Pulse Formation and Dynamics in Self-Pulsating Semiconductor Laser Diodes

by

Stephen A. Lynch

A thesis submitted for the degree of
Doctor of Philosophy
in the University of Dublin

Department of Pure and Applied Physics
Trinity College Dublin
University of Dublin

October 1999

Declaration

This thesis has not been submitted as an exercise for a degree in this or any other university. The work described in this thesis is entirely my own, with exception of assistance recognised in the acknowledgements and the collaborative work noted in the publications. I agree that Trinity College may lend or copy this thesis on request.

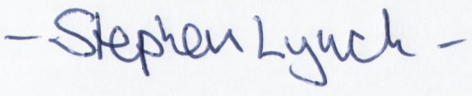

Stephen Anthony Lynch

Pulse Formation and Dynamics in Self-Pulsating Semiconductor Laser Diodes

by Stephen A. Lynch October 1999.

Abstract

Self-pulsating lasers emitting at 800 nm are used in compact disc (CD) players because their low coherence makes them relatively insensitive to optical feedback. The ever increasing demand for higher capacity storage on optical discs necessitates the move to shorter wavelengths. However, attempts at achieving self-pulsation at shorter wavelengths have met with limited success. This suggests that the physical understanding of self-pulsation in semiconductor lasers is incomplete.

The effect of temperature on the processes which control self-pulsation in infrared CD lasers is explored. The variation of self-pulsation frequency with bias current was found to be highly independent of temperature, which means that charge carrier diffusion does not play a first order role. A rate equation model incorporating temperature related effects was developed to explain these results.

Polarisation resolved near field measurements were performed, and high speed streak camera images were recorded. Substantial evidence is presented which proves that there is a considerable modification of the lateral carrier density distribution during the formation and evolution of a pulse. These lateral modifications are explained using a 2D rate equation model. Based on these results, a new hypothesis based on self-focusing is forwarded to explain self-pulsation in these type of lasers.

Similar measurements were performed on commercial red digital video disk (DVD) lasers. The problem of carrier leakage at high temperatures was highlighted. Polarisation resolved near field measurements revealed that these lasers do not make use of the same self-focusing effect identified in CD lasers.

Applications for self-pulsating CD lasers other than data storage were explored. Phenomena such as the electro-optic and all-optical synchronisation of self-pulsating CD lasers were investigated. The fundamental limitations of using a synchronised self-pulsating CD laser as a component of an optically transparent telecommunications system were considered, and constraints on the type of encoding used were inferred.

Acknowledgements

Through the course of my four year sojourn in TCD, I have received the help and friendship of many people. I would like to take this opportunity to express my gratitude.

To Prof. John Hegarty, I would like to say thanks for allowing me the opportunity to join his research group, and for providing the equipment and resources for my work and travel. Thanks also to Dr. John Donegan for looking after my academic well being.

I have been fortunate enough to work alongside six people during my time here. Michael Harley-Stead is responsible for apprenticing me in the art of experimental physics, while Paul Rees and Aidan Egan provided the early modelling backup. The majority of my work was carried out under the watchful eye of my good buddy Pascal Landais and was complemented by modeler supreme Paul McEvoy. I am also grateful for the assistance of new boy Daire Byrne, over the final few months. Nobody could ask for a better mentor than James O'Gorman. The generosity with which he gave of his time went far beyond the call of duty, and without his insight and guidance, none of this work would have been possible.

It is said that no man is an island, and without the friendship of numerous people, the journey towards Ph.D. would have been considerably harder. I was warmly welcomed into the group by Louise, Fred, BR, Tom, and Simon, while Jon Heffernan and John Doran provided often heated entertainment. Too often I was led astray by the terrible three, DTF, 'Speederman' (a.k.a. Christophe) and 'Faagal'. Over time they were joined by Declan, Alan, Cian, John, Gary, Adrian, Paddy, Eamonn, Karl, and Canice, who added to the spice! On the 'other side', the two Daves, Tara, Jennifer, Adrian and Shane were always there to provide a helping hand. Somebody once described Vincent Weldon as the patron saint of graduate students, and I don't believe I can improve on this. Thanks to Elaine for sorting out all of the chaos which

I sent her direction over the years. Thanks also to the technical staff of the Physics Department, Tom Burke, John Kelly, Chris Smith, and in particular Dave Grouse, whose marvellous laser mounts will probably still be in service for many years to come. A special thanks to Mick, Choppy, and Tina for being there when I needed you, and to Joanna for putting up with me. If I've missed out on anyone, you know who you are and thanks.

Thanks to Prof. Wolfgang Elsäßer, Dr. Jens Buus, Dr. Paul Phelan, Prof. Daan Lenstra, Prof. Claudio Mirasso, and Prof. Peter Blood for useful discussions, and to Dr. Didier Erasme and Dr. Guang-Hua Duan for supervising my stay at the ENST in Paris.

Finally I would like to thank my parents Ann and Pádraig, for their love and support, and Máiréad, my sister and closest friend.

Contents

Publications

C. R. Mirasso, G. H. M. van Tartwijk, E. Hernandez-Garcia, D. Lenstra, S. Lynch, P. Phelan, J. O'Gorman, M. San Miguel, and W. Elsaber. Self-Pulsating Semiconductor Lasers: Theory and Experiment. *IEEE J. Quantum Electronics.* 35(5):764-770, May 1999.

P. Rees, P. McEvoy, A. Valle, J. O'Gorman, S. Lynch, P. Landais, L. Pesquera, and J. Hegarty. A Theoretical Analysis of Optical Clock Extraction Using a Self-Pulsating Laser Diode *IEEE J. Quantum Electronics*, 35(2):221-227, February 1999.

A. Egan, M. Harley-Stead, P. Rees, S. Lynch, P. McEvoy, J. O'Gorman and J. Hegarty. All-Optical Synchronisation Of Self-Pulsating Laser Diodes with Frequency Multiplication and Division. *Journal of Modern Optics*, 1998, 45(6):1239-1248

S. A. Lynch, P. McEvoy, P. Landais, J. O'Gorman, J. Hegarty and W. Elsäßer. Temperature Dependence of Self-Pulsation in Narrow Stripe, Gain Guided Compact Disc Laser Diodes. *SPIE Proceedings*, QU04, Quebec 1998

A. Egan, M. Harley-Stead, P. Rees, S. Lynch, P. McEvoy, J. O'Gorman and J. Hegarty. All-Optical Synchronisation of Self-Pulsating Laser Diodes. *Appl. Phys. Lett.* 68(25):3534-3536, 17 June 1996

A. Egan, M. Harley-Stead, P. Rees, S. Lynch, J O'Gorman and J. Hegarty. An Experimental and Theoretical Analysis of Jitter in Self-Pulsating Lasers Synchronised to Periodic Electrical Signals. *IEEE Photonics Technology Letters*, 8(6)758-760, June 1996

S. A. Lynch, P. McEvoy, P. Landais, J. O'Gorman, D. McDonald, J. Donegan, J. Hegarty and W. Elsäßer. Temperature Dependence of the Self-Pulsating Characteristics of Compact Disk Laser Diodes. *CLEO Europe'98*, Glasgow, Sept 1998

S. Lynch, P. McEvoy, P. Landais, J. O'Gorman, D. McDonald, J. Hegarty and W. Elsäßer. Temperature Dependence of Self-Pulsation in Narrow Stripe, Gain Guided, Compact Disk Laser Diodes. *Invited Talk, SPIE QU04*, Quebec 1998.

S. Lynch, P. McEvoy, P. Landais, J. O'Gorman, D. McDonald and J. Hegarty. Effect of Temperature on Self-Pulsation in Narrow Stripe, Gain Guided, Compact Disk Laser Diodes. *CLEO'98*, San Francisco 1998.

S. A. Lynch, P. McEvoy, P. Landais, J. O'Gorman, D. McDonald, J. Donegan, J. Hegarty, W. Elsäßer, and P. Rees. Low Temperature Self-Pulsation in CD Laser Diodes. *SIOE'98*, Cardiff 1998.

P. McEvoy, S. Lynch, P. Landais, J. O'Gorman, D. McDonald, J. Donegan, J. Hegarty, W. Elsäßer, and P. Rees. Oscillation Phenomena in Compact Disc Laser Diodes. *SIOE'98*, Cardiff 1998.

I. Pierse, P. Rees, S. Lynch and P. Landais. Time-Frequency Analysis of Self-Pulsation in Laser Diodes. *SIOE'98*, Cardiff 1998.

P. McEvoy, S. Lynch, J O'Gorman, P. Landais, D. McDonald, P. Phelan, J. Hegarty and P. Rees. Parameter Extraction of Self-Pulsating CD Laser Diodes. *SIOE'97*, Cardiff 1997.

C. R. Mirasso, E. Hernandez-Garcia, M. San Miguel, D. Lenstra, G. van Tartwijk, S. Lynch, P. Landais, P. Phelan and J O'Gorman. Self-Pulsating Frequency Dependence of CD Lasers: A Comparison Between Experiment and Theory. *SIOE'97*, Cardiff 1997.

S. Lynch, P. McEvoy, A. Egan, P. Rees, M. Harley-Stead, J O'Gorman, and J. Hegarty. Dynamics of the Synchronisation of Self-Pulsating Laser Diodes to Periodic Optical Signals. *SIOE'96*, Cardiff 1996.

S. Lynch, P. McEvoy, A. Egan, P. Rees, M. Harley-Stead, J O'Gorman, and J. Hegarty. Timing Issues Relating to All-Optical Synchronisation of Self-Pulsating Laser Diodes. *SIOE'96*, Cardiff 1996.

Chapter 1

Introduction

1.1 General Introduction and Background

The semiconductor laser has in no small way contributed to the explosive growth in optical communications. This has only been made possible by the tremendous advances in semiconductor laser science. Whether one uses threshold current density, spectral characteristics, or brightness as a figure of merit, improvement in semiconductor lasers has followed a curve even more impressive than the oft quoted Moore's Law which describes integration density of silicon chips. Technology which has made this possible has included epitaxial growth techniques such as MOVPE and MBE which allow control down to the level of single atomic layers. Nevertheless, even with the enormous advances which have been made, much remains to be done before it can be said that we have truly mastered the science of semiconductor lasers. New material systems will have to be mastered as the available wavelength range of semiconductor lasers is extended into the yellow, green, blue and ultraviolet. The direct integration of electrical and optical components, which the ever increasing demand for bandwidth will eventually necessitate, will raise a whole new set of problems. In short, the future of semiconductor laser research is still extremely bright!

The ultimate origin of the laser stems back to Einstein's 1917 paper, where the concepts of spontaneous and stimulated emission are introduced for the first time, [1]. The development of the first operational laser followed very quickly after the publication of Schawlow and Townes' celebrated 1958 paper [2]. By 1960 Maiman had demonstrated an operational Ruby laser [3] and by 1962 several groups had reported lasing action in semiconductors. The first semiconductor laser consisted of a forward biased GaAs p-n junction, which provided the optical gain, and a cavity defined by two polished facets perpendicular to the junction plane providing the optical feedback. However, a combination of bad transverse confinement and absorption in the GaAs semiconductor material surrounding the gain region led to very large threshold current densities ($> 50,000$ A/cm^2), making room temperature operation impossible. Towards the end of the 1960s, the problems faced by homostructure lasers were countered by the introduction of the double heterostructure. In this type of laser a narrow bandgap semiconductor is sandwiched between to two layers of wider bandgap material. This has the dual effect of improving the transverse confinement, and considerably reducing the absorption in the material around the gain region. The net result was much lower threshold current densities ($< 1,500$ A/cm^2), making room temperature operation possible. By the early 1970s the technology improved considerably. New ridge waveguide, and buried heterostructures improved lateral confinement (both current and optical), driving threshold current densities even lower. During this decade distributed feedback (DFB), distributed Bragg reflectors (DBR), cleaved coupled cavity (C^3), and external cavity lasers which were investigated with the aim of producing lasers with narrow spectral linewidths for long haul high speed optical communications. From the 1970s onwards many new material systems were investigated, extending the available wavelength range from the near-infrared to the visible. Quantum well active regions were introduced in order to enhance the optical gain and improve temperature characteristics. The early 1990s saw the introduction of a completely new

type of structure, the vertical cavity surface emitting laser (VCSEL) which opened up a whole new area of semiconductor laser applications. Other recent developments have included the quantum cascade laser, which opens up the mid to far infrared region of the electromagnetic spectrum.

Self-pulsation was known from the days of the very first semiconductor lasers. It was initially associated with degraded devices and was considered an undesirable phenomenon. Much of the early research on this topic was undertaken with the aim of engineering devices which did not self-pulsate. With the eventual progress in growth epitaxy, the quality of semiconductor material improved to the extent that spurious self-pulsation was almost never observed in newly manufactured devices. During the early 1980s a few applications emerged which could exploit the phenomenon and it became necessary to engineer laser diodes to exhibit self-pulsation. In particular, the low coherence properties of self-pulsating lasers made them an ideal candidate for the reading head of the newly developed compact disc player. In the late 1980s and early 1990s it was realised that self-pulsating lasers could also be used to extract and redistribute the clock from an optical stream of data. Considerable research was undertaken in order to develop high speed self-pulsating lasers for this purpose. Currently, the major thrust of the research into self-pulsating lasers revolves around the development of short wavelength devices for next generation optical storage applications.

This thesis is predominantly concerned with the underlying physics behind the latter two of these fields, that is, short wavelength self-pulsating lasers for data storage, and the application of self-pulsating lasers as a component in transparent optical networks.

1.2 Thesis Overview

Chapter 2, contains all of the background physics pertinent to this thesis. Some of the topics covered include the propagation of light in semiconduc-

tor materials, electrical pumping, and optical gain. The rest of the chapter includes an introduction to self-pulsation and a more in-depth look at self-pulsation in CD type structures. As far as possible these subjects are presented in modules, so that the well informed reader can skip over familiar material.

In chapter 3, the effect of temperature on the processes which influence self-pulsation in infrared CD lasers are explored. Data is presented on the effect of temperature on the self-pulsation frequency, over a wide temperature range. The remainder of the chapter is devoted to the development of a rate equation model which incorporates these temperature related effects.

Chapter 4 deals with the physics of pulse formation in CD type laser structures. Substantial experimental evidence is presented which proves that there is a considerable modification of the lateral carrier density distribution during the formation and evolution of a pulse. These lateral modifications are investigated and explained using a 2D rate equation model. The chapter concludes with a new hypothesis on the origins of self-pulsation in CD lasers.

In chapter 5, experimental data pertinent to self-pulsation in short wavelength lasers is presented. Similar investigations to those in Chapters 3 and 4, but relevant to visible self-pulsating lasers are detailed. Based on the experimental data, some conclusions are drawn on the problems of achieving self-pulsation in wider bandgap semiconductor materials.

Chapter 6 reports on some of the applications of self-pulsating lasers. It concentrates on the potential use of the self-pulsating laser as a component of an all-optical clock extraction and re-distribution subsystem. This type of subsystem might be used in future optically transparent networks.

In chapter 7 the key results from the preceding chapters are gathered together in one coherent block. Some final thoughts on the future of this research are also presented here.

1.3 A Word On Notation

As far as possible, I have tried to keep to the conventional notation for most of the symbols throughout this thesis. Unfortunately, due to the diverse areas of physics drawn upon, a strict adherence to conventional notation does leave room for some ambiguity. For example, letter E is used for energy and for electric field. In most cases the meaning of these conventionally overused symbols should be entirely obvious.

Chapter 2

Semiconductor Lasers and Self-Pulsation: Basic Concepts

2.1 Overview

The aim of this chapter is to set down the background physics and some of the experimental techniques which are used in the subsequent chapters. Section 2.2 deals with physics of waveguiding in semiconductor material and is relevant for Chapters 4 and 5. Section 2.3 describes the physics of light amplification and gain in semiconductor laser diodes and is used mainly in the discussion of the temperature dependent rate equation model in section 3.4 of chapter 3. The history and development of the semiconductor laser diode is described briefly in section 2.4, and section 2.5 chronicles the history of self-pulsation in laser diodes. Finally, in sections 2.6 and 2.7, the principal characteristics of self-pulsating CD lasers are introduced, along with some of the conventional wisdom regarding the physics of self-pulsation in this type of laser.

2.2 Propagation of Light in Semiconductor Waveguides

In general, two ingredients are required for lasing, optical gain and feedback. In a semiconductor laser, feedback is usually achieved through reflection at the semiconductor/air interfaces of the Fabry-Perot cavity defined by the two cleaved facets of the laser chip. By the same token, the optical mode propagating along this resonant cavity must be adequately guided in the transverse direction so that the energy does not leak away into the surrounding regions. The longitudinal and transverse characteristics of a semiconductor resonant cavity are now discussed in the following two subsections.

2.2.1 Resonant Cavities and Axial Modes

The high gain associated with inverted semiconductor material is sufficient that only moderate reflection is required to achieve the feedback necessary for lasing. This fact is illustrated by the following simple calculation (in this case taking the refractive index of GaAs to be $\simeq 3.6$). Here the relevant Fresnel equation gives the reflection coefficient of the semiconductor/air interface in terms of the refractive indices,

$$R_{facet} = \left(\frac{n_2 - n_1}{n_2 + n_1}\right)^2 = \left(\frac{3.6 - 1}{3.6 + 1}\right)^2 \simeq 0.32. \tag{2.1}$$

Within the resonant cavity formed by the two facets, standing wave patterns are set up. These must satisfy the condition:

$$m\frac{\lambda}{2} = L_{opt}, \tag{2.2}$$

where λ is the wavelength, L_{opt} is the *optical* pathlength between the two facets, and m is an integer. Each value of m satisfying Eq. 2.2 defines what is known as an *axial* or *longitudinal* mode of the resonant cavity. Equation 2.2 can also be written in terms of frequency.

$$\nu = \frac{mc}{2L_{opt}} \tag{2.3}$$

where ν is the frequency. Using a typical values for the length and refractive index of a semiconductor laser chip ($L = 250$ μm, $n_g = 3.6$), emitting at $\lambda = 800$ nm, it is possible to calculate the frequency separation $\Delta\nu$, and the wavelength separation $\Delta\lambda$, between adjacent axial modes.

$$\Delta\nu = \frac{c}{2n_gL} = \frac{3 \times 10^8 \ ms^{-1}}{2(3.6)(250 \times 10^{-6} \ m)} \simeq 167 \text{ GHz}$$
$$\Delta\lambda = \frac{\lambda^2}{2n_gL} = \frac{(800 \times 10^{-9} \ m)^2}{2(3.6)(250 \times 10^{-6} \ m)} \simeq 0.36 \text{ nm} \tag{2.4}$$

The number of axial modes in the optical spectrum depends on the width of the gain spectrum. Typically, for a simple Fabry-Perot laser diode this is large. Fig. 2.1 shows a typical above threshold optical spectrum of a simple CW Fabry-Perot AlGaAs laser diode emitting at around $\lambda = 780$ nm. For this laser diode $\Delta\lambda = 0.31$ nm.

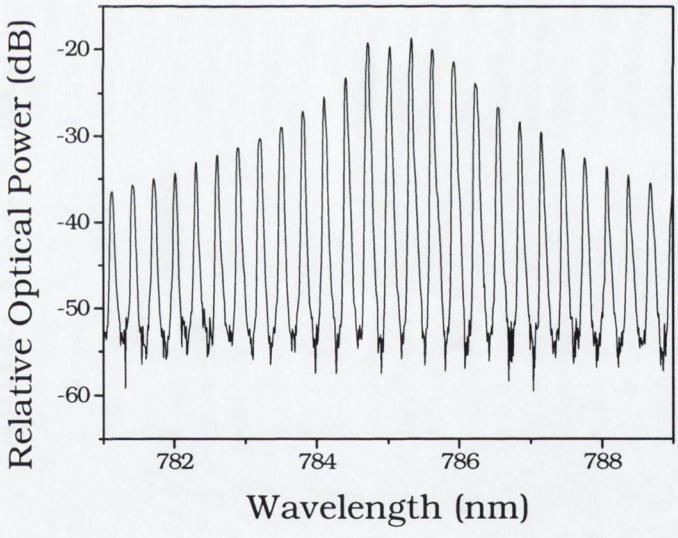

Figure 2.1: Typical above threshold optical spectrum of a simple CW Fabry-Perot AlGaAs laser diode emitting at around $\lambda = 780$ nm.

For many applications, particularly telecommunications, a multi-mode spectrum is very undesirable. For example, single mode lasing emission dra-

matically increases the upper bandwidth at which information can be transferred down an optical fibre. Many novel ways of achieving single mode emission have been demonstrated. The most common is undoubtedly the distributed feedback (DFB) laser. Here feedback is achieved, not through reflection at the facets, but through the multiple reflections from a grating which has been fabricated along the length of the laser chip above the active region [4]. Other methods of achieving single frequency operation have included using distributed Bragg reflecting (DBR) structures [4], cleaved coupled cavity (C^3) structures [5], and stabilised Fabry-Perot (SFP) structures [6].

2.2.2 Transverse Modes and the slab waveguide

The following subsection deals with the basic description of TE and TM mode propagation in slab dielectric waveguides. A mode of a dielectric waveguide at an angular frequency ω is a solution of the wave equation (2.5).

$$\vec{\nabla}^2\vec{E}(\vec{r},t) + k^2n^2(\vec{r})\vec{E}(\vec{r},t) = 0 \tag{2.5}$$

The solutions of this equation are subject to the continuity of the tangential components of $\vec{E}$ and $\vec{H}$ at the dielectric interfaces, and the field generally takes the form:

$$\vec{E}(\vec{r},t) = \vec{\mathcal{E}}(\vec{r})e^{i[\omega t - \phi(\vec{r})]} \tag{2.6}$$

where $k = \omega/c$ and $n(\vec{r})$ is the index of refraction. The basic guiding features of a dielectric waveguide can be extracted from a simple planar model in which no variation exists in the y-direction. Fig. 2.2 shows a simple slab waveguide. The z-axis has been chosen as the direction of propagation and $\partial/\partial y = 0$. Limiting the analysis to waves with phase fronts normal to the waveguide axis, z, and setting $\phi(\vec{r}) = \beta z$, equation (2.5) becomes:

$$\left(\frac{\partial^2}{\partial x^2} + \frac{\partial^2}{\partial y^2}\right)\vec{E}(x,y) + [k^2n^2(\vec{r}) - \beta^2]\vec{E}(x,y) = 0 \tag{2.7}$$

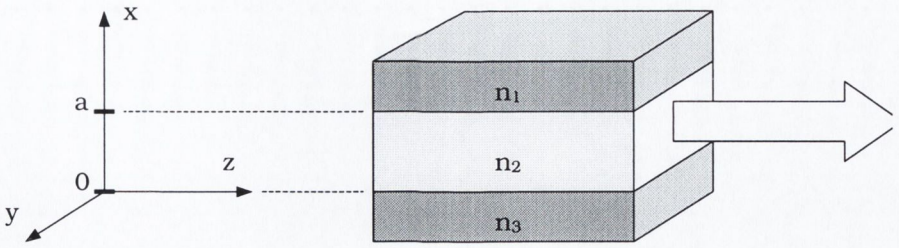

Figure 2.2: Schematic of a three-layer slab waveguide. The large arrow indicates the direction of propagation. Indices are assumed to be in the x-direction.

Putting $\partial/\partial y = 0$ in Eq. (2.7) and writing it separately for regions 1,2 and 3, yields a set of three equations (2.8) where $E(x,y)$ is a cartesian component of $\vec{E}(x,y)$.

$$\begin{aligned}
&\frac{\partial^2}{\partial x^2}E(x,y) + (k^2 n_1^2 - \beta^2)E(x,y) = 0, \qquad x > a \\
&\frac{\partial^2}{\partial x^2}E(x,y) + (k^2 n_2^2 - \beta^2)E(x,y) = 0, \qquad 0 < x < a \\
&\frac{\partial^2}{\partial x^2}E(x,y) + (k^2 n_3^2 - \beta^2)E(x,y) = 0, \qquad x < a
\end{aligned} \tag{2.8}$$

Two types of solution sets are possible. The solution set,

$$\begin{aligned}
E_y &= \mathcal{E}_y(x)e^{i(\omega t - \beta z)}, \\
H_x &= -\frac{i}{\omega\mu}\frac{\partial E_y}{\partial z}, \\
H_z &= \frac{i}{\omega\mu}\frac{\partial E_y}{\partial x},
\end{aligned} \tag{2.9}$$

are known as transverse electric (TE), with polarisation aligned in the plane of the waveguide (in the case of a real laser diode this would be in the plane of the active region). On the other hand, the solution set,

$$\begin{aligned}
H_y &= \mathcal{H}_y(x)e^{i(\omega t - \beta z)}, \\
E_x &= \frac{i}{\omega\varepsilon}\frac{\partial H_y}{\partial z}, \\
E_z &= -\frac{i}{\omega\varepsilon}\frac{\partial H_y}{\partial x},
\end{aligned} \tag{2.10}$$

are known as transverse magnetic (TM), with polarisation aligned perpendicular to the waveguide (in the growth direction for a real laser diode). Here μ and ε have their usual meanings.

Inspection of the general solution of the equation set (2.8) reveals that some constraints must be put on the values of n_1, n_2 and n_3 if the waveguide is to support guided modes. It is assumed first that $n_2 > n_3, n_1$ so that the sandwiched layer, 2, always has the highest refractive index. Fig. 2.3 illustrates some of the possible solutions of equation set (2.8). For $\beta > kn_2$,

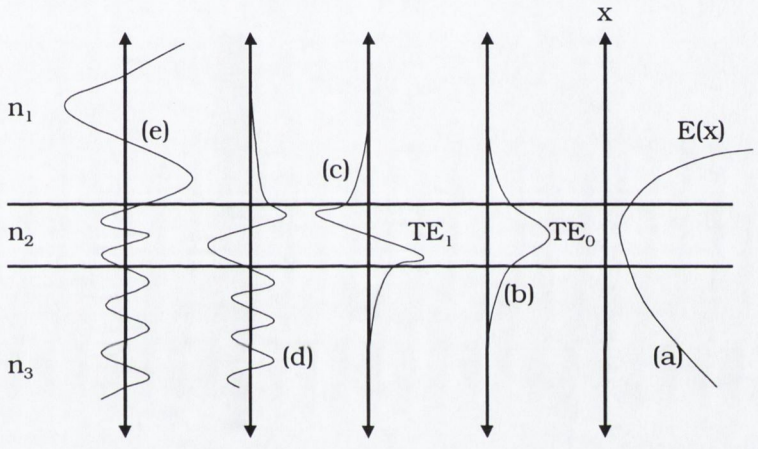

Figure 2.3: Illustration showing the electric field distributions corresponding to different values of the propagation constant β of the waveguide.

solution (a), $E(x)$ is exponential everywhere. This solution is not physically realisable and thus does not correspond to a real wave. For $kn_3 < \beta < kn_2$, solutions such as (b) and (c) are obtained. While the electric field is sinusoidal in layer 2, it decays exponentially in layers 1 and 3. The majority of the energy is confined in layer 2, and thus these are referred to as *confined* or *guided* modes. At a given wavelength the number of guided modes will depend on the thickness of layer 2, and on the indices of refraction, n_1, n_2 and n_3. At some minimum thickness of layer 2, the TE_0 mode becomes confined. Further increases in the thickness of this layer will allow the TE_1 mode to be confined, and so on. Solutions for $kn_1 < \beta < kn_3$, correspond to

exponential behaviour in layer 1, and to sinusoidal behaviour in layers 2 and 3 as illustrated by (d). These type of modes are called substrate radiation modes. For $0 < \beta < kn_1$, as in (e) the solution becomes sinusoidal in all three layers. These are the so-called radiation modes of the waveguide.

While the three slab waveguide is quite a simplification from reality, most of the results hold true for real semiconductor waveguides. In the case where the exact solutions are required, these can be calculated numerically using similar arguments [4, 7]. It is also possible to show that there is a difference in the facet reflectivity (pg. of 304 of [4]) and the optical confinement for TE and TM modes (pg. 46 of [8]). These quantities play an important role in deciding the dominant polarisation of the lasing emission.

2.3 Light Amplification in Inverted Media

When an electron, which is in an excited state, returns to its ground state, it must release the energy of this transition. If the energy separation of the initial and final states is sufficient, then the net energy from the transition may be released in the form of a photon of light. It is the possibility of a radiative transition such as this which forms the basis of light generation in semiconductor material.

The following two subsections deal with the underlying physics within semiconductors which lead to radiative recombination, and ultimately lasing under the right conditions. The first subsection deals with the general aspects of carrier recombination. The second subsection brings these ideas further and illustrates how these physical processes may be exploited to achieve light amplification and ultimately lasing.

2.3.1 Recombination of Carriers and the Generation of Light

The net rate of change of carriers in an electrically pumped semiconductor will depend on the rate at which carriers are created through electrical pumping, and the rate at which these carriers are lost through recombination. This sentence can be simply expressed by Eq. (2.11), where R_{gen} denotes the generation rate and R_{rec} denotes the overall recombination rate.

$$\frac{dN}{dt} = R_{gen} - R_{rec} = \frac{I}{eV} - R_{rec} \tag{2.11}$$

R_{gen} may be simply expressed in terms of the magnitude of pumping current, I. Here e is the electronic charge, and V is the volume of the *active* region. The recombination rate may consist of four components.

$$R_{rec} = R_{sp} + R_{nr} + R_l + R_{st} = \frac{N}{\tau(N)} + R_{st} \tag{2.12}$$

R_{sp} is the rate at which carriers recombine to give spontaneous emission, R_{nr} is the rate at which carriers recombine nonradiatively, R_l is the carrier leakage rate, and finally R_{st} is the rate at which carriers recombine to give stimulated emission. The carrier recombination rate can be re-written in terms of the carrier density, N, and a time constant or *lifetime*, $\tau(N)$, in which the first three processes are lumped together as one. This is conventionally described by a power series in N, where the individual terms have meaning.

$$\frac{N}{\tau(N)} = AN + BN^2 + CN^3 \tag{2.13}$$

Fig. 2.4 illustrates some of the recombination processes described by this power series. The first and third terms in the series, $(AN + CN^3)$, deal with nonradiative recombination. AN parameterises two processes, defect recombination and surface recombination. These are illustrated by Fig. 2.4(b). In this case an electron falls into a defect or surface level in the band gap. It then recombines nonradiatively from this level. The third term, CN^3 parameterises a two body process, known as Auger recombination. There are many

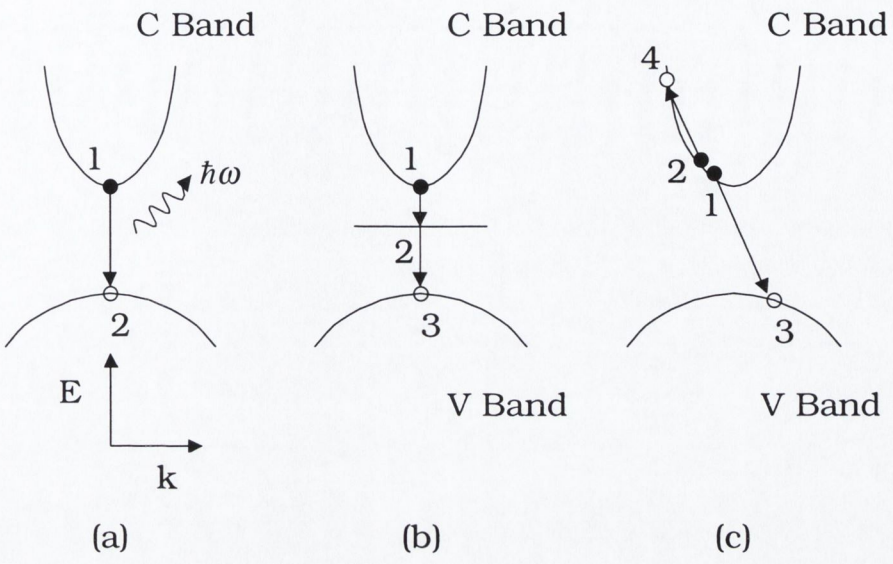

Figure 2.4: Illustration showing possible recombination processes in a semiconductor on a simple band diagram. (a) Radiative, (b) Non-radiative, and (c) Auger.

permutations of this process which are denoted by the initial and final energy states. Fig. 2.4(c) depicts the CCCH process, which involves three electron states and one heavy hole state. In this particular example, two electrons collide in the conduction band. One of the electrons is excited into the valence band while the other is excited higher into the conduction band, where it eventually thermalises back down to the bottom of the conduction band, releasing the excess energy as heat. Finally, the second term of the power series, BN^2, parameterises radiative recombination. This process requires vertical transitions in k-space and is depicted in Fig. 2.4(a).

The recombination rates of all these processes can now be gathered in one very simple rate equation, and in an analogous way, a second equation describing the rate at which photons are generated can be written down.

$$\frac{dN}{dt} = \frac{I}{eV} - \frac{N}{\tau(N)} - R_{st} \tag{2.14}$$

$$\frac{dP}{dt} = \Gamma R_{st} + \Gamma \beta_{sp} R_{sp} - \frac{P}{\tau_P} \tag{2.15}$$

The first term in Eq. (2.15) describes the rate at which photons are generated through stimulated emission. The pre-factor, Γ takes into account that the cavity volume occupied by the photons is larger than the active region volume. The second term deals with the rate at which photons are generated by spontaneous emission. β_{sp} is the reciprocal of the number of optical modes in the bandwidth of the spontaneous emission. The last term describes the rate at which photons are removed from the cavity. For the moment this term is defined in a similar fashion to the carrier recombination rate in Eq. (2.14).

2.3.2 Optical Gain and Stimulated Emission

I now turn to details of calculating the terms R_{st} and R_{sp} in equations (2.14) and (2.15). Fig. 2.5 shows a two level diagram depicting the three processes. The rates at which these three processes occur depends on the density of

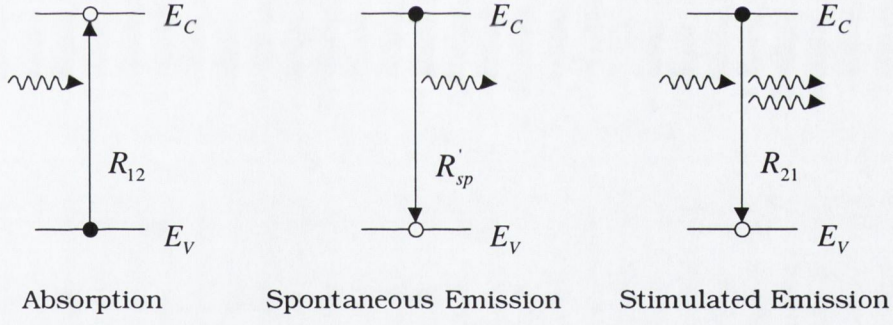

Figure 2.5: Energy level diagram illustrating the single-mode transition rates for absorption, spontaneous emission and stimulated emission.

photons and the density of available state pairs. The dependence on the photon density enters through the local electric field strength, $|\mathcal{E}|^2$. $|\mathcal{E}|^2$ can be described in terms of the number of photons in an optical mode, PV_P (where V_P is the volume of the mode), and the field strength of one photon $|\mathcal{E}_{\hbar\omega}|^2$. Thus $R_{12}, R_{21} \propto |\mathcal{E}|^2$ and $R_{sp}' \propto |\mathcal{E}^{vf}|^2$, where $|\mathcal{E}^{vf}|^2$ is vacuum field strength. The vacuum field strength arises from the fact that the lowest

energy state of a quantised field is not zero. Expressed another way, the vacuum field strength is really the field strength generated by one photon, i.e. $|\mathcal{E}^{vf}|^2 = |\mathcal{E}_{\hbar\omega}|^2$. It should be noted here that R_{12}, R_{21} and R'_{sp} are the single mode transition rates. R_{sp} is obtained by summing over all optical modes. Since transitions can only occur between filled initial states and empty final states the three transition rates become:

$$R_{12} = R_r f_1(1 - f_2), \tag{2.16}$$

$$R_{21} = R_r f_2(1 - f_1), \tag{2.17}$$

$$R'_{sp} = R_r^{vf} f_2(1 - f_1). \tag{2.18}$$

Here f_1 and f_2 are the occupation probabilities which are usually described well by Fermi functions. R_r is the transition rate that would exist if all state pairs were available to participate in the transition. For the spontaneous emission rate, $R_r^{vf} = R_r$, with $|\mathcal{E}|^2 \to |\mathcal{E}^{vf}|^2$. R_{st} is simply the net generation rate of photons in the semiconductor and thus:

$$R_{st} = R_{21} - R_{12} = R_r(f_2 - f_1) \tag{2.19}$$

This allows simple relations between the transition rates to be derived.

$$\frac{R_{21}}{R_{12}} = e^{(\Delta E_F - E_{21})/kT} \tag{2.20}$$

$$\frac{R'_{sp}}{R_{st}} = \left(\frac{1}{PV_P}\right) \frac{1}{1 - e^{(E_{21} - \Delta E_F)/kT}} \tag{2.21}$$

Eq. 2.20 states that the stimulated emission rate will only be larger than the absorption rate when $E_{Fc} - E_{Fv} \equiv \Delta E_F > E_{21}$. This means that the net stimulated rate will only be positive when the quasi-Fermi level separation (discussed in section 2.4.1), $E_{Fc} - E_{Fv}$, is greater than the photon energy of interest. Since the photon energy must at the very least be equal to the bandgap energy, then to achieve gain in a semiconductor, the voltage across a p-n junction must be greater than the bandgap. Eq. 2.21 reveals that there

is a fundamental relationship between the single mode spontaneous emission rate and the net stimulated emission rate.

The rate at which transitions take place in the presence of a time dependent perturbation can be calculated directly from Fermi's Golden Rule,

$$R_r = \frac{2\pi}{\hbar} \left| \langle 1|\mathcal{H}'|2\rangle \right|^2 \rho_f(E_{21}) \Big|_{E_{21}=\hbar\omega}. \tag{2.22}$$

Fermi's Golden rule reveals that the number of transitions per unit volume, occurring per second is dependent on (a) the density of final states, $\rho_f(E_{21})$ available to the electron, and (b) the spatial overlap of the initial and final electron wavefunctions with the harmonic perturbation, described by the Hamiltonian, $\mathcal{H}'$. The details of the calculation of the matric element $\langle 1|\mathcal{H}'|2\rangle$ are beyond the scope of this thesis. However, Coldren [4] provides an excellent treatment. Of more interest is the end result. Material gain is defined as the proportional growth of the photon density as it propagates along some direction, i.e.

$$G = \frac{1}{P}\frac{dP}{dz} = \frac{1}{v_g P}\frac{dP}{dt} = \frac{1}{v_g P}(R_{21} - R_{12}) = \frac{R_{st}}{v_g P} = \frac{R_r}{v_g P}(f_2 - f_1). \tag{2.23}$$

Using Fermi's Golden rule for R_r, the single mode gain, G_{21}, can be calculated.

$$G_{21} = \frac{2\pi}{\hbar}\frac{\left|\langle 1|\mathcal{H}'|2\rangle\right|^2}{v_g P}\rho_{red}(E_{21})(f_2 - f_1) \tag{2.24}$$

$\rho_{red}(E)$, with its associated energy dependence, is the reduced density of states. This is interpreted as the density of electron-hole transition pairs per transition energy, ΔE, and thus will depend on the number of states in the conduction band and the valence band. If k-selection applies, then only states with identical k-vectors can form a transition pair, and only vertical transitions in k-space can occur. Because of this condition, the number transition pairs within Δk must be equal to the number of states in the conduction or valance band, and thus

$$\rho_{red}(E)\Delta E = \rho_c(E)\Delta E_c = \rho_v(E)\Delta E_v. \tag{2.25}$$

Finally by setting $\Delta E = \Delta E_c + \Delta E_v$ the reduced density of states can be simply expressed in terms of the density of states in the conduction and valance bands:

$$\frac{1}{\rho_{red}(E)} = \frac{1}{\rho_c(E)} + \frac{1}{\rho_v(E)}. \tag{2.26}$$

G_{21} is then summed over the number of modes in the bandwidth of the spontaneous emission, to give G. The ultimate form of this expression is quoted later (on pg. 54 of chapter 3) along with some calculations. However it suffices in this section to consider some of the general features of the gain spectrum. The shape of the bounding limits of the gain spectrum is primarily

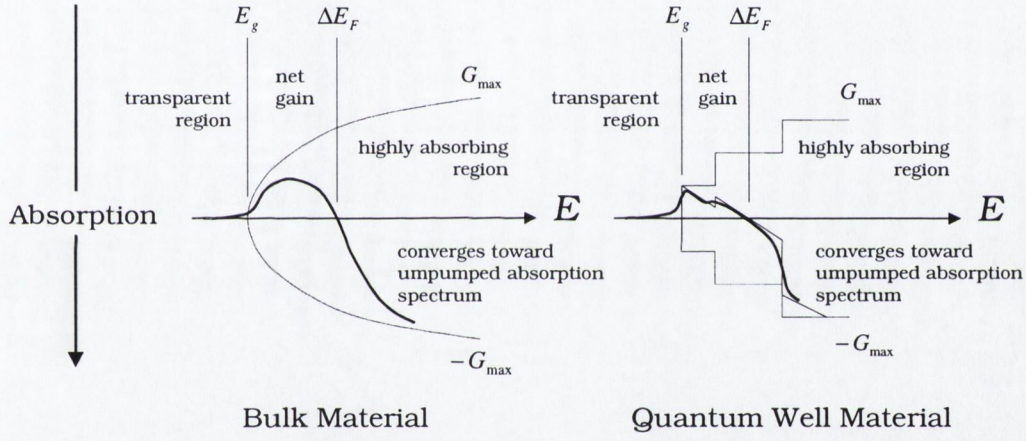

Figure 2.6: Gain spectra in bulk and quantum-well materials (based on illustration from [4]).

governed by the reduced density of states function. In bulk material this function scales as $E^{1/2}$, while in quantum well material it follows a step-like dependence, (see pg. 48 of chapter 3). As a result the bulk gain spectrum is quite smooth, while the quantum well gain spectrum may show some features, depending on the amount of broadening.

For rate equation models, only the variation of peak gain with carrier density is required. The complication of performing the full gain calculation often is circumvented by making simple approximations. For bulk material

the approximation $G = a(N - N_0)$ is used. For quantum well material, the logarithmic form $G = a\ln(N/N_0)$ is a better approximation. Fig. 2.7 shows an illustration of the linear gain approximation. Here the coefficient a is

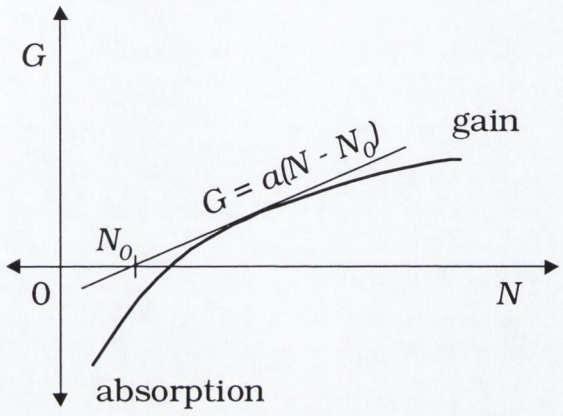

Figure 2.7: Illustration showing the linear gain approximation. Plotted on the graph is the peak gain as a function of carrier density.

the called the differential gain and corresponds to the slope of the line. N_0 is carrier density axis intercept. The physical interpretation of this point is transparency. The rate equations on pg. 14 of section 2.3.1 can now be written in the more familiar form (2.27) and (2.28),

$$\frac{dN}{dt} = \frac{I}{eV} - \frac{N}{\tau(N)} - v_g GP, \tag{2.27}$$

$$\frac{dP}{dt} = \Gamma v_g GP + \Gamma \beta_{sp} BN^2 - \frac{P}{\tau_P}. \tag{2.28}$$

2.4 Background on Laser Diodes

The two conditions necessary for lasing have been discussed at length in the previous sections. The topic of this section is the realisation of these conditions in a practical semiconductor device.

2.4.1 PN junctions and carrier injection

The first of the two lasing conditions was optical feedback. The simplest method of achieving this is to exploit the natural Fabry-Perot resonator defined by the cleaved facets of a laser chip. The second condition was optical gain. In section 2.3.2 it was shown that optical gain is only possible in semiconductor material if the Fermi level separation is larger than the bandgap. A very convenient way to achieve this condition in semiconductor material is to use a forward biased p-n junction.

A p-n junction is formed by bringing a p-type and an n-type semiconductor into contact with each other. Fig. 2.8 shows the energy band diagram before and after contact. Before contact the individual Fermi levels do not match up. Once they are in contact, electrons from the n-side and holes from the p-side diffuse across the junction. The causes an electric field to be set up which opposes the the flow of carriers. Eventually a steady state is reached and the Fermi level is continuous across the p-n junction, as shown in the middle diagram in Fig. 2.8. The p-n junction can be forward biased by applying an external voltage, which reduces the electric field at the junction, and results in further diffusion of electrons and holes across the junction. Since there is no longer an equilibrium situation the Fermi level is no longer continuous across the junction. The electron and hole populations either side of the junction are instead represented by quasi-Fermi levels. There will be a narrow depletion region at the junction interface where both electrons and holes are present simultaneously and can combine radiatively or nonradiatively. When the external voltage exceeds a critical value such that the quasi-Fermi level separation exceeds the bandgap of the material, population inversion is achieved. When this point is reached the junction is then able to amplify electromagnetic radiation and exhibits optical gain.

The very first semiconductor lasers were fabricated using the simple p-n junction just described. However, they suffered from two main disadvan-

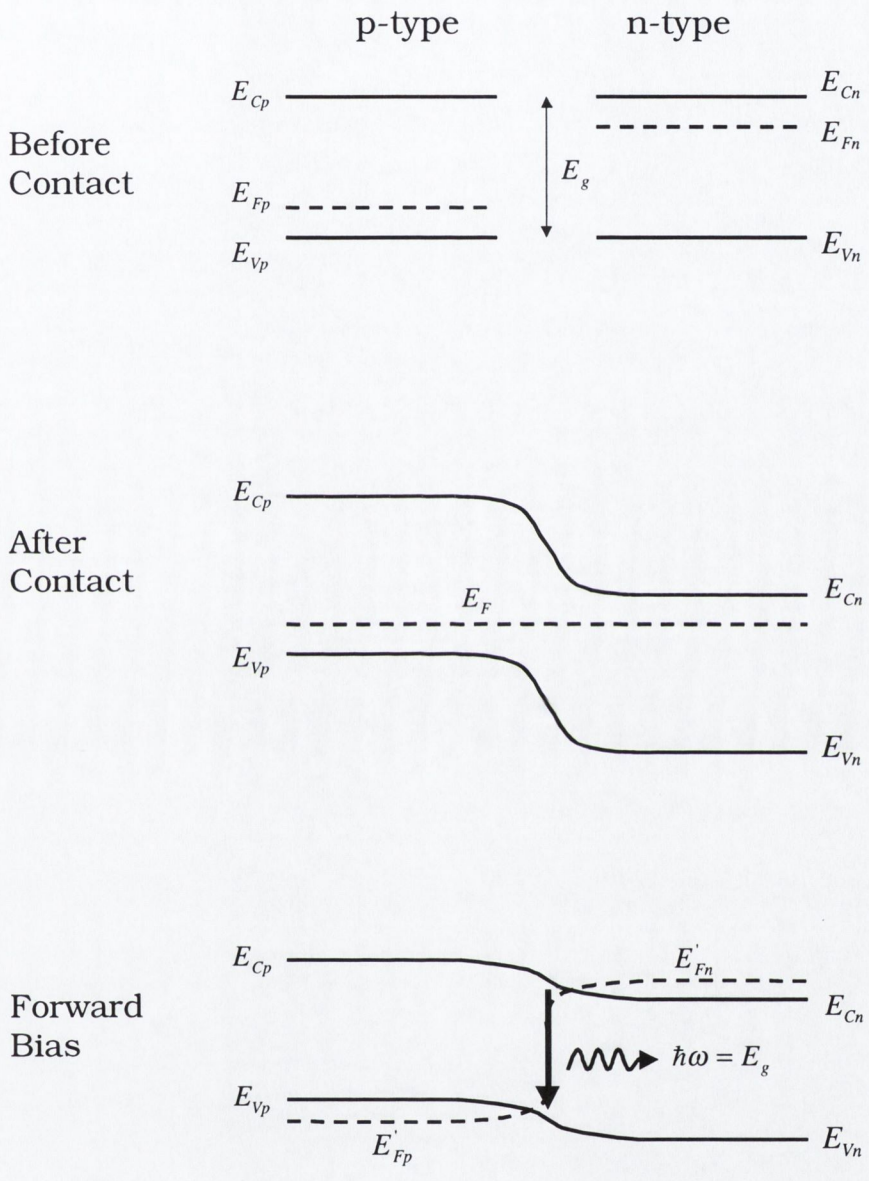

Figure 2.8: Energy band diagram of a p-n junction. Top: before contact, middle: after contact with zero bias, and bottom: forward bias.

tages. Both the carrier confinement and optical confinement were very poor which resulted in very large threshold currents. Consequently these so-called *homostructure* lasers could only be operated under cryogenic conditions.

2.4.2 Heterostructure Lasers

The shortcomings of homostructure lasers were quickly overcome by replacing the homostructure with a heterostructure. In a heterostructure, material of different bandgap is incorporated into the junction. The most well known example is probably the GaAs/AlGaAs system. Fig. 2.9 shows an energy band diagram of a p-i-n single heterostructure laser. The thin intrinsic active region has a lower bandgap than the two p-type and n-type cladding layers. The bandgap difference causes potential barriers to form in both the conduction and valence bands. These potential barriers confine carriers to a narrow active region and allow a substantial population inversion to be built up. The smaller refractive index associated with the larger bandgap of the cladding layers also causes the optical mode to be guided in the active region. Furthermore, since the tails of this optical mode are propagating through wider bandgap material it is not absorbed in these regions. Further improvements can be achieved using double heterostructures, where an additional large bandgap layer is included to optimise the guiding in either growth directions. Additional refinements have included stripe geometries, buried heterostructures, and graded index separate confinement heterostructures, (GRINSCH). These have led to the eventual room temperature operation of semiconductor laser diodes.

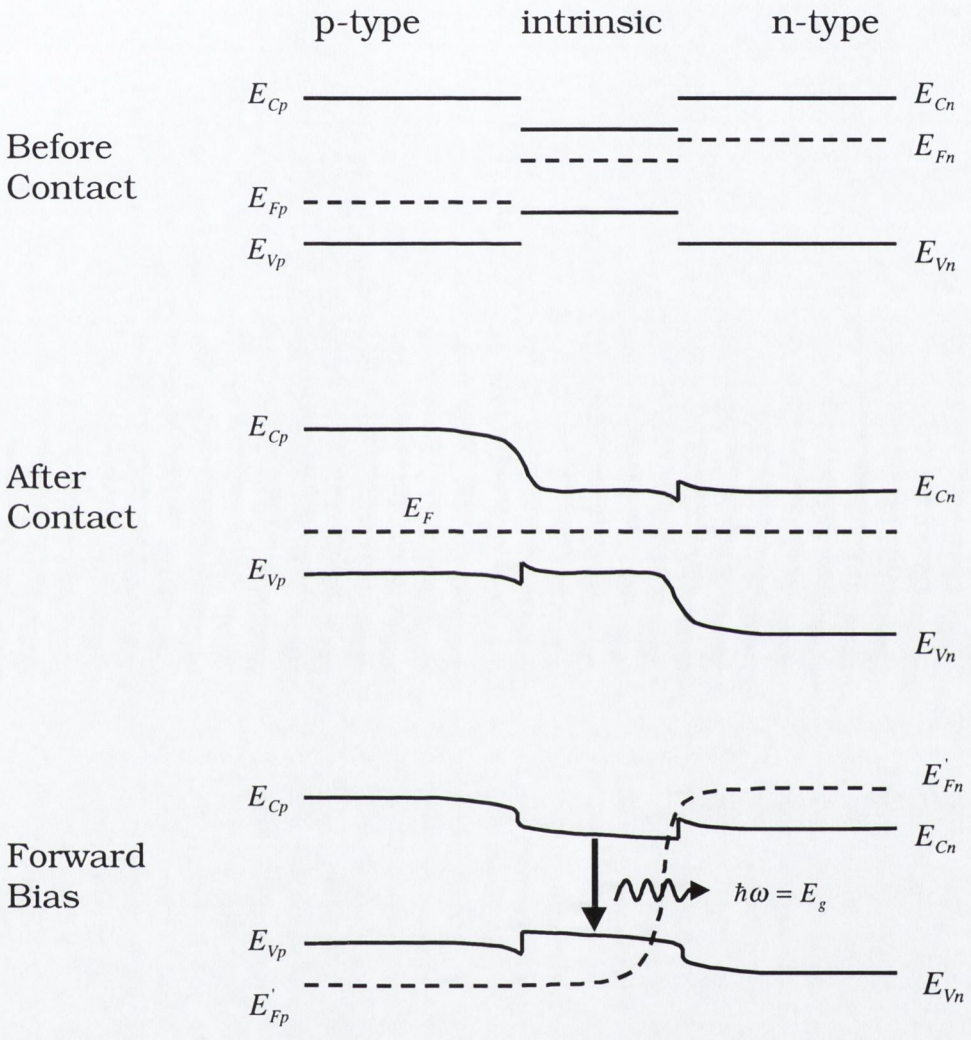

Figure 2.9: Energy band diagram of a p-i-n single heterojunction. Top: before contact, middle: after contact with zero bias, and bottom: forward bias.

2.5 Background on Self-Pulsating Laser Diodes

2.5.1 Self-Pulsation in degraded materials

Since the advent of the very first semiconductor lasers self-pulsation was well known, and has been a topic of great interest. It was originally considered to be an undesirable phenomenon and was associated with elevated defect densities in poor quality materials or degraded devices, [9]. The defect centres were believed to act as saturable absorbers, leading to self-pulsation or bistability in the device dynamics. With the continual progress in epitaxial growth technologies, conventional mono-section lasers no longer exhibited these phenomena. It was later realised that self-pulsation is attractive for many applications, and it became necessary to engineer reliable high quality laser diodes which exhibited self-pulsation. The following subsections contain a brief synopsis of some of the key milestones in this development.

2.5.2 Self-Pulsation by design

One of the earliest studies of self-pulsation in the literature was by Basov [10] in 1968. Basov investigated the behaviour of two-section lasers, that is, a single laser diode chip with two independently biased sections. Self-pulsation was observed when one of the sections was biased near transparency while the other section was biased in gain. Basov explained this behaviour using a simple rate equation model and confirmed using a linear stability analysis that self-pulsation can only arise in this type of structure when one section is biased well below transparency and the other section is biased in gain.

Self-pulsation was also studied in proton-bombarded stripe geometry double heterostructures, which were not aged and exhibited well defined self-pulsation from the initial moment of operation, [11]. The origin of the self-pulsation in these devices was accounted for by nonlinear gain.

Although work on self-pulsation continued during the 1970s, especially in the context of degradation and defects in lasers, it was not until the late seventies and early eighties that significant advances were made in its understanding. In 1979 Dixon and Joyce proposed a model for self-pulsation in AlGaAs double heterostructure lasers, [12]. It had previously been proposed that self-pulsation could arise in such devices due to dark-line defects. However, they were forced to seek another explanation for self-pulsation in laser diodes which they had fabricated and which did not contain dark-line defects. They proposed that non-radiative recombination near the cleaved facets of the laser can depress the carrier density and lead to regions of saturable absorption. Since these saturable absorption regions were confined to the ends of the laser, these regions can be lumped together as one. The device is then assumed to be made up of two sections, the main gain region, and a saturable absorber region located at one end. The authors constructed a coupled three rate equation model which described the evolution of the carrier density in each of the two sections as well as the average photon density. It is this model which forms the basis of many of the self-pulsation models used today. The authors concluded that the non-linear behaviour of the gain/absorption curve with carrier density was a key effect in the generation of self-pulsation.

Many further studies were carried out on the dynamics of self-pulsation in two section lasers after the earlier work of Basov. Among the most important of these studies was the work of Harder, Lau, and Yariv [13]. They analysed the current-voltage (I-V) characteristics of split contact devices and identified a region of negative resistance in the absorber section corresponding to a large negative photocurrent at the onset of lasing. By performing a numerical analysis of the equivalent electrical circuit they showed that negative resistance could lead to pulsations which coupled to the relaxation oscillation frequency of the laser. They also went on to show that a self-pulsation laser such as this had very attractive relative intensity noise (RIN) characteristics

when used as a component in the reading head of an optical storage system.

A key paper which has been very much overlooked is that of van der Ziel, [14]. He studied self-focusing effects in pulsating AlGaAs double heterostructure lasers with 12 μm stripe widths and showed that there was a spatial modification of the lateral light intensity distribution during pulse emission. Two years later Buus published a paper reporting investigations of the effect of spatial hole burning in the carrier density distribution on the guiding properties of the optical mode [15]. While the majority of his concerns were to do with the static guiding properties of laser diodes, he does show that the guiding is time-dependent and due to the dependence of the refractive index on carrier density. He concludes that self-focusing could be used as an alternative explanation for self-pulsation in lasers where the guiding mechanism depends on the intensity.

In 1991 Yamada published one of the most quoted papers in this field, on the origins of self-pulsation in stripe geometry lasers [16]. In this paper he described a rate equation model which is based on the type of model previously used by Basov, to describe self-pulsation in two-section lasers. In this model the active layer was divided into two regions, a central pumped gain region directly beneath the electrical contact, and two unpumped regions at either side. The tails of the optical mode propagating along the cavity overlapped with these unpumped regions which acted as saturable absorbers and gave rise to self-pulsation. Most of the more recent studies dealing with self-pulsation in stripe geometry lasers have ultimately been based on this model.

2.5.3 Other types of Self-Pulsating Lasers

Recently self-pulsation has been a topic of intense study for potential applications in telecommunications systems since Barnsley [17] showed it was possible to synchronise self-pulsation lasers to the clock frequency of a return

to zero (RZ) encoded optical data stream. Very high frequency self-pulsation (up to 64 GHz) has been observed in multi-section DFB lasers [18]. Mode beating was suggested as one possible explanation for this behaviour [19]. Other explanations for the existence of high frequency self-pulsation in DFB lasers have included spatial instabilities in the longitudinal power distribution of lasing mode [20] and negative differential gain [21].

Very recently, self-pulsation has been observed in vertical-cavity surface emitting lasers [22]. In this case the origin of the pulsations was postulated to be due to spatially localised saturable absorption near the output facet.

2.6 Self-Pulsation in CD Laser Diodes

The main application of self-pulsating lasers has been optical storage. Self-pulsating lasers are used for this application because they have a short coherence length. As a result, they are very insensitive to optical feedback and have a very low relative intensity noise. The conventional CD laser diode is a narrow stripe double heterostructure with a bulk active region, fabricated in the GaAs/AlGaAs material system, with lasing emission typically centred around $\lambda = 780$ nm. An illustration showing the transverse cross-section of a typical laser, is shown in Fig. 2.10. The gain section is pumped through a p-type electrical contact, and has the following approximate dimensions: 250 μm long, 2 μm wide, and 0.2 μm thick. The n-type current blocking layer defines the width of this gain section and gives rise to two lateral unpumped regions at either side. It is these unpumped sections that are proposed to act as saturable absorbers. The tails of the optical mode propagating along the cavity overlap with these unpumped regions.

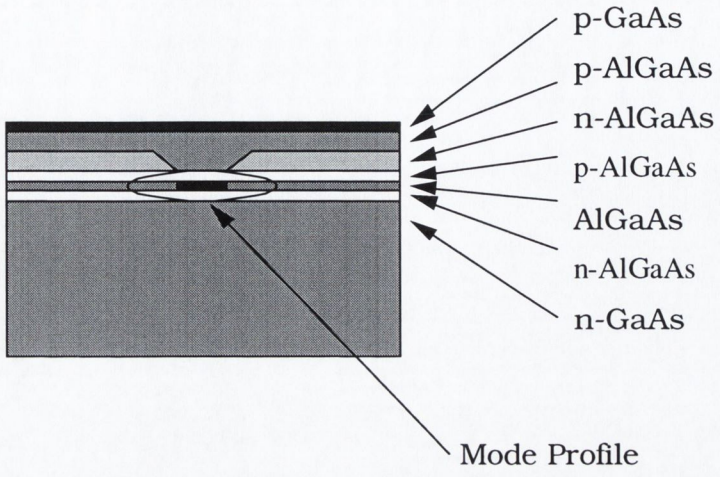

Figure 2.10: Illustration showing the transverse cross-section of a CD laser.

2.6.1 Frequency Behaviour

A typical radio frequency (RF) power spectrum of a self-pulsation CD laser is shown in Fig. 2.11. The power spectrum is characterized by a main peak at 1.03 GHz which corresponds to the self-pulsation frequency, ν_{sp}. The following peaks at 2.07 GHz, 3.10 GHz, 4.14 GHz, and 5.18 GHz are higher order harmonics. The behaviour of the free-running self-pulsation frequency with bias current is generally highly linear. However, close to the threshold current, the curve can exhibit some nonlinear behaviour, as seen in Fig. 2.12. This non-linear behaviour near threshold has been a topic of considerable interest for some time. Recently, a theoretical investigation into this phenomenon was performed [23], using a similar rate equation model to that described in section 2.7.2. A stability analysis was performed on the rate equations and it was concluded that the self-pulsation frequency bias current parameter space was bounded on both sides by what is known mathematically as a Hopf bifurcation. Either side of this Hopf bifurcation the CW solution was stable. Within the highly complex region of the curve near the lower frequency bound there is a cross-over point. Below this cross-over point the

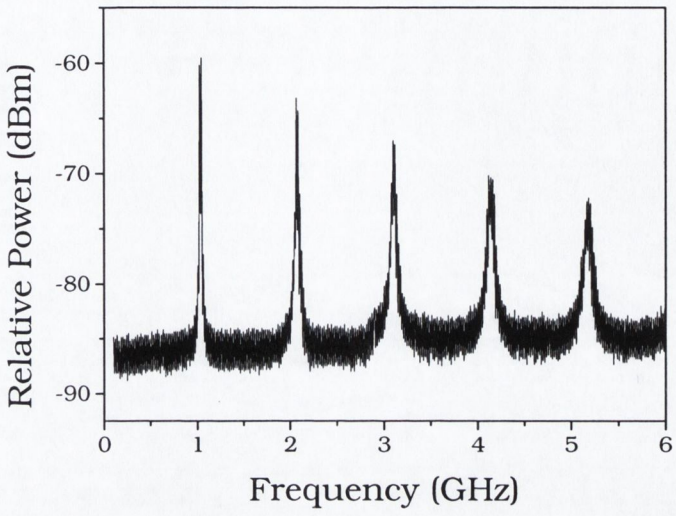

Figure 2.11: Typical RF spectrum for a commercial SHARP LT022MD self-pulsating CD laser diode recorded at a bias current of 56 mA and a heatsink temperature of 20 ^{0}C. The resolution bandwidth of the RF spectrum analyzer was 1 MHz and the video bandwidth was 10 KHz.

self-pulsation behaves as passive Q-switching oscillations, while above the cross-over point the behaviour approaches undamped relaxation oscillations.

2.6.2 Pulsewidth Behaviour and Autocorrelation as a Measurement Technique

While the RF power spectrum obviously corresponds to the frequency domain, it is also interesting to look at the behaviour in the time domain. Unfortunately, the fast time scales involved make direct measurements on a sampling oscilloscope difficult. Currently the fastest sampling oscilloscope available, has a bandwidth of 50 GHz. However, this only corresponds to a risetime of about 7 ps. One way to investigate the temporal dynamics at ps resolution is to use a streak camera. This method is discussed in detail on pg. 74 of chapter 4. Another innovative method that is often used to study the pulsewidth is to perform an intensity autocorrelation. Fig. 2.13

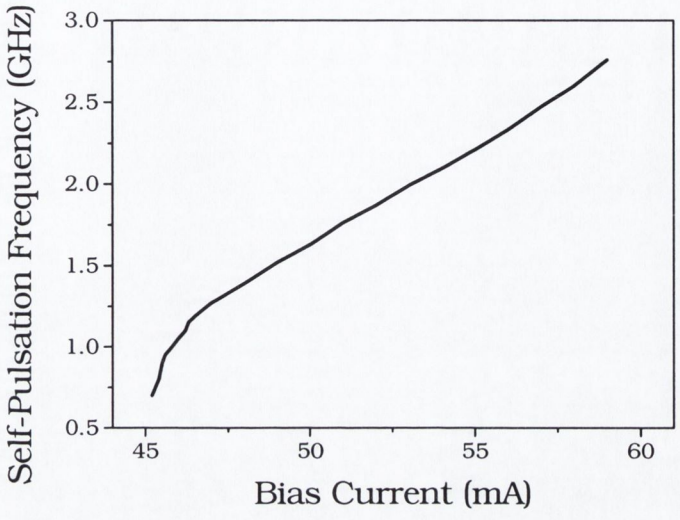

Figure 2.12: Free-running self-pulsating frequency versus bias current for typical SHARP LT022MD, recorded at a heatsink temperature of 20 ^{0}C. In order to measure the points close to threshold a small electrical modulation was applied to aid location of the resonance.

shows a schematic diagram of the autocorrelator which was used in many of pulsewidth investigations in this thesis. The basis for the autocorrelator is the Michelson interferometer. The incoming beam is divided into two equal parts by a beam splitter. The two beams are then recombined in a second harmonic crystal after one of them has passed through a variable delay. The intensity of the second harmonic signal is measured with a photomultiplier tube (PMT). An infrared filter ensures that only the second harmonic signal reaches the PMT. The purpose of the two half-wave plates is to correct any variation in power in both arms, by optimising the beam polarisation. The efficiency of second harmonic generation is maximised by making small angular adjustments to the crystal in order to ensure correct phase matching to the incoming light. The magnitude of the second harmonic signal is proportional to $\int |E^2|^2 \, dt$. If the measurement is performed with interferometric accuracy then the correlated second harmonic signal, $\mathcal{G}(\Delta t)$, is given by (2.29), where

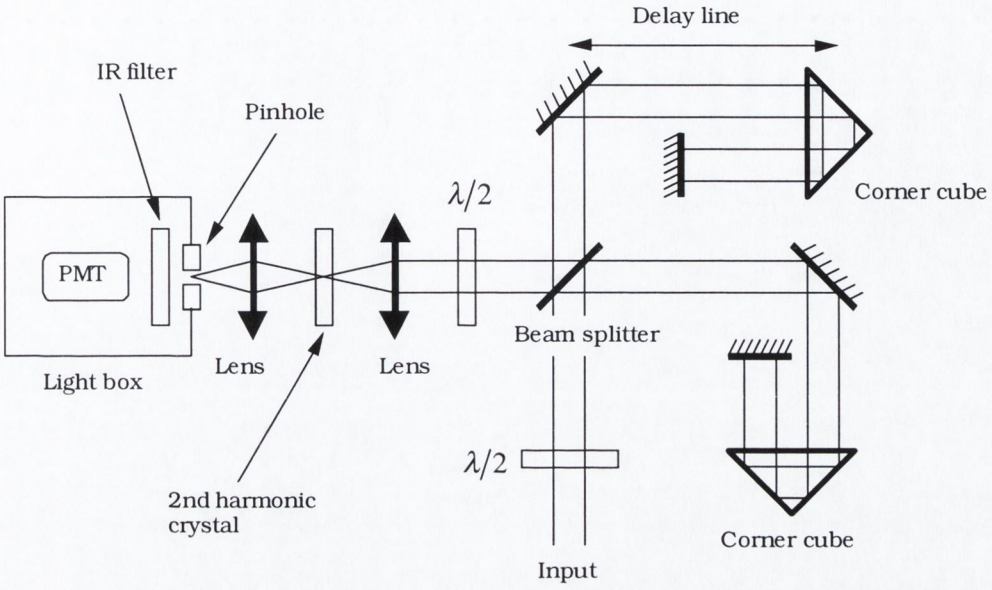

Figure 2.13: Schematic diagram of the autocorrelator used to perform pulsewidth measurements.

Δt is the time delay between the two arms of the interferometer.

$$\begin{aligned}
\mathcal{G}(\Delta t) &= \int \left|(E(t) + E(t-\Delta t))^2\right|^2 dt \\
&= \int \left|\left(\mathcal{E}(t)e^{i[\omega t+\phi(t)]} + \mathcal{E}(t-\Delta t)e^{i[\omega(t-\Delta t)+\phi(t-\Delta t)]}\right)^2\right|^2 dt \\
&= \int \Big[2\mathcal{E}^4(t) + 4\mathcal{E}^2(t)\mathcal{E}^2(t-\Delta t) \\
&\quad + 4\mathcal{E}(t)\mathcal{E}(t-\Delta t)\left(\mathcal{E}^2(t) + \mathcal{E}^2(t-\Delta t)\right)\cos\left[\omega t + \phi(t) - \phi(t-\Delta t)\right] \\
&\quad + 2\mathcal{E}^2(t)\mathcal{E}^2(t-\Delta t)\cos\left[2\left(\omega t + \phi(t) - \phi(t-\Delta t)\right)\right]\Big]\, dt
\end{aligned} \tag{2.29}$$

In the experiment described above, only the intensity correlation function was measured, and the two cosine interferometric terms average out to zero. $\mathcal{G}(\Delta t)$ then reduces to (2.30).

$$\mathcal{G}(\Delta t) = \int \left[2\mathcal{E}^4(t) + 4\mathcal{E}^2(t)\mathcal{E}^2(t-\Delta t)\right] dt = 2\int I^2 dt + 4\int I(t)I(t-\Delta t)dt \tag{2.30}$$

Finally, normalising (2.30) yields the measured second harmonic intensity autocorrelation, I_{SH}, [24],

$$I_{SH} \propto 1 + \frac{2\int I(t)I(t-\Delta t)dt}{\int I^2 dt} \tag{2.31}$$

Inspection of (2.31) reveals an ideal peak to background ratio of 3:1 for a coherent pulse. Fig. 2.14 shows a typical autocorrelation trace of a self-pulsating laser. The comb of narrow peaks riding on top of the trace are known as coherence spikes. These coherence spikes indicate coherent amplified modulation noise and are separated on the autocorrelation trace by the cavity round trip time. The width of these spikes is a measure of the temporal width of the noise fluctuations and the contrast ratio is a measure of the modulation depth. The existence of this noise also causes the peak to background ratio laser to be somewhat less than then ideal value. Since I_{SH}

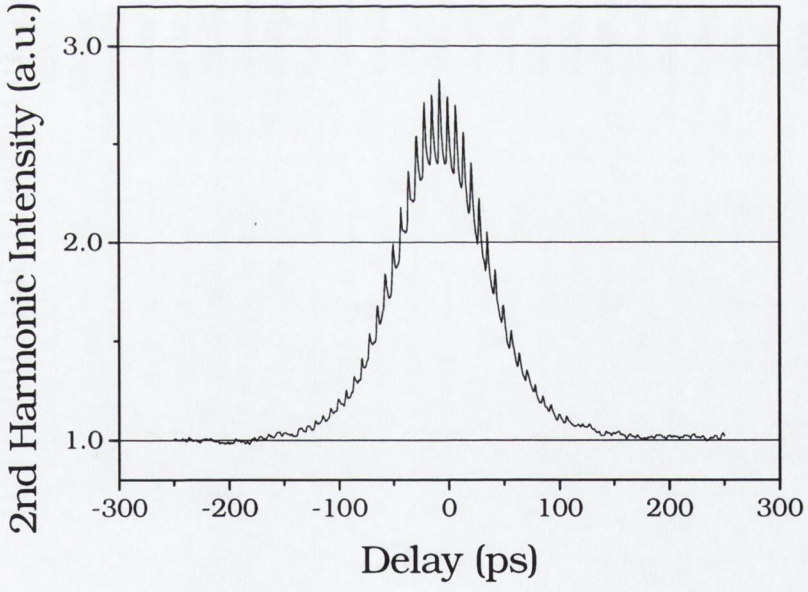

Figure 2.14: Typical autocorrelation trace for a SHARP LT022MD self-pulsating CD laser. The bias current was 56 mA and the heatsink temperature was 20 ^{0}C.

Pulse Shape	**I(t)**	**Autocorrelation Scaling Factor**
Gaussian	$\exp(-t^2)$	1.414
sech^2	$\text{sech}^2(t)$	1.543
Single-sided exponential	$\exp(-t)$ for $t \geq 0$ 0 otherwise	2

Table 2.1: Common pulse shapes I(t), and the scaling factor by which the autocorrelation trace must adjusted in order to obtain the correct pulse width.

is a symmetric function it does not provide any information about the shape of the actual optical pulse. In order to measure the full width at half maximum, (FWHM) of the optical pulse, a pulse shape must be assumed, and the FWHM of the measured autocorrelation trace multiplied by the appropriate scaling factor associated with that shape. Table 2.1 shows some of the more common pulse shapes used to fit the autocorrelation trace and their associated scaling factors. In all cases it was found that the autocorrelation trace was best fitted with a gaussian function. The FWHM of the autocorrelation is thus divided by 1.414 in order to obtain a measure of the FWHM of the optical pulse.

Fig. 2.15 shows the variation of the FWHM of the autocorrelation trace for a typical self-pulsating CD laser. The trend shown by this curve is very similar for all the CD lasers in this work. Initially the FWHM is very broad near threshold. As the bias current is increased the FWHM begins to narrow, and eventually settles down (in this case to a value of around 100 ps). Normally, the FWHM begins to broaden again as the bias current is further increased. This broadening is also associated with a change in the contrast ratio on the autocorrelation trace as the modulation depth of the optical pulses changes from 100% to a smaller value. The contrast ratio will continue to decrease until at some point the laser will eventually cease to exhibit self-pulsating and the emission becomes CW. Since this usually happens near the damage threshold for the laser it is not actually shown in Fig. 2.15.

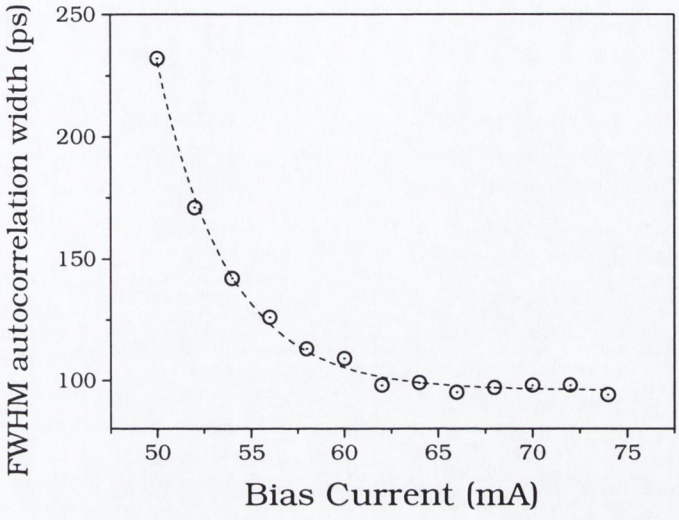

Figure 2.15: Measured FWHM autocorrelation function versus bias current. Note: The dashed line is merely a guide to the eye.

2.6.3 Optical Spectra and the Linewidth Enhancement Factor

Fig. 2.16 shows a typical above threshold optical spectrum for a self-pulsating CD laser. When compared with Fig. 2.1 on page 8, one important difference becomes very apparent. While the individual longitudinal modes in the optical spectrum of the non self-pulsating laser in Fig. 2.1 are clearly defined, the longitudinal modes in the optical spectrum of the self-pulsating laser in Fig. 2.16 are broadened to the point that they are no longer well defined. It is the short coherence length which results from the broad spectral width that makes these devices attractive for data storage applications. There are a number of important reasons for this broadening effect. Firstly, since the emission from the laser is not CW, significantly more fourier components are required to describe the optical pulse. This effect can be seen very clearly in the optical spectrum of a laser which emits very short (sub picosecond) optical pulses. In fact, the temporal width of an optical pulse is ultimately

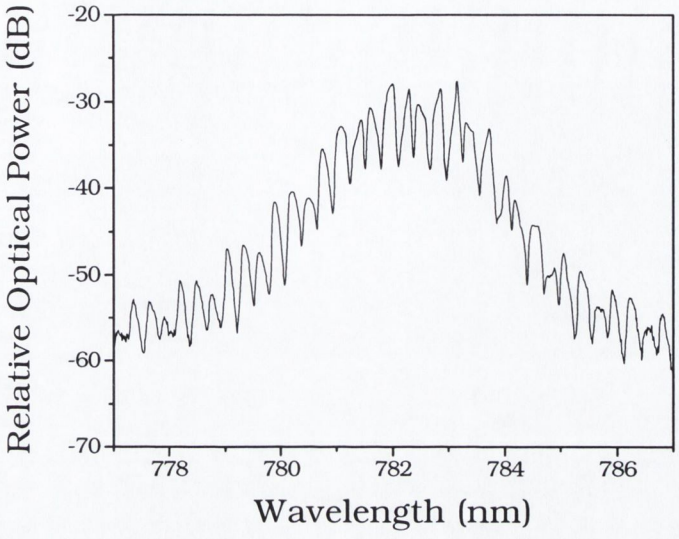

Figure 2.16: Typical above threshold spectrum of a commercial SHARP LT022MD self-pulsating CD laser diode recorded at a bias current of 56 mA and a heatsink temperature of 20 ^{0}C.

limited by the bandwidth of the gain spectrum. For example, a sub femtosecond pulse would require a gain bandwidth stretching down into the x-ray region of the electromagnetic spectrum. The second mechanism which results in a broadening of the longitudinal mode spectrum is the relationship between the optical gain and the refractive index. These two quantities are inextricably linked through the Kramers Kronig relations. Any change in the imaginary part of the complex susceptibility (gain or loss) will be accompanied by a corresponding change in the real part (refractive index), and vice versa. Since the laser is exhibiting self-pulsation, and the carrier density in the active region changes during the evolution of each pulse, there will be a corresponding change in the gain and hence the refractive index. The net result is that there is a wavelength shift as the optical pulse is emitted, [25].

The magnitude of this coupling between carrier-concentration induced variations of the real and imaginary parts of the complex susceptibility is

one of the fundamental parameters for semiconductor lasers. It is quantified by a parameter known as the linewidth broadening (or enhancement) factor. The linewidth broadening factor, α, can be defined in its most fundamental form by (2.32), [26].

$$\alpha = -\frac{d\left[\mathrm{Re}\left(\chi(n)\right)\right]/dn}{d\left[\mathrm{Im}\left(\chi(n)\right)\right]/dn} \tag{2.32}$$

The sign in Eq. (2.32) is chosen so that α is positive at semiconductor laser wavelengths. In most practical cases the carrier induced contribution to both the refractive index and the imaginary part of the permittivity is much smaller than the refractive index in the absence of carriers, and thus Eq. (2.32) is equivalent to Eq. (2.33),

$$\alpha = -2k\frac{d\mu/dn}{dg/dn} \tag{2.33}$$

where k is the free-space wave vector, μ is the refractive index, and g is the gain, [27].

The are many ways to measure the linewidth broadening factor of a laser diode, but one convenient method in the case of self-pulsating lasers is to make use of the relationship between α and the large signal modulation time-bandwidth product,

$$\Delta\nu\Delta t = \frac{2\ln 2}{\pi}\sqrt{1+\alpha^2} \tag{2.34}$$

where $\Delta\nu$ is the spectral linewidth FWHM of the dynamic frequency spectrum and Δt is the temporal FWHM of the optical pulse, [27]. This formula is based on the assumption that the optical pulse has a Gaussian shape, which is the best fit based on the autocorrelation results. Similar formulae have been derived for non-Gaussian shaped optical pulses, [28]. In this case, α was calculated using the pulsewidth measurements derived from the previously mentioned autocorrelation technique, and spectral linewidth measurements under the same bias conditions.

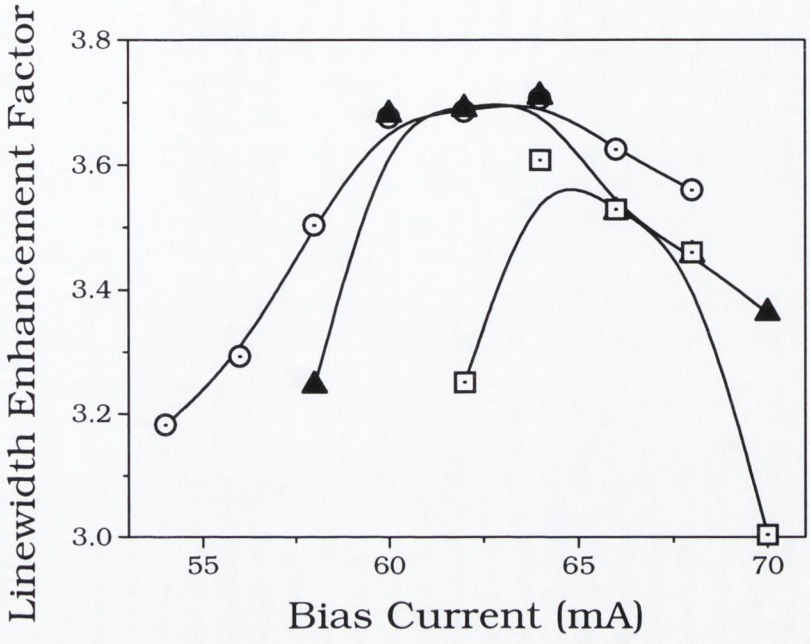

Figure 2.17: Measured Linewidth Enhancement Factor, α, for three longitudinal modes versus bias current. Note: The lines are merely guides to the eye.

α was measured for a number of different bias currents. Fig. 2.17 shows the variation of α with bias current for 3 longitudinal modes. The estimated values of α fall within the range of the relevant values quoted in the literature and to the best of my knowledge are the first experimental measurement of this quantity in self-pulsating CD lasers.

2.7 Describing Self-Pulsation in CD Lasers in Physical Terms

2.7.1 The Two-Section Laser as an Illustrative Model

The first attempt to model self-pulsation was by Dixon and Joyce [12] in 1979. For mathematical convenience they divided the laser into two sections, an end section of length $2L_E$ and a bulk section, with carrier densities n_E and n_B respectively. This is illustrated in Fig. 2.18. An average photon

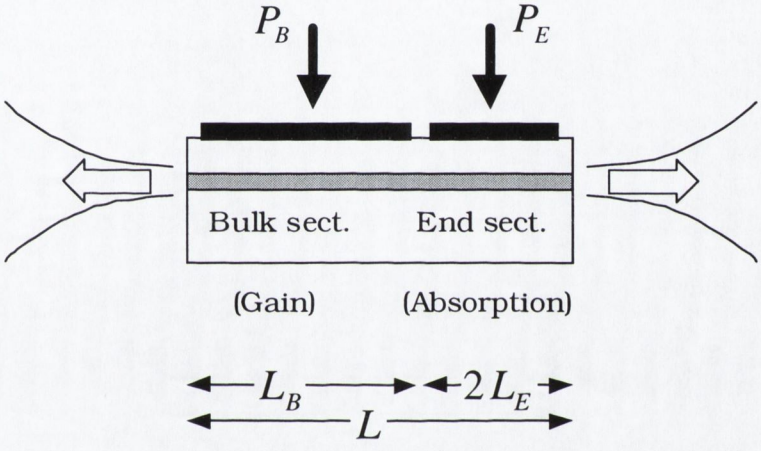

Figure 2.18: Illustration showing the longitudinal cross-section of a two section laser.

density P was assumed throughout the cavity. A coupled rate equation set (2.35)-(2.37) is used to describe the temporal evolution of these quantities.

$$\frac{dn_E}{dt} = P_E - \frac{n_E}{\tau_E} + \Gamma\alpha\nu_g P \tag{2.35}$$

$$\frac{dn_B}{dt} = P_B - \frac{n_B}{\tau_B} - \Gamma g\nu_g P \tag{2.36}$$

$$\frac{dP}{dt} = f\left(\frac{n_B}{\tau_B}\right) + (G - \alpha_m - \alpha_s)\Gamma\nu_g P \tag{2.37}$$

The form of these equations is very similar to equations 2.27 and 2.28 derived at the end of section 2.3.2. Here, two equations describe the temporal evolution of the carrier densities in the individual sections. P_E and P_B are

simply the pump rates for the respective sections, followed by the respective carrier recombination rates. The end-region loss, $\alpha(n_E)$, and the bulk-region gain, $g(n_B)$, combine to produce an overall cavity gain $G = -2\alpha(n)L_E/L + gL_B/L$ where $L_B = L - 2L_E$, the length of the bulk-region. f is the fraction of the spontaneous emission which joins the stimulated emission, and is similar to the term β_{sp} in Eq. (2.28). α_m is the mirror loss and α_s is the scattering loss.

2.7.2 Adapting the two-section laser model for the CD laser

Most of the recent models which have been used to study self-pulsation and its applications in CD lasers have been based on the model of Yamada [16]. The ultimate origin of this model lies in the original work of Dixon and Joyce which has been outlined in the previous section. The active region is treated as two separate sections, a cental gain region defined by the dimensions of the pumping electrode, and two unpumped regions at either side. The carrier density in the side regions is treated as one lumped value. The dynamics can then be described by a set of three coupled rate equations.

$$\frac{dN_1}{dt} = \frac{I_b}{eV} - \gamma_{e1}(N_1)N_1 - \Gamma_1(N_i)G(N_1)P - \frac{N_1 - N_2}{\tau_{12}} \tag{2.38}$$

$$\frac{dN_2}{dt} = -\gamma_{e2}(N_2)N_2 - \Gamma_2(N_i)G(N_2)P - \frac{N_2 - N_1}{\tau_{21}} \tag{2.39}$$

$$\frac{dP}{dt} = \left[\Gamma_1(N_i)G(N_1) + \Gamma_2(N_i)G(N_2) - \frac{1}{\tau_p}\right]P + \beta\sum_i B(N_i)N_i^2 \tag{2.40}$$

Inspection of these equations reveals that they show a striking similarity to equations (2.35)-(2.37). There are however a number of significant differences. Eq. (2.38) contains no electrical pumping term, unlike Eq. (2.35). Also, there is an extra term in both Eq. (2.38) and (2.39), which accounts for the diffusion of carriers between the two idealised regions. The rate of diffusion from region to region is characterised by a diffusion time. The magnitude of this diffusion rate will also depend on the relative carrier densities

in each section. One very major difference is that the lateral optical confinement, Γ, is no longer treated as constant since the guiding depends on the two carrier densities. It must therefore be re-calculated after each iteration step. This is a key innovation, and there is a common thread with the work in chapter 4.

A detailed discussion of this type of model is presented in chapter 3, and the full meaning of all the terms is explained there.

2.7.3 Mechanisms for Self-Pulsation in CD Lasers: Conventional Wisdom

The culmination of the previous two sections has been the development of the CD rate equation laser model just presented, and conventional self-pulsation in CD lasers is understood in these terms. However, it is perhaps the very success of this model that may be one of the greatest impediments in the way of further progress. Since the underlying mechanism driving this model is saturable absorption, many groups have continued further along these lines in their attempts to achieve self-pulsation in new structures by enhancing saturable absorption effects in their devices. On the other hand, it appears that the early work of van der Ziel and Buus, on time-dependent waveguide modifications in wide stripe lasers, has been largely ignored. Certainly, at the time of this work the major thrust of the research in this field was to engineer guiding instabilities and phenomena such as bistability and self-pulsation out of laser diodes. It is only recently with the apparent lack of progress in achieving self-pulsation in new materials, that the research goals have changed.

Significant progress has certainly been made on the basis of these models. However progress has slowed, particularly with respect to self-pulsation in new materials, such as AlGaInP. This suggests that re-examining the self-pulsation hypothesis may be appropriate. Regarding this, a reasonable approach is to return to the AlGaAs material system, since the devices are well behaved and the essential physics is not masked by pathological and even spurious electrical effects.

Chapter 3

The Effect of Temperature on Self-Pulsation in CD Laser Diodes

3.1 Rationale

According to the current consensus in the literature, the cause of self-pulsation in CD lasers is saturable absorption. In these devices the transverse electromagnetic field extends from an electrically pumped region of the stripe layer to the unpumped regions at either side. It is these unpumped regions which are thought to behave as saturable absorber sections and the self-pulsation arises from the interaction of the confined electromagnetic field with this non-uniformly pumped material. In short, when the number of carriers in the saturable absorber sections is small, the losses are quite large, enabling a population inversion to build up. As time progresses the number of carriers in these sections builds up until the lasing condition is reached. At this point a pulse is emitted, which depletes the population of carriers and the cycle begins again. In this picture, controlling the processes by which carriers are generated in these saturable absorber sections is the key to controlling self-pulsation in CD type structures. The two dominant processes by which carriers are generated in these saturable absorber sections are by absorption

of the light generated in the gain region and charge carrier diffusion. The aim of the work presented in this chapter is to assess both experimentally and by calculation the influence of carrier diffusion in CD lasers. Temperature is used as a probe, since carrier mobility and hence carrier diffusion is highly temperature dependent.

3.2 Experimental Details

This section describes both the details of the CD laser which was studied, and the experimental apparatus which was used to look at the behaviour of these lasers over a wide temperature range.

The devices tested were SHARP CD laser diodes, model LT022MD, which were the most readily available commercial self-pulsating CD laser diodes. The structure of these devices is quite well known and is illustrated in the inset of Fig. 3.1. This type of laser has a Fabry-Perot cavity with a bulk AlGaAs active region with emission wavelength around, $\lambda = 800$ nm. The gain section is pumped through a p-type electrical contact and has the following approximate dimensions: 250 μm long, 2 μm wide and 0.2 μm thick. The two n-blocking layers confine the current to the central region of the active layer, which gives rise to two lateral unpumped regions at the sides to achieve the saturable absorber regions. The optical mode propagating along the laser cavity overlaps these saturable absorbing regions.

As illustrated in Fig. 3.1, this component was placed in an open cycle liquid nitrogen cryostat which allowed temperature tuning in the range $77\ \mathrm{K} \leq T \leq 370\ \mathrm{K}$. The emitted light was then collected by a 0.65 NA microscope objective and passed through a 36 dB isolator, to avoid any feedback which might perturb the self-pulsation. At the isolator output the light was monitored by either an integrating sphere or a 60 GHz bandwidth photodiode. The integrating sphere was used to record calibrated, time averaged, power measurements. The 60 GHz photodiode was used to transform the op-

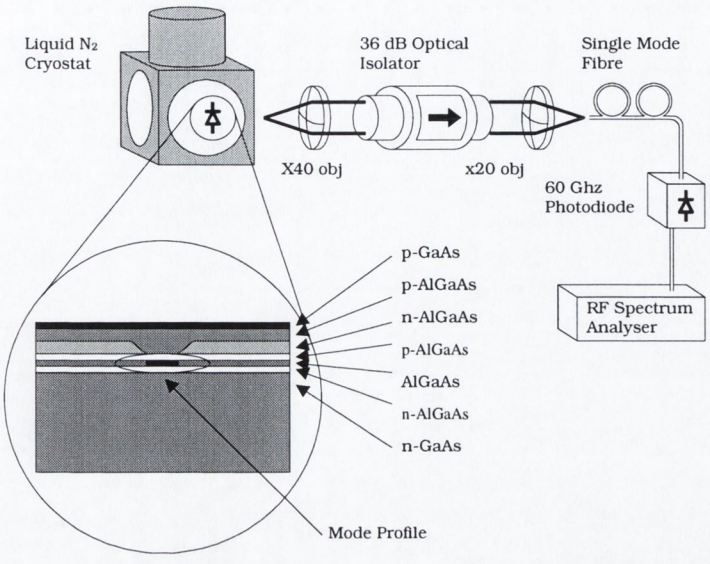

Figure 3.1: Schematic of the experimental set-up. Inset shows the structure of the self-pulsating CD laser.

tical emission to an electrical signal which could be observed with a 22 GHz bandwidth RF spectrum analyser (model HP 8563A).

3.3 Experimental Results

The following subsections describe some of the more interesting experimental results obtained when the temperature dependence of the self-pulsating behaviour was investigated.

3.3.1 Light-Current Curves and the Behaviour of Threshold Current

One of the first measurements which is made on a laser diode, is an estimation of the threshold current (I_{th}). This is the point at which the net gain becomes equal to the cavity losses and the significant component of the emitted light is due to stimulated emission. This is usually accomplished by recording a light-current (LI) curve. I_{th} is indicated by a discontinuity in the LI curve

above which the intensity of the emitted light usually behaves linearly with bias current, according to the expression

$$P = \eta_d \frac{h\nu}{e} (I - I_{th}) \ . \tag{3.1}$$

where P is the optical power, I is the bias current, and h, ν and e have their usual meanings. The quantity η_d is called the differential quantum efficiency. It is proportional to the slope of the LI curve which can be easily demonstrated by differentiating Eq. (3.1), to give the expression

$$\eta_d = \left(\frac{h\nu}{e} \right)^{-1} \frac{dP}{dI} \ . \tag{3.2}$$

η_d includes the internal quantum efficiency, the mirror losses, the material losses, and the modal gain.

Fig. 3.2 shows a series of LI curves which were recorded at 20 K intervals for temperatures, T, in the range 77 K $\leq T \leq$ 370 K. The lasing threshold current increases with increasing temperature and varies in the range 7 mA $\leq I_{th} \leq$ 80 mA. Careful study of this plot also shows that η_d decreases with increasing temperature, thus indicating that the laser is more efficient at lower temperatures. The more significant reasons for this behaviour can be explained as follows. As the temperature increases the peak gain at a given carrier density is reduced requiring a higher bias current to achieve lasing threshold. Furthermore since there is an additional Joule heating effect associated with the increased current, non-radiative effects in carrier recombination further add to the escalation in lasing threshold.

Empirically, the typical temperature dependent threshold behaviour for AlGaAs laser diodes is usually well described by Eq. (3.3), [4, 8].

$$I_{th} = I_0 \exp \left(\frac{T}{T_0} \right) \tag{3.3}$$

where I_0 is the intercept on the threshold current axis, when the threshold current is plotted against temperature on a semi-logarithmic graph. T_0 is a

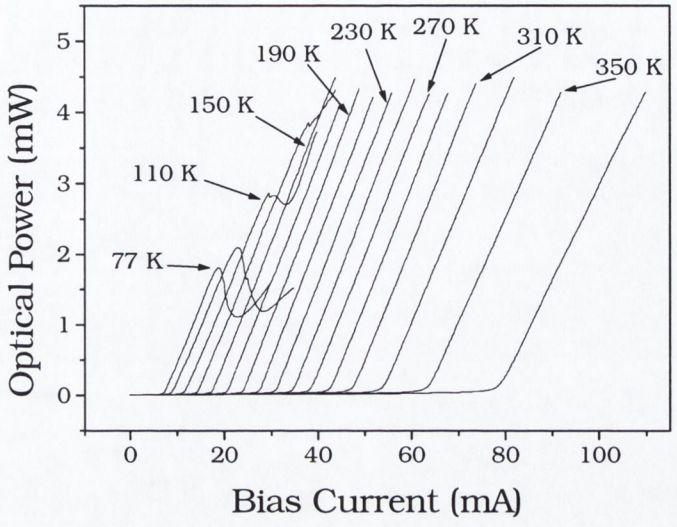

Figure 3.2: Typical Light-Current curves for a SHARP LT022MD in the temperature range, T, 77 $K \leq T \leq$ 370 K. Note: Only every second curve is labelled on the graph.

parameter which is known as the characteristic temperature and describes the sensitivity of threshold current to temperature. Fig. 3.3 shows the variation of threshold current with temperature on a semi-logarithmic plot for this laser diode. For the data shown in this figure, when fitted to the exponential form described by Eq. (3.3), a smaller value of T_0 was estimated at low temperatures ($T_0 = 85$ K) than for high (room) temperatures ($T_0 = 185$ K).

Such behaviour is unusual in Fabry-Perot lasers emitting at this wavelength, which usually obey Eq. (3.3) very closely over the entire temperature range in question. However, this behaviour is typical in the type of CD laser being studied. There are many reasons why the temperature dependence of threshold may deviate from Eq. (3.3). One well known mechanism in longer wavelength lasers is Auger recombination, though this is considered to be negligible in GaAs materials [4, 8]. Another mechanism which has often been advanced to explain deviations from Eq. (3.3) is carrier leakage. However

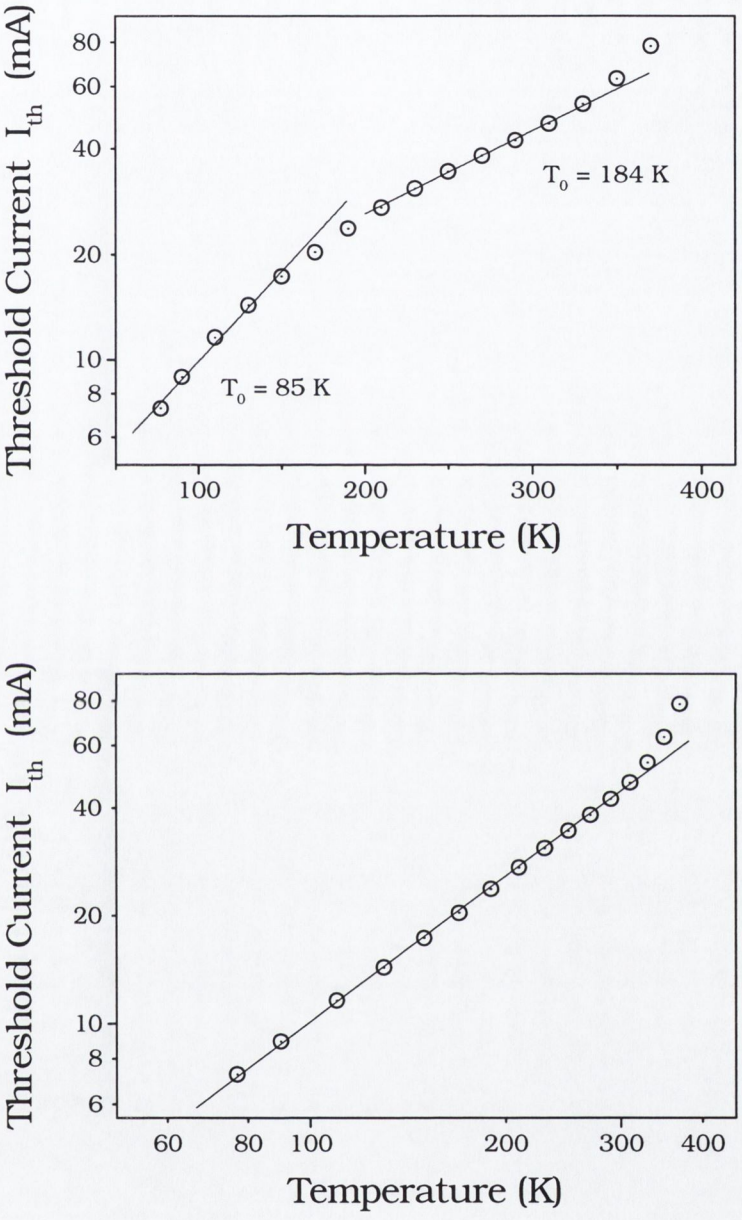

Figure 3.3: (Top) Semi-logarithmic plot of I_{th} versus temperature, and (bottom) fully logarithmic plot of I_{th} versus temperature indicating a power law dependence over the temperature range, T, 77 K $\leq T \leq$ 350 K.

as the temperature increases the more energetic carriers are more likely to escape from the heterojunction, thereby increasing the leakage current, and causing the threshold current to become more temperature sensitive with increasing temperature. It is clear from Fig. 3.3 that the measured values of T_0 show the opposite trend and consequently the temperature dependence of threshold cannot be explained just by carrier leakage.

Considerably more insight can be obtained by re-plotting the data on a double logarithmic plot. The straight line fit over the temperature range, T, 77 K $\leq T \leq$ 350 K indicates a power law dependence. With a little digression it is possible to explain this behaviour. The total radiative recombination rate on transition from the conduction to the valance band, R_{cv}, is given by the general expression, [29]

$$R_{cv} \propto \int_{E_g}^{\infty} \rho_{red}(E) f_c (1 - f_v) d(E_c - E_v). \tag{3.4}$$

Here, f_c and f_v are occupation probabilities of the conduction and valence bands, which for are described by Fermi functions. For degenerate material such as an unstrained intrinsic active region, and for $T \gg 0\ K$, the energy dependence of the product of these Fermi functions will be relatively insensitive to temperature changes after integration. The other term inside the integral is the reduced density of states, $\rho_{red}(E)$. The energy dependence of the density of states for a particular band depends on whether the material is bulk (3D) or whether the material has been confined thus reducing the number of dimensions, d by using quantum well (2D), quantum wire (1D) or quantum dot (0D) structures. A general expression for the energy dependence is given by, [29],

$$\rho(E) = \frac{s V_d (m_1 m_2 \ldots m_d)^{\frac{1}{2}}}{\Gamma(\frac{d}{2})(2\pi\hbar^2)^{\frac{1}{2}}} (E - E_0)^{\frac{d}{2}-1}. \tag{3.5}$$

Here s is the spin factor, V_d is the d-dimensional *volume* (i.e. for 2-D struc-

tures this would be an area) which is given by the equation (3.6).

$$V_d(r) = \left[\frac{\pi^{\frac{d}{2}}}{\Gamma(1+\frac{d}{2})} \right] r^d \tag{3.6}$$

The m_i in equation (3.5) are the effective masses for the different directions and the zero subscript on E_0 in the integral refers to lowest energy state of the band. By inspection it is easy to see that on integration of (3.5) that the energy dependence and hence the temperature dependence of R_{cv} will be $d/2$. The temperature dependence of I_{th} can then bean inferred from the below threshold steady-state carrier rate equation:

$$\frac{\eta_i I_{th}}{eV} = (R_{sp} + R_{nr} + R_l)_{th} \tag{3.7}$$

where R_{sp} is the spontaneous emission rate, R_{nr} is the nonradiative recombination rate, and R_l is the rate of carrier pairs lost through leakage. Thus for 3D bulk lasers made from high quality material with negligible nonradiative recombination the temperature dependence of threshold is expected to scale as $T^{\frac{3}{2}}$ while for quantum well structures the temperature dependence is expected to scale linearly, [30, 31]. In this case the slope of this curve was found to be 1.3, which is closest to the theoretical bulk value of 1.5. Now, since leakage current has already been discounted, and I_{th} clearly exhibits a power law dependence over the temperature range in question, it is reasonable to assume that non-radiative recombination is small relative to the other recombination processes in this type of CD laser.

3.3.2 Frequency Behaviour

The amount of information which can be recovered from steady state measurements, such as the LI behaviour, is limited. Of more interest with respect to self-pulsating lasers is the dynamic response. With this object in mind, one of the first tasks is to investigate the parameter space over which self-pulsation is sustained by a CD laser. The behaviour of several CD lasers was

examined in range 77 K $\leq T \leq$ 370 K. For all of the devices self-pulsation was found to extinguish between 100 K and 130 K. Fig. 3.4 shows a typical plot of the variation of self-pulsation frequency with bias current over range 110 K $\leq T \leq$ 370 K. It should be noted that the upper limit of 370 K

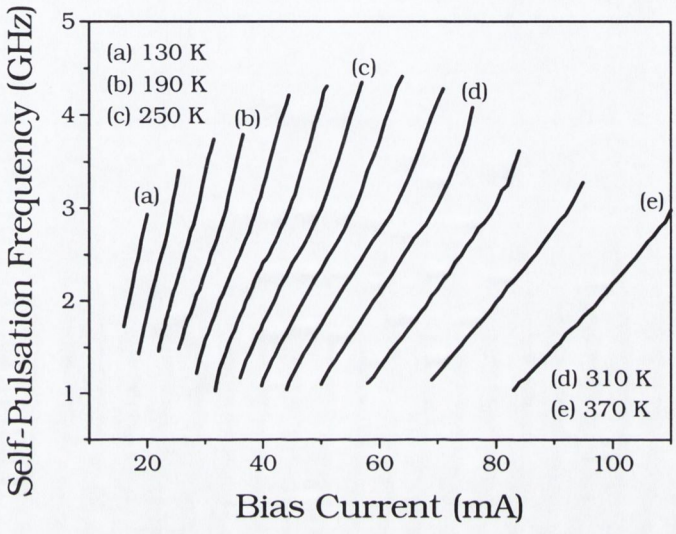

Figure 3.4: Self-Pulsation frequency versus bias current measured at 20 K intervals, in the temperature range T, 110 K $\leq T \leq$ 370 K. Note: Only every third curve is labelled on the graph.

was determined by the packaging and was not the upper temperature at which self-pulsation was found to extinguish. The relationship between self-pulsation frequency and bias current is highly linear and is more sensitive to changes in bias current at lower temperatures. Fig. 3.5 shows the same data re-plotted (as is conventional) as a function of normalised bias current. These results are interesting for a number of reasons. Firstly, self-pulsation has often been described as a destabilised relaxation oscillation. For a simple one-section laser this is described by a square root law and can be obtained

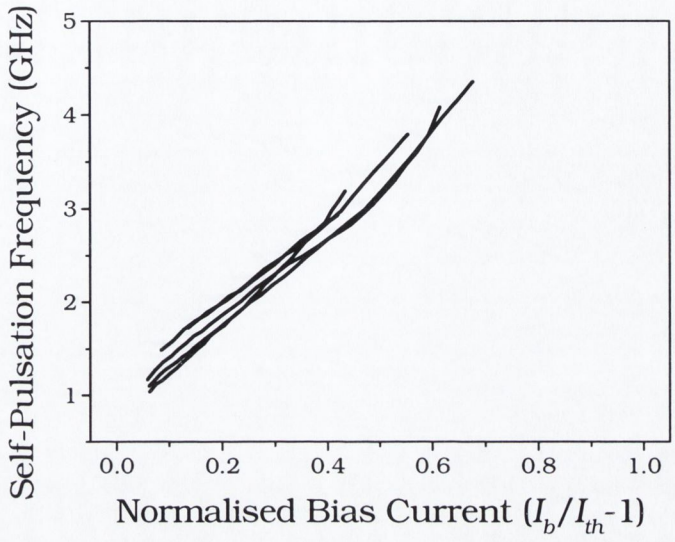

Figure 3.5: Self-Pulsation frequency versus normalised bias current in the temperature range T, 110 K $\leq T \leq$ 370 K. Note: For clarity only a few curves are shown.

from a small signal analysis of the rate equations [32]:

$$\Omega \approx \sqrt{\frac{dG}{dN}\left(\frac{I_b - I_{th}}{eV}\right)} \approx \sqrt{\frac{1}{\tau_P \tau_N}\left(\frac{I_b}{I_{th}} - 1\right)}. \tag{3.8}$$

Inspection of Eq. 3.8 shows that it a carrier lifetime term, τ_N, which is highly temperature dependent. However, there is little impact of temperature on the slopes or intercept of the curves in Fig. 3.5. Eq. 3.8 is only strictly valid for simple one-section lasers, but it is possible to derive a more complicated expression which is valid for the 3 rate equation system used to model CD lasers, [32]:

$$\Omega \approx \sqrt{\sum_i \Gamma_i^2 G_i P \frac{dG_i}{dN_i} + \sum_i \Gamma_i G_i^2 P X_i} \tag{3.9}$$

where,

$$X_i = \gamma_{ei} + N\frac{d\gamma_{ei}}{dN_i} + \Gamma_i P \frac{dG_i}{dN_i} + \frac{d\Gamma_i}{dN_i} P G_i + \frac{1}{\tau_{ij}} \tag{3.10}$$

with $i, j = 1, 2$, and $i \neq j$. While Eq. 3.9 is considerably more complicated the physics is still essentially the same. It contains many terms which are highly temperature dependent while at the same time this temperature dependence is not reflected in the experimental data. This observation suggests that it is an oversimplification to describe self-pulsation as just a destabilised relation oscillation and that the physics is considerably more complicated.

3.4 Adapting the CD Laser model to include Temperature

It was demonstrated in section 2.7.2 how a simple rate equation model could be used to describe self-pulsation in a CD laser. However this type of model does not explicitly contain a temperature dependence. In order to simulate the experimental findings it was necessary to modify the existing CD model in order to display the influence of temperature on the self-pulsation behaviour. This was done in a phenomenological fashion. By inspection, the various terms in the CD rate equation model which might have a temperature dependence were identified. These terms are highlighted in equations (3.11 - 3.13).

$$\frac{dN_1}{dt} = \frac{I_b}{e} - \gamma_{e1}(N_1, T)N_1 - \Gamma_1(N_i, T)G(N_1, T)P - \frac{N_1 - N_2}{\tau_{12}(T)} \tag{3.11}$$

$$\frac{dN_2}{dt} = -\gamma_{e2}(N_2, T)N_2 - \Gamma_2(N_i, T)G(N_2, T)P - \frac{N_2 - N_1}{\tau_{21}(T)} \tag{3.12}$$

$$\frac{dP}{dt} = \left[\Gamma_1(N_i, T)G(N_1, T) + \Gamma_2(N_i, T)G(N_2, T)\right]P - \frac{P}{\tau_P} + \beta \sum_i B(N_i, T)N_i^2 \tag{3.13}$$

As before, Γ_i is the confinement factor and G is the gain or absorption in the active layer. τ_p is the photon lifetime which is given by the expression:

$$\tau_P^{-1} = \nu_g \left[\alpha_{int} + \frac{1}{L} \ln\left(\frac{1}{R}\right)\right] \tag{3.14}$$

where ν_g is the group velocity, α_{int} the internal losses, L the cavity length, and R the reflectivity of the output mirror. β represents the coupling efficiency of the spontaneous emission to the lasing mode, and $B(N_i, T)$ is the bimolecular recombination rate. I_b is the injection current into the gain section, e is the electronic charge, and $\gamma_{ei}(N_i, T)$ is the carrier recombination rate. $\tau_{xy}(T)$ is the carrier diffusion time between section x and section y. In each case the temperature dependence was included by making simple physical approximations which are outlined in sections 3.4.1 - 3.4.3.

3.4.1 Material Gain and Absorption

The common assumption when dealing with many rate equation models is that gain is a linear function of carrier density [16, 33]. Instead, a calculation of gain including many body effects was incorporated into the model rather than making this assumption. There are a number of reasons for incorporating the gain in this manner. Firstly this calculation results in a much more realistic value for the gain, and its dependence on temperature. Secondly the gain calculation introduces a self-consistency in the model, since the radiative recombination rates for each section from which the carrier recombination rates and spontaneous emission rates are calculated, are now determined by one calculation.

The gain was pre-calculated as a function of carrier density and temperature and was included in the laser model using two dimensional interpolation. Parabolic band structure was assumed for the light and heavy hole valence bands and the gamma, X, and L minima of the conduction band. The electron and hole Fermi functions f_c and f_v were obtained by imposing the charge neutrality condition in the undoped active region. Assuming strict k-selection the absorption and spontaneous emission rate [4, 8], were given by Eq. (3.15) and (3.16). The value of $B(N_i, T)$ was then obtained by integrating $r_{sp}(\hbar\omega)$ over all energy while due to the standard convention for rate

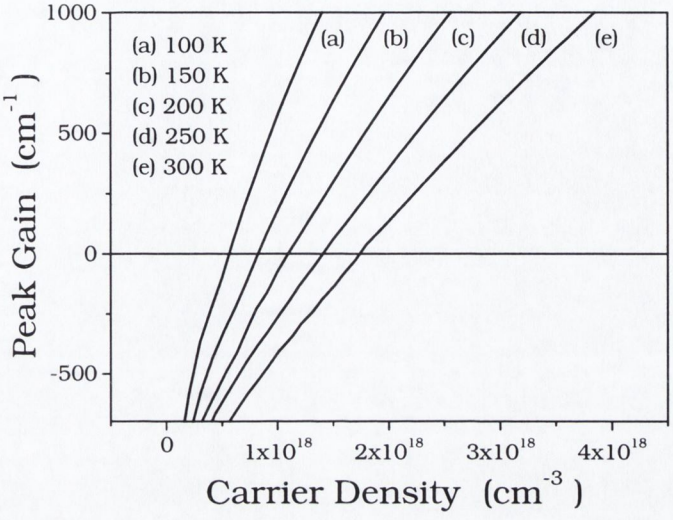

Figure 3.6: Calculated peak gain versus carrier density for five different temperatures

equation models $G = -\alpha(\hbar\omega)|_{max}$.

$$\alpha(\hbar\omega) = \int \frac{e^2 h}{2\epsilon_0 m_0^2 c n_g(\hbar\omega)} |M_b|^2 \rho_{red}(\hbar\omega)[1 - f_c - f_v] L(E_{eh}, \hbar\omega) dE_{eh} \tag{3.15}$$

$$r_{sp}(\hbar\omega) = \int \frac{4\pi n_g e^2(\hbar\omega)}{\epsilon_0 m_0^2 c^3 h^2} |M_b|^2 \rho_{red}(\hbar\omega) f_c f_v L(E_{eh}, \hbar\omega) dE_{eh} \tag{3.16}$$

$\rho_{red}(\hbar\omega)$ is the three dimensional reduced density of states and M_b is the Kane matrix element [4, 8]. The many body effects include bandgap re-normalisation and spectral broadening and are included phenomenologically. The bandgap re-normalisation [4], was included as a rigid reduction ΔE (eV), in the effective bandgap:

$$\Delta E = 1.6 \times 10^{-8} \left[2 \left(\frac{N_i}{V_i} \right)^{\frac{1}{3}} \right] \tag{3.17}$$

Spectral broadening due to carrier-carrier scattering was described using the

Lorentzian convolution given by:

$$L(E_{eh}, \hbar\omega) = \frac{1}{\pi}\left[\frac{\left(\frac{\hbar}{\tau_{in}}\right)}{(E_{eh} - \hbar\omega)^2 + \left(\frac{\hbar}{\tau_{in}}\right)^2}\right] \tag{3.18}$$

with a weak carrier concentration dependent scattering lifetime (in seconds) [34], of the form:

$$\tau_{in} = 1 \times 10^{-8}\left[2\left(\frac{N_i}{V_i}\right)^{-\frac{1}{3}}\right] \tag{3.19}$$

The peak gain, defined at the local maximum of the gain versus wavelength curve was then calculated as a function of carrier density. Fig. (3.6) shows a plot of peak gain versus carrier density for a number of different temperatures.

3.4.2 Carrier Recombination Rates

The carrier recombination rate in semiconductor material is commonly described by the quadratic expression:

$$\gamma_e = A + BN + CN^2 \tag{3.20}$$

where A is the non-radiative recombination rate, B (as before) is the bimolecular recombination rate and C is the Auger recombination rate.

In this material system Auger recombination is considered to be negligible, so the N^2 term is ignored. The carrier recombination rate γ_{ei} for section i, is thus assumed to exhibit a linear dependence on carrier number, where $A(N_i, T)$ and $B(N_i, T)$ have now some temperature dependence.

$$\gamma_{ei}(N_i, T) = A(N_i, T) + B(N_i, T)N_i \tag{3.21}$$

As already mentioned in section 3.4.1, $B(N_i, T)$ is obtained from the gain calculation. As an approximation $A(N_i, T)$ is assumed to have a linear dependence on temperature and was varied in the range $10^8 \leq A(N_i, T) \leq 5 \times 10^8$, over the corresponding temperature range $77\ K \leq T \leq 310\ K$. This approximation is acceptable since $AN \ll BN^2$ at lasing carrier densities.

3.4.3 Carrier Diffusion

The characteristic carrier diffusion time between section 1 and section 2 is usually given by expression 3.22, [16].

$$\tau_{12}(T) = \frac{w^2}{2D} \tag{3.22}$$

w is the width of the gain section, and D is the diffusion coefficient. The corresponding carrier diffusion time in the opposite direction is then proportional to the volumes of the two sections:

$$\tau_{21}(T) = \frac{V_2}{V_1}\tau_{12}(T) \tag{3.23}$$

$\tau_{xy}(T)$ inherits its temperature dependence through D, since D is defined by the Einstein relation, (3.24), which includes the highly temperature dependent electron mobility, $\mu(T)$.

$$D = 2\mu(T)k_bT\left[q\left(\frac{m_h}{m_e}+1\right)\right] \tag{3.24}$$

k_b is Boltzmann's constant and m_e, m_h are the respective effective masses of the electron and hole.

The variation of $\mu(T)$ with temperature was approximately derived from experimental data in Fig. 3.7 which was obtained from the literature, [35]. From approximately 50 K up to 300 K $\mu(T)$ vs temperature curve appears quite linear on this semi-logarithmic plot. A number of points were chosen along this line and were fitted with a simple exponential function. This exponential function was then used in the model to give the temperature variation of mobility with temperature and hence the temperature variation of the carrier diffusion times required by the rate equations.

3.5 Understanding the Results of the Model

Using the model, it was possible to simulate the experimental results presented in the previous sections, and investigate the dynamic behaviour of a CD

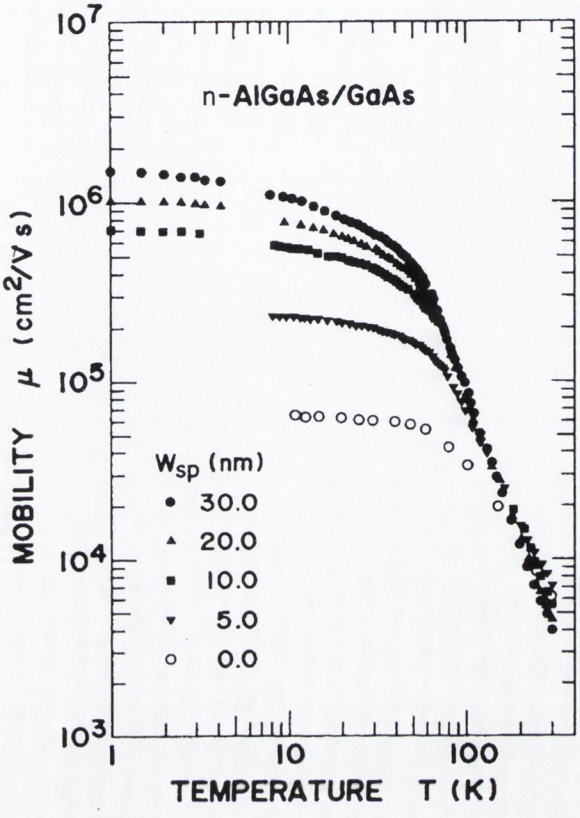

Figure 3.7: Temperature Dependence of electron mobility, μ, parameterised in terms of layer thickness, W_{sp}. Reprinted from [35].

laser as a function of bias current with respect to the sample temperature. From each simulation, after a series of a few thousand pulses (ignoring the initial relaxation transients after turn on), information such as the variation of self-pulsation frequency with temperature, was extracted. This information is presented and discussed in the following sections. Note that the value of all the parameters used has been taken from the literature, and no attempt has been made at fitting the experimental results.

3.5.1 Threshold Current Behaviour

Fig. 3.8 shows both the experimental and calculated results on the variation of threshold current with temperature for comparison, and it is clear that

there is good agreement between the two in the range 100 $K \leq T \leq 350$ K.

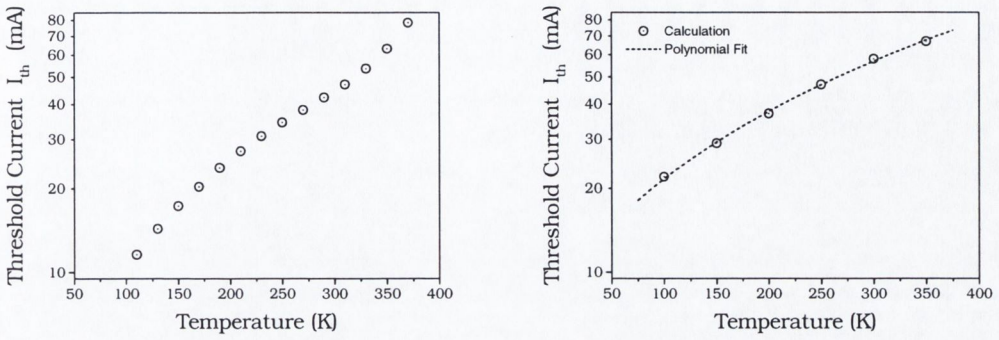

(a) (b)

Figure 3.8: (a) Semi-logarithmic plot of experimental I_{th} versus temperature and (b) Semi-logarithmic plot of calculated I_{th} versus temperature.

Based on this agreement, some qualitative hypotheses can now be made about this behaviour. Since the only temperature dependent parameters which are included in the model are gain, carrier recombination rate, and carrier diffusion, the only parameters which could cause the simulation to deviate from the empirical equation (3.3) are the carrier diffusion and the nonradiative component of the carrier recombination rate. However, since it already has been demonstrated that the threshold exhibits a power law dependence over the most of the temperature range in question, it can also be concluded that nonradiative recombination does not play a significant role in the the temperature dependence of I_{th}. Close inspection of Fig. 3.8 (a) and (b) reveals that the two curves begin to deviate above 350 K. It is very likely that this deviation and obvious inflection point in the experimental curve at higher temperatures indicates the onset of leakage currents.

3.5.2 Frequency Behaviour

Fig. 3.9 shows both the experimental and calculated results on the variation of self-pulsation frequency with bias current, as well as normalised bias cur-

rent for different temperatures. While the calculated relationship between

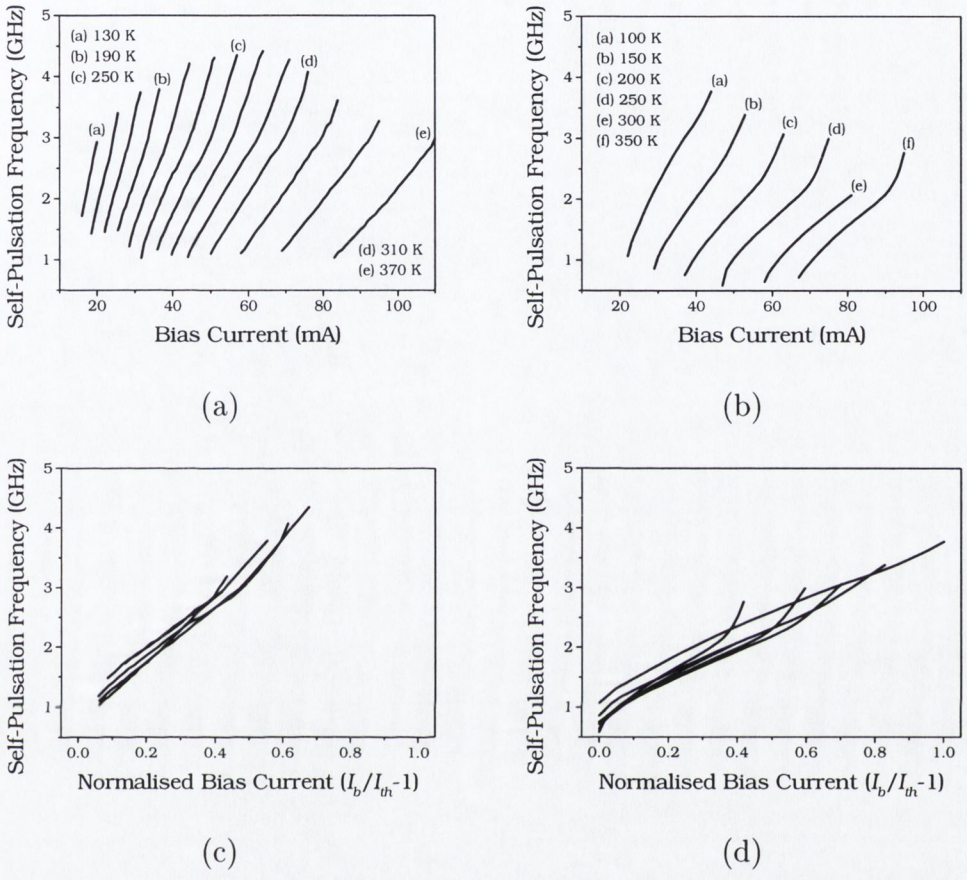

Figure 3.9: Self-pulsation frequency versus bias current, (a) Experimental results and (b) Calculated results. Self-pulsation frequency versus normalised bias current, (c) Experimental results and (d) Calculated results.

the self-pulsation frequency and bias current in (b), is not as linear as experimentally observed in (a), both the experimental and calculated trends show strong agreement. Moving on to (c) and (d), the slope of both curves is highly independent of temperature. Over this temperature range, carrier diffusion which plays a strong role in the damping of relaxation oscillations [16], increases dramatically over the range $50\ K \leq T \leq 370\ K$ due to the increase in mobility. This change however does not impact the self-pulsation frequency variation with normalised bias current.

3.6 Summary and Discussion

In this chapter both experimental and theoretical investigations of the temperature dependence of a self-pulsating CD laser diode have been presented. It has been shown that temperature can be phenomenologically included in a rate equation model by making very simple physical approximations, and that this model can be used to adequately predict the macroscopic details of the dynamic behaviour over a large temperature range. Based on comparison of experimental and calculated behaviour qualitative hypotheses can be made on the operation of a self-pulsating CD laser diode. The deviation from the standard exponential threshold temperature dependence has been explained, and accounted for in the model. More importantly, it has been shown that the self-pulsation frequency in these lasers does not obey the standard square root rule observed for relaxation oscillations, finally dispelling the myth that self-pulsation in CD type laser structures is purely a destabilised relaxation oscillation, due to saturable absorption.

One of the drawbacks of this model however, is that while it can be used describe the gross dynamic features of self-pulsation in CD lasers, and can be easily adapted to describe electro-optic synchronisation of such a laser (chapter 6), it does not give any insight into the physics of pulse formation in CD lasers. This problem is addressed in the next chapter.

Chapter 4

Pulse Formation in CD Lasers: A Closer Look

4.1 Introduction

The general properties of self-pulsating CD lasers have been discussed in the previous two chapters. At the end of chapter 2 a simple three rate equation model was introduced which has been commonly used to study self-pulsation in these type of semiconductor laser structures. In chapter 3 this model was expanded to include temperature, and by comparing experimental data with simulation, some qualitative conclusions could be drawn on the operation of these devices. However, by the end of the chapter is was apparent that this type of description had severe limitations in terms of understanding the underlying physics in CD type lasers. The present chapter begins by re-examining more closely some of the experimental data presented in chapter 3. The insights gained when further investigating some of the peculiarities in this behaviour point in the direction of progress. Based on these fresh insights, a new hypothesis is presented at the end of the present chapter, on the origin of self-pulsation in CD lasers.

4.2 Non-Linearities in Light-Current Characteristics at Low Temperature

The experimental LI and self-pulsating characteristics for the type of CD laser which has been previously discussed in chapter 3 are re-plotted beside each other in Fig. 4.1 for comparison. Concentrating first on Fig. 4.1 (a), the LI behaviour is highly linear over the range 150 K $\leq T \leq$ 370 K. However, below 150 K, the LI curves develop significant non-linearities, which increase in severity with decreasing temperature. Moving now to Fig. 4.1 (b), self-

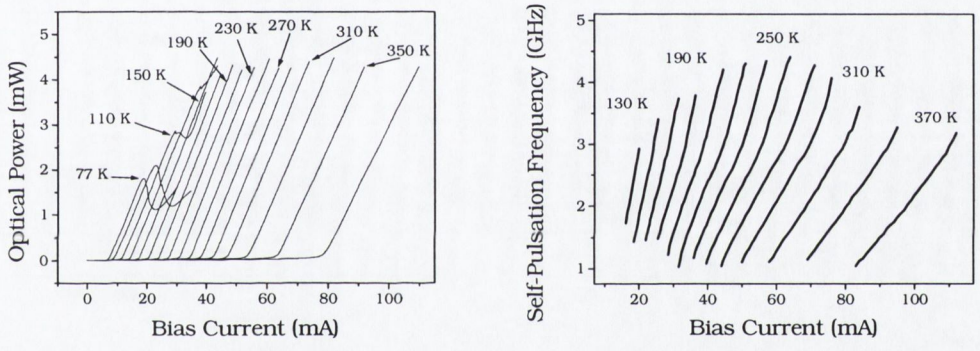

(a) (b)

Figure 4.1: (a) Typical experimental Light-Current curves for a SHARP LT022MD in the range $77\ K \leq T \leq 370\ K$ and (b) Experimental self-Pulsation frequency bias current for the same laser in the range 110 K $\leq T \leq$ 370 K.

pulsation can be seen to extinguish at around 130 K. Comparing this temperature with the temperature at which the non-linearities in the LI curves appear, it would reasonable to assume that there is some relationship between the onset of self-pulsation and the cessation of LI non-linearities. In sections 4.2.1 and 4.2.2 directly following, this relationship is explored in an attempt to gain a greater understanding of the underlying physics behind the onset of self-pulsation in these type of laser diodes.

4.2.1 Polarisation Resolved Light-Current Curves and Carrier Pinning

It is well known that in the absence of gain saturation, the carrier density in mono-section laser diodes becomes pinned at the threshold current level. Above this, any further increase in pumping current leads to the excess carriers being converted to photons by stimulated emission. It is also a straight forward calculation to show that for a slab waveguide, only two types of guided transverse modes are supported, transverse electric (TE) and transverse magnetic (TM). For TE modes, the polarization of the guided light is aligned along the plane of the active layer and for TM modes the polarization is aligned along the growth direction (i.e. the plane perpendicular to the active layer). Laser diodes tend to emit predominantly in the in the TE mode, since it has a slightly larger Γ and a slightly larger facet reflectivity than the TM mode. One useful consequence of this fact, is that it gives a very easy way to probe the carrier density behaviour in a semiconductor laser, since a crossed polarizer can be used to effectively filter out the TE mode. The remaining light will then be mainly due to spontaneous emission which is of course closely related to the carrier density.

Fig. 4.2 (a) and (b) shows the polarisation resolved LI characteristics for heatsink temperatures of 370 K and 77 K respectively. On the left axis of each graph is plotted the ordinary LI curve and on the right axis is plotted the same LI curve when recorded through a Glan-Thompson polarizer, which has been orientated at 90^0 to the polarisation of the emitted light. Considering first Fig. 4.2 (a), the polarisation resolved LI curve behaves according to an exponential growth law up to about 80 mA. Above this value, which is the threshold current level at this heatsink temperature, the carrier density pins. (Note: The carrier density is not perfectly pinned, but increases very slowly with increasing bias current. This small increase is commonly attributed to spatial hole burning.) This type of behaviour held true down to around

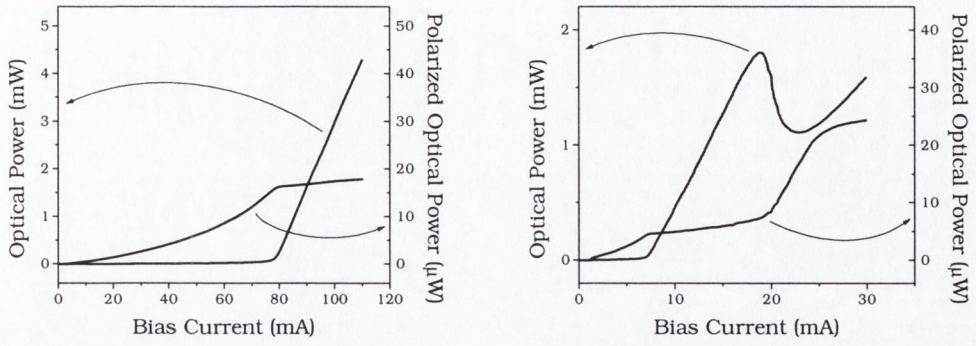

(a) (b)

Figure 4.2: (a) On the left axis, typical LI curve for a SHARP LT022MD laser diode at a heatsink temperature of 370 K, on the right axis, a typical polarisation resolved LI Curve. (b) Similar plots for the same laser, but at a heatsink temperature of 77 K.

150 K. However, in Fig. 4.2 (b), an interesting feature appears in the the polarisation resolved LI curve (on the right axis of the graph). The curve appears to pin once at the threshold level and for a second time at higher level around the non-linearity in the non-polarisation resolved LI curve.

Previously, non-linearities in the LI behaviour have been investigated both experimentally [36] and theoretically [15]. The origins of these non-linearities were attributed to spatial hole burning, arising from a change in the carrier density profile across the active region due to stimulated emission. This would lead to a change in the overall intensity distribution, and would manifest itself as distortion in the first order transverse mode. This distortion would naturally lead to a change in the efficiency of the laser and hence the non-linearity in the LI curve. Fig. 4.3 shows two key graphs extracted from [15]. The graph on the left hand side shows the non-linearities in the LI curve. The plot on the right hand side shows the asymmetry in the carrier density profile, associated with the non-linearity.

Presented in the next section are experimental investigations, which were made on the near field of this laser diode in order to ascertain whether the

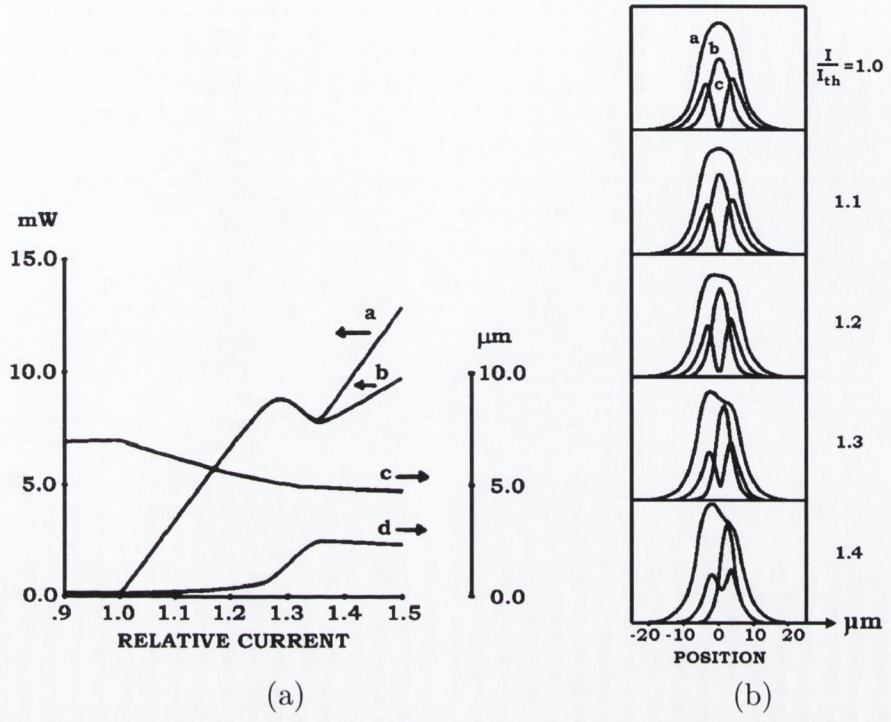

Figure 4.3: On the left: (a) Total output power, (b) output power of the fundamental mode, (c) full width at half maximum of the intensity distribution of the fundamental mode, and (d) position of maximum intensity relative to the centre. On the right: (a) Carrier density, (b) normalised intensity distribution for the first-order mode, and (c) comparable intensity distribution for the first-order mode, all shown for different values of the current. Reprinted from [15].

distortion in the near field predicted in [15] could indeed be observed under the same conditions where the non-linearities in the LI curves were found to occur.

4.2.2 Near Field Patterns

Fig. 4.4 shows the experimental setup used to investigate the behaviour of the near field over the temperature range in question. The lasers were placed in the liquid nitrogen cryostat under similar conditions as before and the emitted light was collected by a 0.65 NA microscope objective. Unlike Fig. 3.1

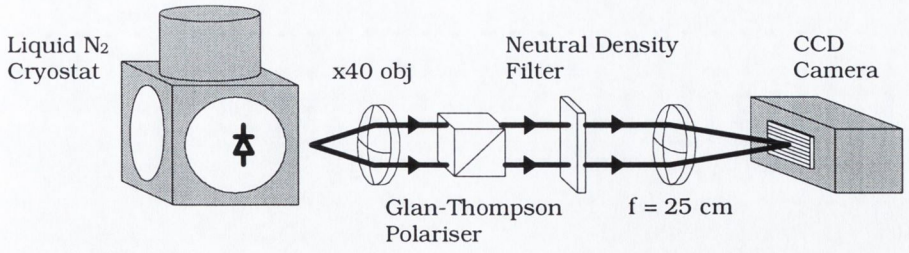

Figure 4.4: Schematic of the experimental set-up used to investigate the near field.

however, an optical isolator was not used to eliminate feedback. Instead, both the Glan-Thompson polariser and the neutral density filters were set at a very slight angle to the beam. Different polarisation states could be selected by rotating the polariser. The beam was then focused down to a spot on a CCD array by a 25 cm focal length lens. The total magnification of the system was calibrated using a pinhole array was found to be 38.5. Fig. 4.5 shows the evolution of the near field patterns for both the overall light emission and the polarisation resolved spontaneous emission component, for a heatsink temperature of 77 K. Below threshold, which was approximately 7 mA at this temperature, both near field patterns are symmetric. Once the device begins to lase, an asymmetry appears in the lasing intensity distribution, which is mirrored in the opposite asymmetry in the spontaneous emission. This asymmetry reaches a maximum under the same bias condition where the non-linearity in the LI curve occurs. This observation can be explained as follows. Small imperfections in the active layer lead to spatial hole burning of the carrier density profile. This can be seen by examination of the near field of the spontaneous emission. Since the semiconductor refractive index is linked directly to the carrier density through complex susceptibility and the plasma effect, any asymmetry in the carrier density profile leads to asymmetric guiding of the light, which can be directly observed in the near field emission.

One of the difficulties with this particular experiment is in making direct

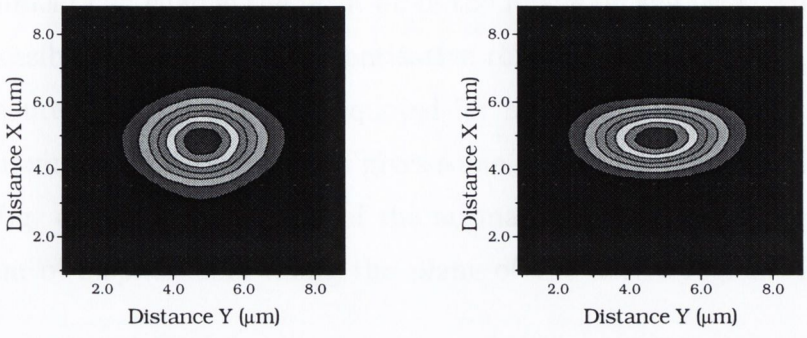

77 K, 4 mA, unpolarised

77 K, 4 mA, polarised

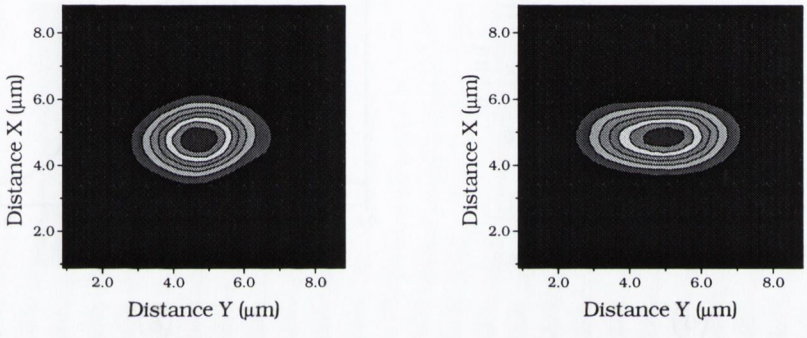

77 K, 10 mA, unpolarised

77 K, 10 mA, polarised

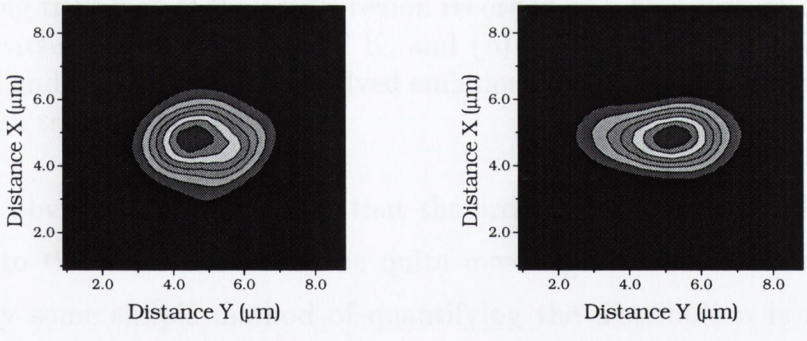

77 K, 20 mA, unpolarised

77 K, 20 mA, polarised

Figure 4.5: Six representative normalised contour plots of the time averaged near field pattern, recorded at various bias conditions, at a heatsink temperature of 77 K. The patterns on the left show the direct light emission while those on the right are recorded under similar conditions but are polarisation resolved.

quantitative displacement measurements, since small changes in temperature and alignment can change the position of the image on the CCD. However it is still possible to make useful quantitative relative distance measurements. One measurement which is often quoted for mode profiles is the full width at half maximum (FWHM), which gives some idea of the physical size of the mode. Fig. 4.6 (a) shows a plot of the normalised intensity distribution as a function of displacement along the plane of the active region. It should

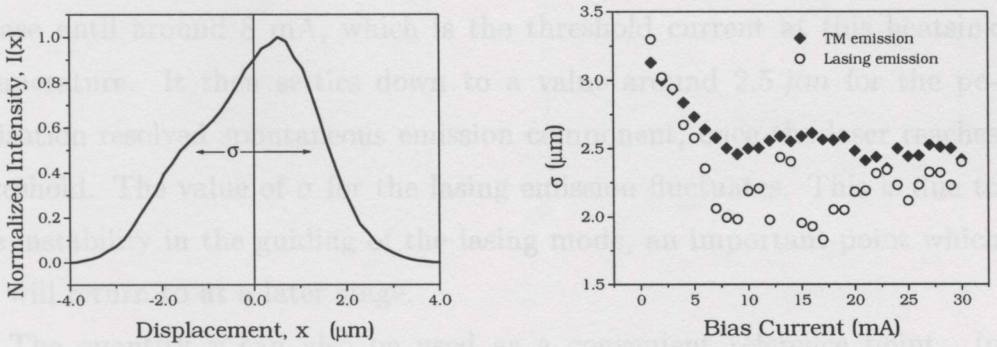

(a) (b)

Figure 4.6: (a) Normalized intensity profile of the polarisation resolved emission, along the plane of the active region recorded at a bias current of 17 mA and a heatsink temperature of 77 K, and (b) Plot of σ for both the lasing emission and the polarisation resolved emission for different bias currents, at a heatsink temperature of 77 K.

be quite obvious from this figure that the ordinary definition of FWHM as applied to this situation would be quite meaningless. To circumvent this difficultly some simple method of quantifying the distribution is required. If $I(x)$ is the intensity distribution as a function of displacement, x, as in Fig. 4.6 (a), then a quantity $\bar{x}$ can be defined, which describes a weighted centre position, in an analogous formula to the definition of centre of mass [37] in classical mechanics,

$$\bar{x} = \frac{\int xI(x)dx}{\int I(x)dx}. \tag{4.1}$$

In an analogous formula to the definition of the radius of gyration in classical mechanics, $\bar{x}$ can then be used to calculate a quantity σ which is similar to the FWHM.

$$\sigma = 2\sqrt{\frac{\int (x-\bar{x})^2 I(x)dx}{\int I(x)dx}} \tag{4.2}$$

Fig. 4.6 (b) shows a plot of σ for both the lasing emission and the spontaneous emission for different bias currents, at a heatsink temperature of 77 K. The value of σ for both lasing and spontaneous emission can be seen to decrease until around 8 mA, which is the threshold current at this heatsink temperature. It then settles down to a value around 2.5 μm for the polarisation resolved spontaneous emission component, once the laser reaches threshold. The value of σ for the lasing emission fluctuates. This is due to the instability in the guiding of the lasing mode, an important point which we will return to at a later stage.

The quantity $\bar{x}$ can also be used as a convenient reference point. In Fig. 4.6 (a), and Fig. 4.7 (a), $\bar{x}$ is assigned a value of zero. Fig. 4.7 (a) shows the evolution of the intensity profile of the polarisation resolved emission with bias current. Note that the maximum displacement of the peak intensity occurs in the current region 15 mA to 20 mA. This fact is more clearly illustrated by Fig. 4.7 (b), which shows the displacement of $\bar{x}$ from the peak intensity of the polarisation resolved TE emission, as a function of bias current. The LI characteristics for the same conditions are also plotted for comparison. It is now very clear from this graph that the maximum peak displacement occurs at the non-linearity in the LI curve and that the two are directly related. A similar result was also predicted in [15] for wide stripe lasers and explained in the following manner. For increasing currents, the position of maximum intensity starts moving further away from the centre of the gain region, due to spatial hole burning of the carrier density. The intensity profile narrows due to this changed carrier density profile and in order to maintain the mode gain, the efficiency must then decrease. Of course in an

ideal laser structure with a perfectly uniform active region this effect would not be observed since a perfectly uniform active region would introduce a degeneracy into the system. However any tiny imperfections or asymmetries, which would be observed in a real laser would remove this degeneracy and lead to non-linearities in the modal gain and consequently spatial hole burning.

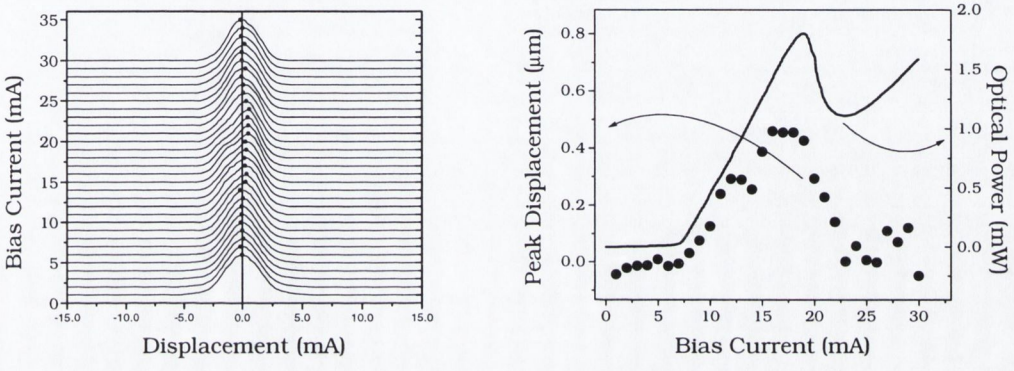

(a) (b)

Figure 4.7: (a) Intensity profiles as a function of displacement along the plane of the active region for the polarisation resolved emission, for currents, I in the range $0 \leq I \leq 30$ mA and at a heatsink temperature of 77 K. Note the peak intensity for each curve is marked by a dot. (b) On the left axis, the displacement of peak intensity of the spontaneous emission, from $\bar{x}$ in μm, against bias current for a heatsink temperature of 77 K. On the right axis, optical power plotted against bias current for the same experimental conditions.

With reference to Fig. 4.1 (a) it can be seen that as the heatsink temperature is raised, the kinks in the LI curve appear at increasing optical powers and decrease in magnitude. By the time the heatsink temperature has reached 150 K the kinks have disappeared altogether and the LI curve becomes highly linear. This was also the temperature at which the device first began to exhibit well defined self-pulsation. Once the laser begins to operate in this self-pulsation regime the behaviour of the near field changes markedly. Fig. 4.8 shows contour plots of the near field patterns for three

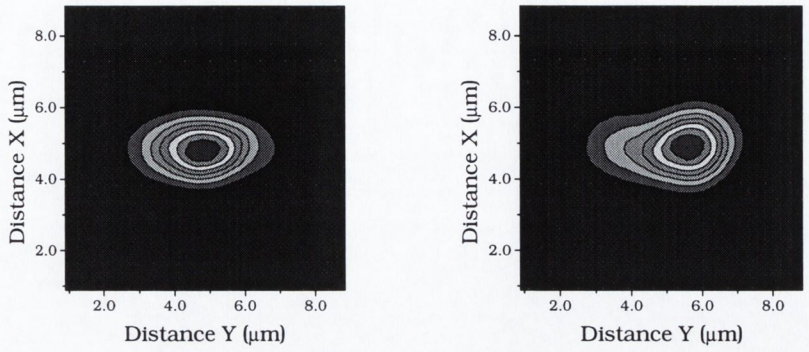

150 K, 44 mA, unpolarised

150 K, 44 mA, polarised

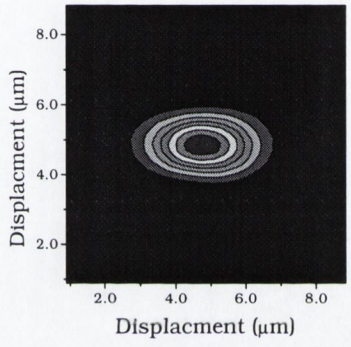

230 K, 56 mA, unpolarised

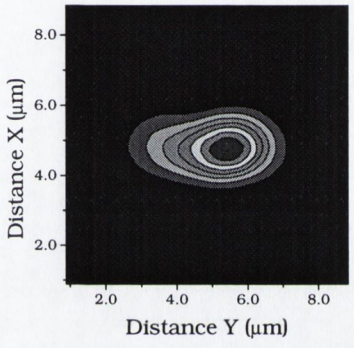

230 K, 56 mA, polarised

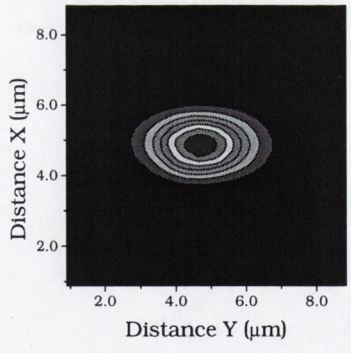

310 K, 74 mA, unpolarised

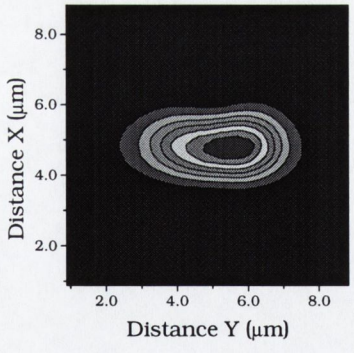

310 K, 74 mA, polarised

Figure 4.8: Six representative normalised contour plots of the near field pattern, bias conditions which correspond to an optical power of about 4 mW, and at heatsink temperatures of 150 K, 230 K and 310 K. The patterns on the left show the direct light emission while those on the right are recorded under similar conditions but are polarisation resolved.

representative heatsink temperatures when the laser is in the self-pulsating regime. Comparing this with the last two contour plots of Fig. 4.5, it becomes apparent that the behaviour of the near field patterns is quite different. In this case the near field pattern of the lasing emission was asymmetric in a way which complemented the asymmetry in the spontaneous emission. However, in Fig. 4.8 all the lasing near field patterns are highly symmetric while the spontaneous emission near field patterns are highly asymmetric.

Fig. 4.9 shows (on the left) the variation in the displacement of the peak intensity, x_0, from $\bar{x}$ with bias current, and (on the right) the variation of σ with bias current, for three representative temperatures. For temperatures above 150 K, displacement of the peak intensity from $\bar{x}$ is spread around zero indicating the symmetry of the near field pattern for all bias currents in the self-pulsating regime. In contrast, the displacement of the peak intensity from $\bar{x}$ is spread around zero until threshold and then increases more or less monotonically with increasing bias current. The variation of σ with bias current is similar for both stimulated and spontaneous emission, settling down to around $2\mu m$ for the former, and a slightly larger value for the latter, once the threshold current is reached. These results are very interesting, since at first glance, they appear to contradict the previous explanation for both of the asymmetric lasing and polarisation resolved spontaneous emission near field patterns. The key to understanding this effect is to recognise that these near field patterns are now highly time averaged, since the laser is self-pulsating in the GHz regime. Typically, the duty cycle of these laser diodes is about 10% when it is exhibiting self-pulsation. Thus the laser spends much more time *off* rather then *on*. Notwithstanding this, the stimulated emission still swamps the spontaneous emission and it must be assumed that the near field pattern is on average symmetric during pulse emission. However, when polarisation resolved, the lasing component is effectively removed. The light which is observed is then much more representative of the time averaged near field pattern when the laser is in the other 90% of its duty cycle. This result

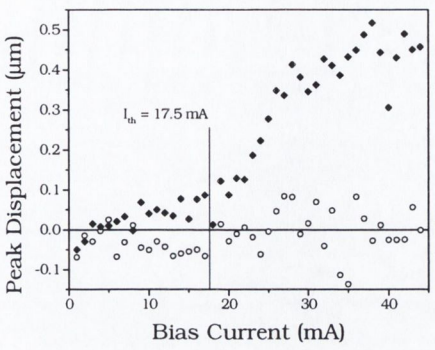

(a) $(\bar{x} - x_0)$ vs I, 150 K

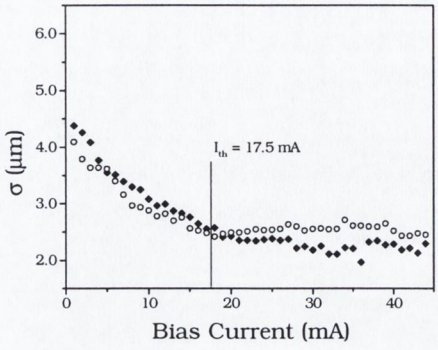

(b) σ vs I, 150 K

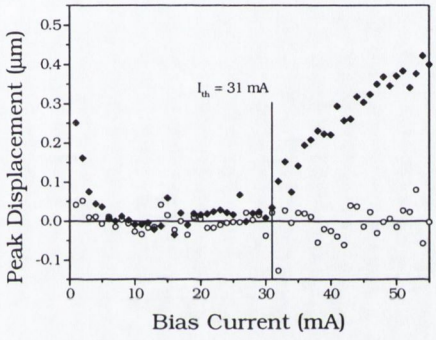

(c) $(\bar{x} - x_0)$ vs I, 230 K

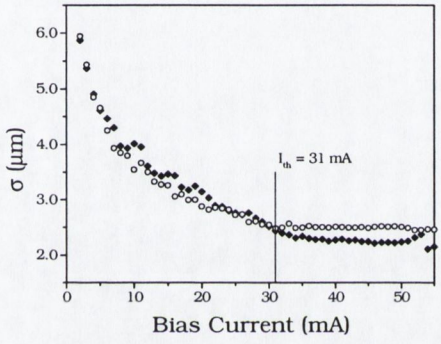

(d) σ vs I, 230 K

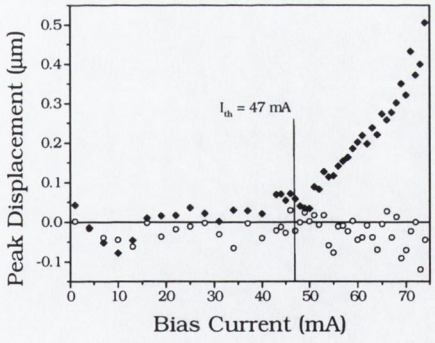

(e) $(\bar{x} - x_0)$ vs I, 310 K

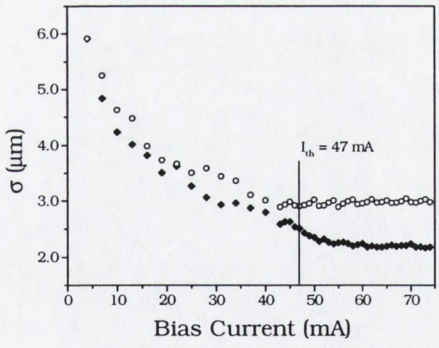

(f) σ vs I, 310 K

Figure 4.9: Six representative graphs which show the variation of both $(\bar{x} - x_0)$ and σ with bias current for heatsink temperatures of 150 K, 230 K and 310 K. The black diamonds represent the spontaneous emission, while the white circles represent the stimulated emission.

furnishes direct evidence for spatial modification of the the light emission and hence the carrier density during the self-pulsation cycle.

4.3 Dynamic Spatial Modifications During Pulse Emission

4.3.1 Experimental Techniques: The Streak Camera

In order to further investigate the carrier density changes during pulse formation and emission, a streak camera was used to investigate the dynamic behaviour of the laser diode. The following paragraph describing the operation of a streak camera has been condensed from the Hamamatsu streak camera application note. In simple terms, the streak camera converts incident light into electrons and performs a high-speed sweep (deflecting electrons from top to bottom), enabling detection of the time variation of the incident light intensity by converting these into different positions on the screen. Fig. 4.10 shows the operating principle of the streak tube, which forms the heart of the streak camera. The light pulse to be measured is focused onto the photo-

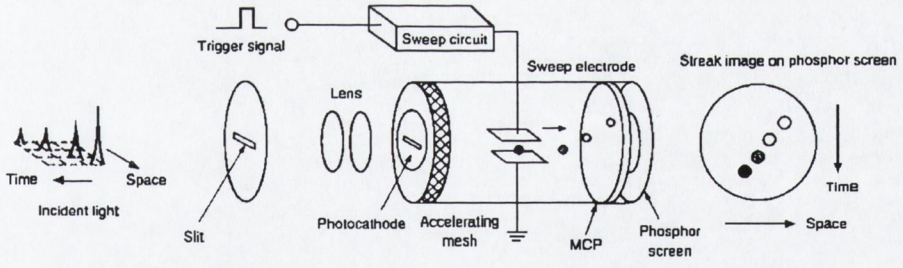

Figure 4.10: Illustration showing the operation of a streak camera. Reprinted from the Hamamatsu catalogue.

cathode of the streak tube through the slit, where the photons are converted into a number of electrons proportional to the intensity of the incident light. These electrons are accelerated and directed towards the phosphor screen, and a high-speed voltage is applied which is synchronized to the incident

light. The electrons are swept at high speed from top to bottom and are then multiplied in the MCP (micro-channel plate), after which they collide against the phosphor screen of the streak tube and converted to an optical image. The optical image which appears on the phosphor screen is called a streak image, and shows the intensity distribution of the incident light, by which the positions of the electrons can be determined in the perpendicular direction over the passage of time. Using this method, the temporal intensity distribution of the light being measured can be displayed as the spatial intensity distribution on the phosphor screen.

Fig. 4.11 shows the experimental setup used to measure the spatial and temporal evolution of the near field. The emitted light was collected and collimated using a microscope objective. The centre of the beam waist was then imaged onto the input slit of the streak camera. The streak camera was run in single shot mode which meant that the measurement was non-invasive (i.e. it was not necessary to use a trigger signal which might perturb the self-pulsation).

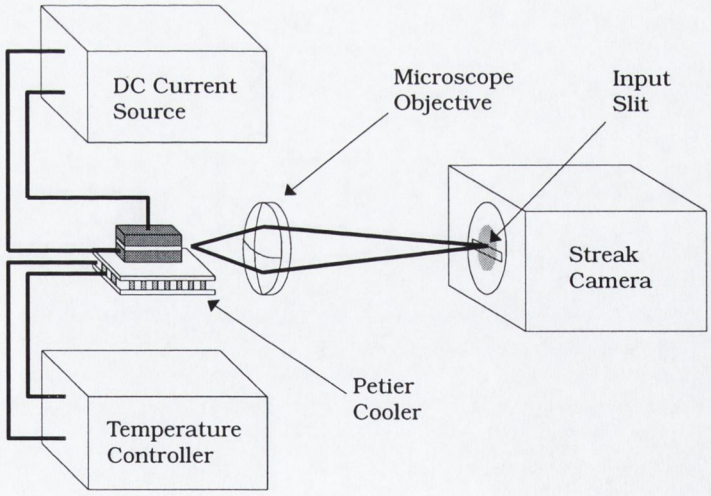

Figure 4.11: Schematic of the experimental set-up used to measure the spatial and temporal evolution of the near field.

4.3.2 Experimental Results

Fig. 4.12 shows a plot of the temporal evolution of the optical power for a typical SHARP LT022MD laser diode under self-pulsating conditions. The plot shows four pulses which were caught in a 4 ns single shot. The time delay between each pulse is slightly longer than 1 ns, indicating a self-pulsation frequency just below 1 GHz. This plot also shows that the rise time of the pulses is somewhat shorter than the fall time. As a sanity check, the

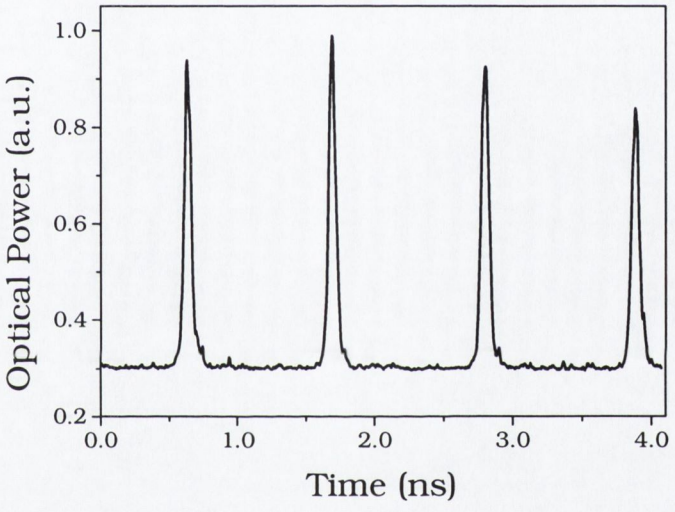

Figure 4.12: Plot of the optical power emission as a function of time for a typical SHARP LT022MD laser diode. The bias current was 46 mA and the laser was at ambient temperature.

pulsewidth measurements made using the streak camera can be compared with pulsewidth measurements made using the autocorrelator. This is shown Fig. 4.13. It is clear from this plot that both measurements are in good agreement.

Fig. 4.14 is a contour plot showing the spatial evolution of the near field in the plane parallel to the active region. The streak camera was also run in single shot mode for this measurement and thus the signal to noise ratio

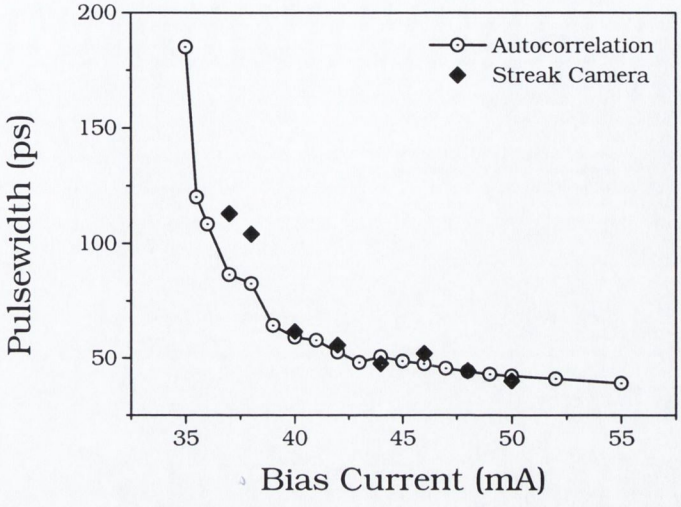

Figure 4.13: Plot showing the pulsewidth versus bias current. The hollow circles were measured using the autocorrelator and the black diamonds were measured using the streak camera.

is not very good. However it is still possible to discern some overlying trend describing the pulse evolution. It is clear that at the onset of lasing the waist of the near field is spatially quite broad. As time progresses the waist of the near field begins to narrow to a well defined point. The lasing emission is then extinguished.

Using Eq. 4.2 it is possible to extract the change in the standard deviation of the intensity distribution of the near field waist, σ_W, with time. This is shown in Fig. 4.15. The evolution of the optical pulse is also shown on the time axis for comparison. This result is very interesting because it shows that there is indeed considerable spatial modification of intensity distribution during pulse emission. This is indicative of a phenomenon known as self-focusing [14].

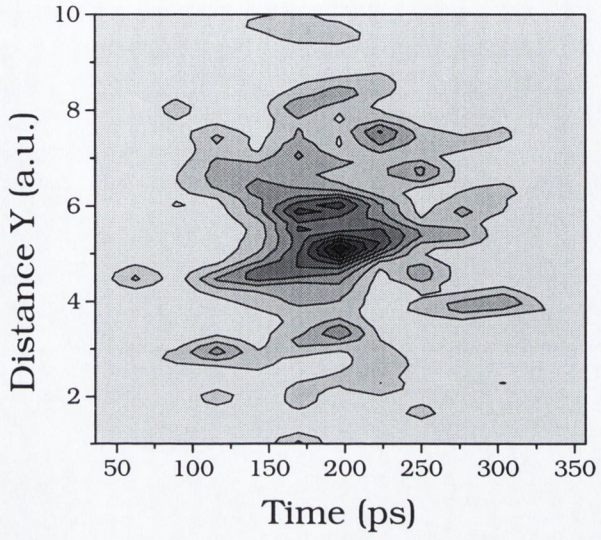

Figure 4.14: Plot showing the evolution of the near field along the plane of the active region for a typical SHARP LT022MD laser diode. The bias current was 45 mA and the laser was at ambient temperature

4.4 Describing the Formation Pulses with both Spatial and Temporal Information

4.4.1 Limits of a 1D Rate Equation Model

Single mode rate equations have been introduced in chapters 2 and 3, in order to describe self-pulsation in CD type laser structures. This type of model will hence forth be referred to as '1D', because the resulting output involves only temporal information regarding the emitted light. This model is certainly useful since from a computational point of view it is relatively simple and quick to implement. It is also quite sufficient to model many applications which require only macroscopic details about self-pulsation in CD type laser structures, as demonstrated in chapter 6. However, in terms of understanding the underlying physics behind self-pulsation in CD lasers,

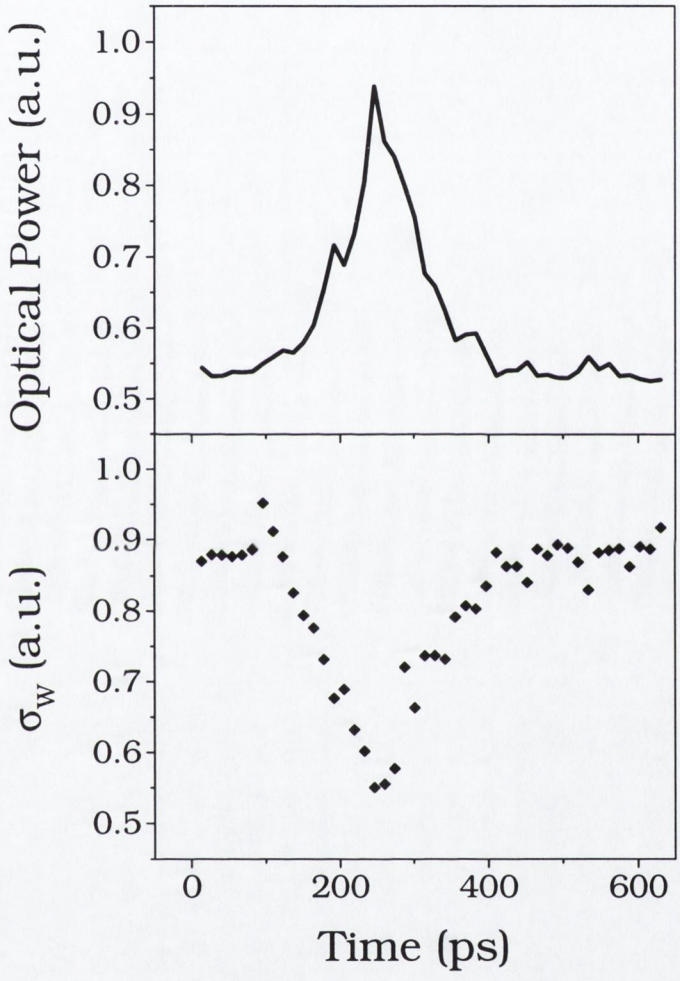

Figure 4.15: Plot showing the evolution of σ_W as with time.

this model is quite limited. In order to get a more complete understanding of self-pulsation in this kind of laser structure it is necessary to move onto the type of model which will be referred to as '2D'. With this model information can be gathered about spatial distributions of the carrier density and the emitted light in one dimension as well as the temporal information.

4.4.2 A 2D Self-Pulsating CD Laser Model

The model which is described below was implemented by McEvoy and is discussed at length in his thesis [38]. It is based on the original work of Takayama *et al.* [39, 40]. The single mode rate equations (2.38)-(2.40) are modified to include spatial information in the lateral direction. This was achieved by dividing the active region into a number of lateral sections (in this case 90), of width $\Delta y = 0.2$ μm.

$$\frac{dN_i}{dt} = \frac{I_i}{ed} - \gamma(N_i)N_i - \Gamma_i G(N_i)P + \frac{D[N_{i-1} - 2N_i + N_{i+1}]}{(\Delta y)^2} \tag{4.3}$$

$$\frac{dP}{dt} = \left(\sum_{i=1}^{90} \Gamma_i G(N_i) - \frac{1}{\tau_p}\right) P + \sum_{i=1}^{90} R_{sp}(N_i) \tag{4.4}$$

Here d is the thickness of the active region, and the other parameters have previously been defined elsewhere (See pages 52-57 of chapter 3). The effects of the various epitaxial layers (shown schematically in Fig. 4.16), on the guiding properties of the laser are incorporated through the calculation of the individual Γ_i for each lateral section. This is achieved in the following manner: the electric field is divided into perpendicular and parallel components in the transverse plane, $\psi(x, y)$ and $\phi(y)$ respectively.

$$E(x, y) = \psi(x, y)\phi(y) = \psi_{i,j}\phi_j \tag{4.5}$$

$\psi(x, y)$ is calculated by solving the field equation (4.6), using the appropriate boundary conditions.

$$\frac{\partial^2 \psi(x, y)}{\partial x^2} + \left[n^2(x, y)k_0^2 - \beta^2(y)\right] \psi(x, y) = 0 \tag{4.6}$$

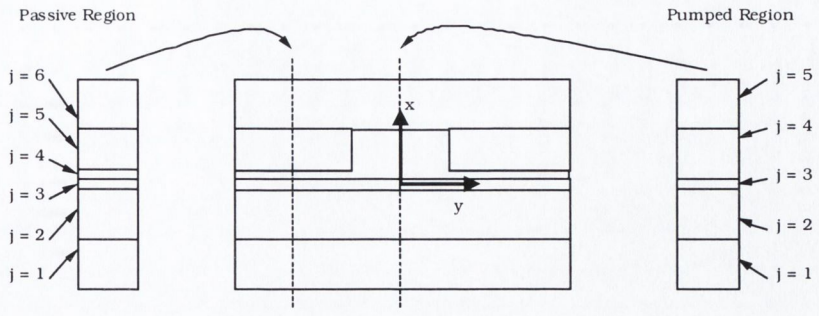

Figure 4.16: Schematic diagram showing an idealised transverse cross-section of the laser.

Here $n(x, y)$ is the layer dependent complex refractive index, and $\beta(y)$ is the complex propagation constant in the direction perpendicular to the junction plane at y. k_0 is the wave number in free space. Since the laser structure has been converted into sections this equation is transformed to,

$$\frac{\partial^2 \psi_{i,j}}{\partial x^2} + \left[n_{i,j}^2 k_0^2 - \beta_i^2\right] \psi_{i,j} = 0 \tag{4.7}$$

where j denotes the layers comprising the laser structure as shown in Fig. 4.16. In a similar fashion the optical field function in the lateral direction can be computed by solving (4.8).

$$\frac{\partial^2 \phi_i}{\partial y^2} + \left[n_{eff}^2(x) k_0^2 - \beta_z^2\right] \phi_i = 0 \tag{4.8}$$

$n_{eff}(x)$ is the effective refractive index which is given by $n_{eff}(x) = \beta_i / k_0$, from the previous result. Finally the Γ_i can be calculated using Eq. (4.9).

$$\Gamma_i = \frac{\int_{y_{i-1}}^{y_i} \phi_i \phi_i^* dy}{\sum_i \left(\int_{y_{i-1}}^{y_i} \phi_i \phi_i^* dy\right)} \frac{\int_{x_{i,2}}^{x_{i,3}} \psi_{i,3} \psi_{i,3}^* dy}{\sum_j \left(\int_{x_{i,2}}^{x_{i,3}} \psi_{i,j} \psi_{i,j}^* dy\right)} \tag{4.9}$$

4.4.3 Calculated Results

Fig. 4.17 shows the calculated evolution of the light distribution in the lateral direction on a contour plot. This plot shows good qualitative agreement with the experimental streak camera trace in Fig. 4.12. At the onset of the

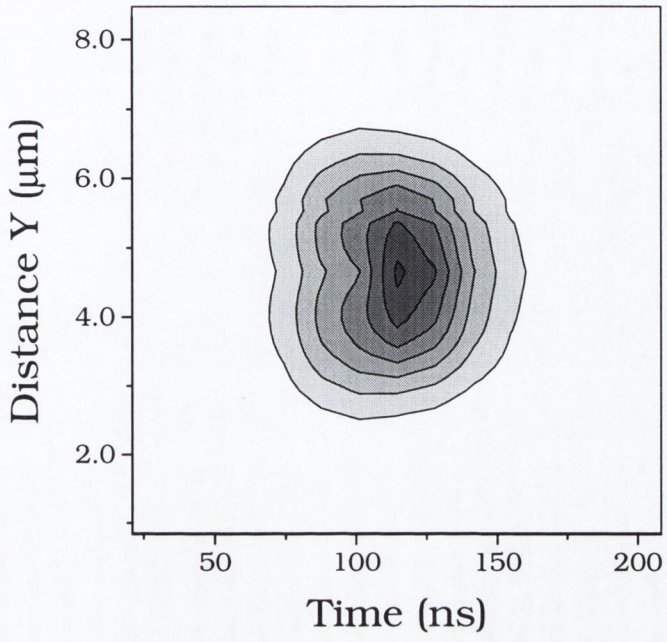

Figure 4.17: Calculated contour plot showing the spatial and temporal evolution of the optical pulse. The pulse was simulated at a temperature of 300 K and a bias current of 60 mA.

pulse the light distribution is spatially quite broad, with two lobes. The light distribution then rapidly narrows until the pulse reaches its maximum intensity. This behaviour can be seen more clearly in Fig. 4.18. This figure shows a series of five time slices 20 ps apart which display the calculated spatial distribution of four quantities along the lateral direction during the formation of a light pulse. The first of these quantities is the carrier density which can be seen to decrease in magnitude as carriers are converted into photons. The second of these quantities is the gain which naturally follows the carrier density. The third quantity is the effective refractive index. The magnitude of the effective refractive index results from a combination of the in built refractive index profile due the various epitaxial layers, and an additional component which results from the spatial distribution of the carrier density.

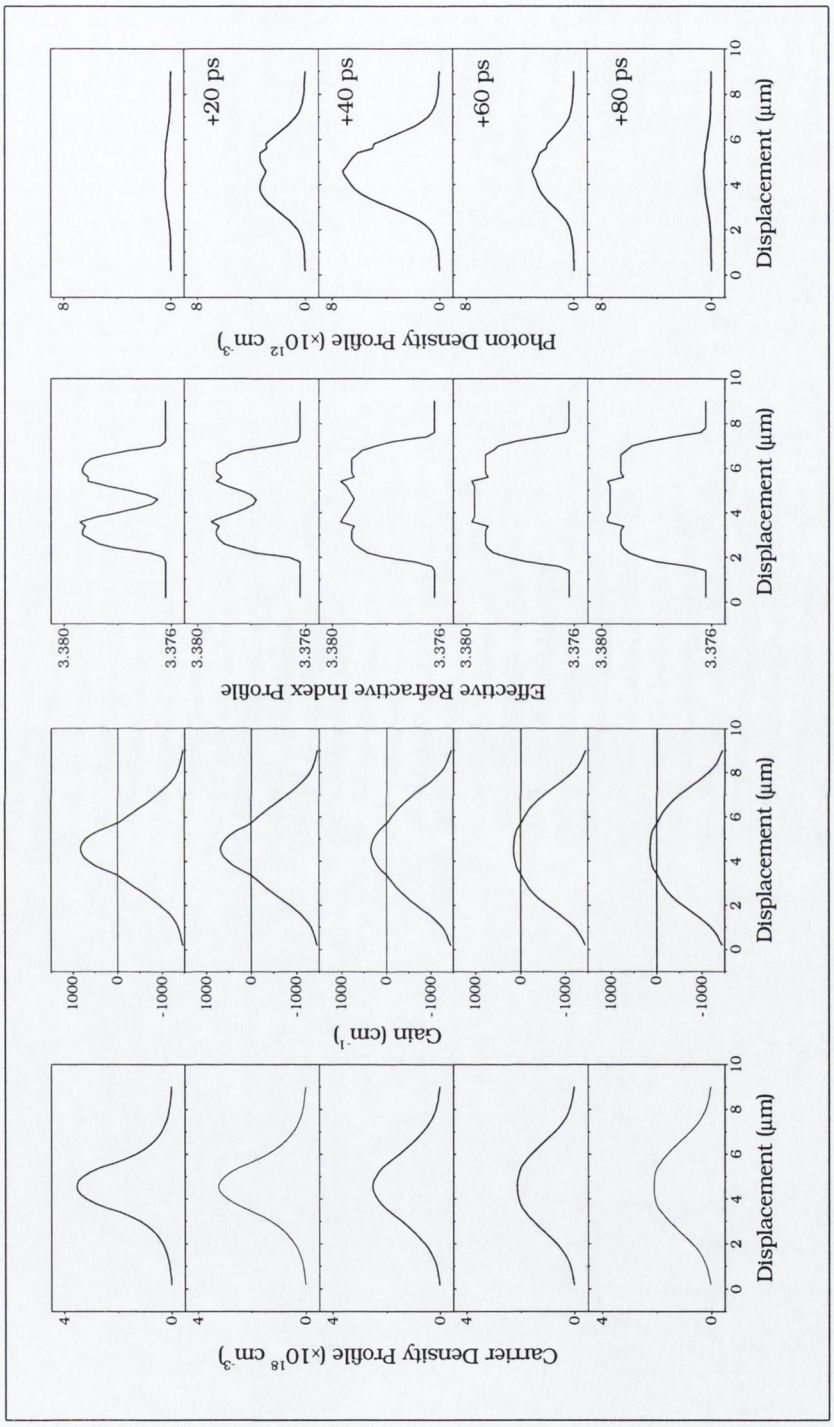

Figure 4.18: Calculated temporal evolution of the carrier density, gain, net effective refractive index, and photon density. The time slices are 20 ps apart, and the bias current was 60 mA.

At the beginning of the light pulse, the effective refractive index profile has a very well defined hole in the centre, which is due to the large value of the carrier density at this time. It is this hole burning of the effective refractive index which determines optical distribution, which is broad with a dip in the centre, and can be seen in the fourth column of this figure. With increasing time, the carrier density evolution, and hence the effective refractive index serves to further encourage the strength of the guiding, and the spatial width of the pulse narrows. Eventually the carrier density becomes sufficiently depleted that there is not enough gain to overcome the losses within the laser and stimulated emission is extinguished.

Fig. 4.19 shows the calculated change in the standard deviation of the intensity distribution, σ_W, along the plane of the active region with time. The evolution of the optical pulse is also shown. It was necessary to introduce a small level of noise (30 dB down from the peak maximum) in order to prevent a zero in the numerator of Eq. (4.2). The calculted σ_W, shows the same trend as the experimentally measured σ_W, shown in Fig. 4.15, and the characteristic signature of self-focusing.

Based on the experiment and calculation it is now possible to propose a mechanism for the origin of self-pulsation in these type of laser structures.

4.5 A Possible Mechanism For the Formation of Pulses in CD Lasers

On the strength of the evidence presented in sections 4.2, 4.3, and 4.4 it should be clear that any explanation of self-pulsation based only on a simple '1D' rate equation model with saturable absorption is incomplete. Moreover, clear evidence has been presented which shows that there is significant spatial dynamics during the formation of a light pulse. On the basis of these findings, a hypothesis can now be formed on the true origin of self-pulsation

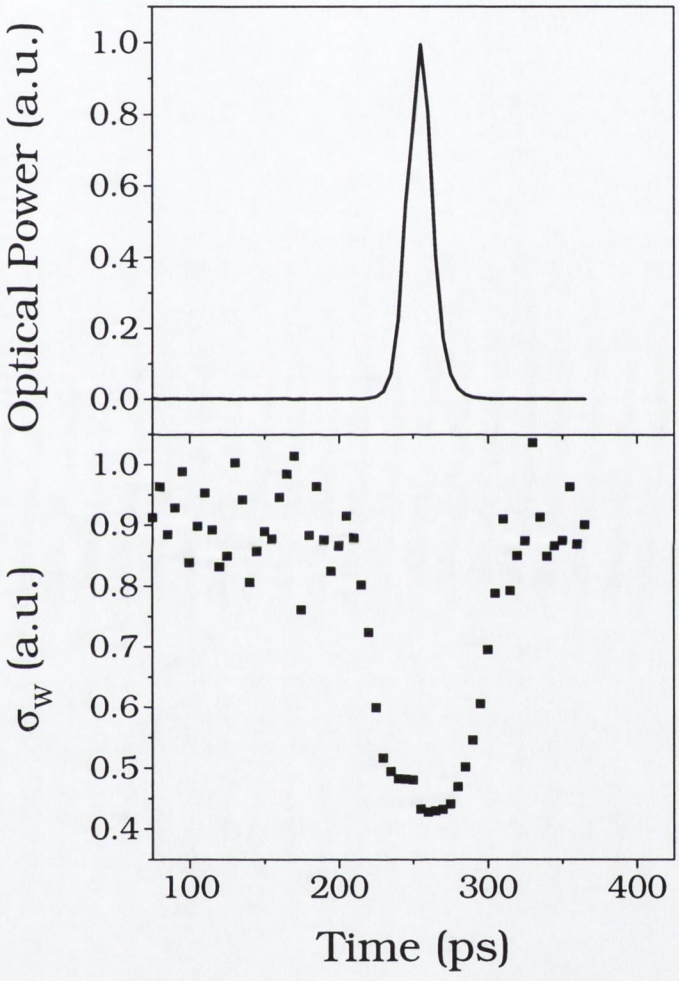

Figure 4.19: Plot showing the calculated evolution of σ_W as with time.

in CD type laser structures. The reader is first referred back to the CD laser structure in Fig. 3.1. The active region is pumped through a p-type electrical contact and the current is confined to the centre by two n-type blocking layers either side of the central region. These blocking layers create an effective refractive index profile in the lateral direction with a step which aids guiding in the centre region. However, once current is injected into the laser the large concentration of carriers towards the centre tends to oppose this guiding by setting up an anti-guiding refractive index profile. Due to this anti-guiding effect, the gain must be large to overcome the losses. Once the lasing condition is reached, carriers rapidly recombine to create stimulated emission photons. As the carrier density decreases the inherent effective index guiding of the blocking layers begins to dominate and less gain is required to overcome the losses in the cavity. Eventually the population inversion becomes depleted and the device can no longer sustain lasing. The number of carriers must then recover before the conditions necessary for lasing are achieved again. This cycle is illustrated in Fig. 4.20. The first column shows the temporal evolution of the number of carriers in the active region. Four temporal positions are highlighted. The second column shows the summation of the lateral effective step index profile due to the blocking layers and the time varying lateral anti-guiding index profile due to number of carriers in the active region. The third column shows the expected near field pattern under these conditions. At position 1, the number of carriers has already built up to a maximum and the device has started to lase. The expected near field would be quite broad at this stage because the anti-guiding effect is at a maximum. At position 2, some of the carriers have already recombined so that the anti-guiding effect is diminished and the optical mode shows enhanced guiding. At position 3, the optical intensity reaches a maximum, and the anti-guiding effect is at a minimum. At position 4, the lasing emission has already been extinguished and the number of carriers has begun to recover. The cycle then repeats.

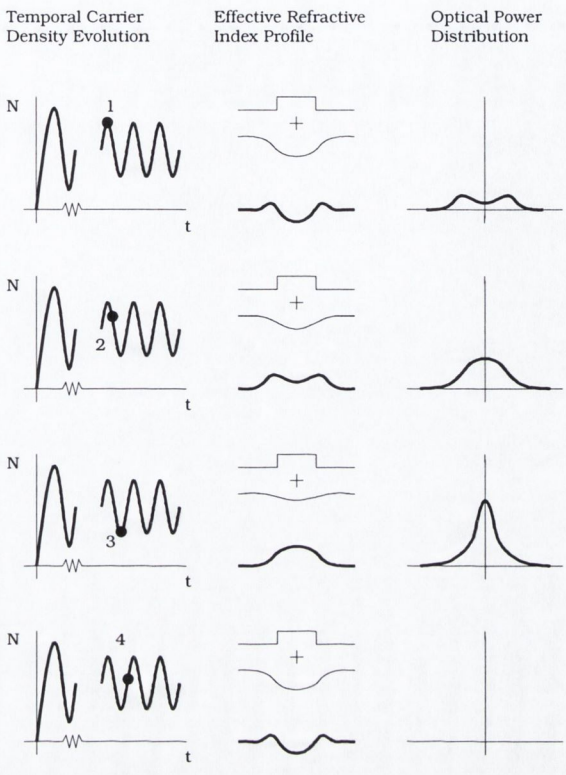

Figure 4.20: Illustration showing the temporal evolution of the number of carriers and the corresponding lateral effective index guiding/anti-guiding effect.

4.6 Summary

The culmination of this chapter is section 4.5 where a new mechanism has been proposed to describe the origin of self-pulsation in CD lasers. Substantial evidence has been presented to support this mechanism. In section 4.2 two main results stand out. At low temperatures, when the laser is emitting in the CW regime, it has been shown that an instability in the guiding results in changes in the emitted power level. At higher temperatures, when the laser is self-pulsating, symmetric and asymmetric near field patterns, lead to the conclusion that there is a modification of the carrier density profile during the pulsation cycle. In section 4.3 streak camera results are presented in which this spatial modification of the optical emission can be directly observed. Fi-

nally in section 4.4 it has been shown how a model can be developed, which supports the interpretation of the experimental results. However, the key result of this chapter, is that based on this new model, it should now be possible to design laser structures in different semiconductor materials by tailoring the refractive index profile in the gain region to exploit the same phenomena which cause self-pulsation in CD lasers.

Chapter 5

Self-Pulsation in Wider Bandgap Materials

5.1 Rationale behind the Move to Shorter Wavelengths

Compact discs have become one of the cheapest, reliable, and convenient ways to distribute digital information. A single sided CD now stores 650 Mbytes of information, corresponding to a data density of 1 bit/$(\mu m)^2$, [41]. In the last few years, however, increasing storage capacities in other media and processing power have led to a software explosion, with many of today's computer applications easily filling an entire CD. It is anticipated that higher capacity optical data storage systems will eventually replace the CD. One of the main short term goals for optical storage is to upgrade the traditional analogue video cassette recorder to a digital system based on optical discs. Such an application would require a disc capacity of about 10 Gbytes. The latest attempt is the Digital Video Disc (DVD), also known as the Digital Versatile Disc, which has a storage capacity of 4.7 Gbytes. This relative increase in data density, for a disc of similar dimensions, has been achieved by changing two things. The focused spot produced by an objective lens has a size limitation because of diffraction and is limited by $\lambda/2(\mathrm{NA})$, where λ is the wavelength of the light and NA is the numerical aperture of the lens.

This equation follows directly from the Rayleigh Criterion, Eq. 5.1, where D the aperture diameter, and $\Delta\theta$ is the minimum resolvable angular separation, [42].

$$\Delta\theta = \frac{1.22\lambda}{D} \tag{5.1}$$

Conventional CD players use an infrared laser with $\lambda = 780$ nm. DVD players use a shorter wavelength semiconductor laser with $\lambda = 650$ nm. Secondly, the NA of the lens is given by Eq. 5.2, where n is the refractive index of the medium and θ_{max} is the outer angle of the cone formed by the converging beam of light.

$$\text{NA} = n \sin\theta_{max} \tag{5.2}$$

Because of Snell's law of refraction, which says that $n \sin\theta$ is a constant, the numerical aperture does not change at the transition from air to the plastic substrate of the disc (assuming the disc substrates are made from the same material). In CD players the NA of the focusing lens is typically in the range 0.4-0.52 while in the DVD player this has been increased to about 0.6.

While the engineering aspects of realising a smaller laser spot size have been mostly addressed, there are still a number of outstanding issues which are proving to be difficult to solve, if a reading head similar to what is used in the CD player is to become practical. Firstly, the laser diode used must have a low relative intensity noise (RIN). Previously this has been achieved by using a self-pulsating laser. Pulsing a laser diode causes the optical spectrum to broaden, thereby reducing the coherence length and making the laser insensitive to the chaotic intensity fluctuations which can arise from optical feedback. It is these intensity fluctuations which would be the main deleterious factor affecting the RIN. Self-pulsating lasers which exhibit robust self-pulsation over the temperature range required for data storage applications have proved difficult to realise and DVD manufacturers have had to resort to including a radio frequency (RF) circuit to actively modulate the

laser. This RF circuit is relatively costly to make and raises additional issues regarding high frequency interference and electromagnetic shielding. Secondly, the laser diodes must have a low threshold current ($I_{th} < 50$ mA) in order to reduce power consumption and to limit the detrimental temperature effects of Joule heating. This is also proving difficult to realise, for the reasons outlined in the next section.

The beginning of this chapter deals with the details of realising a practical self-pulsating DVD laser. Section 5.2 describes the progress which has already made in fabricating red self-pulsating lasers. Section describes the experimental characterisation of a number of red self-pulsating laser diode samples, included LI behaviour, self-pulsation frequency behaviour and near-field behaviour over a wide range of operating conditions. The chapter ends with a discussion on how low threshold self-pulsating lasers might be achieved.

5.2 Realising a Practical Self-Pulsating Laser for DVD Data Storage Applications

A laser diode, if it is to be used in a viable commercial system for DVD data storage applications, must satisfy a number of criteria.

1. Wavelength, $\lambda \leq 650$ nm.
2. Low Threshold, $I_{th} \leq 50$ mA.
3. High characteristic temperature, T_0.
4. Self-Pulsation over the temperature range 0-100 ^{0}C.

The first criterion more or less dictates that the material system will be AlGaInP, although InGaAsP and InGaAlP alloys have also been used. The next two criteria are inextricably linked and are far from trivial to realise. Visible laser diodes are only a recent development. The first demonstration

of a visible CW laser, operating at room temperature was in 1985 by three groups, [43, 44, 45]. The high intrinsic thermal resistance of AlGaInP was overcome by optimising the layer structure in their lasers, thus realising CW room temperature operation. However, the lasers suffered from very high threshold currents which were very sensitive to temperature. Many attempts have been made to circumvent this problem. In 1987 a number of groups incorporated quantum well structures in the active regions of their laser diodes. The aim of this exercise was to reduce the threshold current density mainly through volume effects, and through the reduced density of states, [46, 47, 48]. Unfortunately, the increase in threshold gain was offset by the smaller confinement compared to bulk active regions, and lead to comparable threshold current densities, J_{th}. Considerable progress was made in 1991 by using a strained single quantum well active region (SSQW) in [49]. Kuo *et al.* had predicted in 1985 that introducing strain-effects in III-V semiconductors could reduce the density of states in the valance band by as much as two, thus considerably reducing the carrier density required to reach the threshold gain [50]. This group achieved threshold current densities, J_{th}, in the region of 215-300 A/cm^2 for the SSQW, compared to J_{th} in the range 545-670 A/cm^2 for a lattice-matched single quantum well (SQW). However, strain affects have the additional effect of changing the band gap, depending on whether the strain is compressive or tensile, causing the lasing wavelength to be shifted to $\lambda = 705$ nm for the SSQW laser, in this particular case. Serreze *et al.* [51] succeeded in using compressive strain in a GaInP/AlGaInP broad stripe device to realise a high-power, very low threshold laser diode, emitting at $\lambda = 665$ nm. Following this, Katsuyama *et al* [52] used a compressively strained MQW active region in the same material system to achieve low threshold current operation and exhibit high temperature lasing, up to 150 ^{0}C. Their best device (160 μm long) had a threshold current of just 13.9 mA and a lasing wavelength of $\lambda = 702$ nm at 25 ^{0}C. In 1993 Mannoh *et al.* succeeded in realising high power and high temperature operation us-

ing a MQW active region with tensile strain which emitted at $\lambda = 690$ nm. Typical threshold currents for their 350 μm devices were around 20 mA. As recent as 1998 Chang *et al.* produced an AlGaInP laser diode emitting at $\lambda = 642$ nm with a compressively strained MQW active region [53]. They also used a triple tensile strained barrier cladding layer in order to improve the confinement in their structure and produced an 800 μm gain guided laser diode with a threshold current of 48 mA.

Considering the historical development of visible laser diodes, it is clear that even producing a red laser which exhibits CW emission at room temperature is far from simple. Producing, a red laser which satisfies the first three criteria *and* self-pulsates, has proved extraordinarily difficult. One of the first successful attempts at a visible self-pulsating laser reported in the literature was by Adachi *et al.* [54]. The authors employed a trick which had been previously been reported for the AlGaAs system in order to enhance self-pulsation, [55]. This involved the incorporation of an extra layer functioning as a saturable absorber just above the active region. In this case the authors fabricated a MQW active region containing three strained 50 Å GaInP quantum wells separated by 50 Å $Al_xGa_{1-x}InP$ ($x = 0.5$) barriers, and a highly doped ($P = 2 \times 10^{18}$ cm^{-3}) 50 Å GaInP saturable absorbing layer. The saturable absorbing layer was separated from the active region by a p-type ($P = 4 \times 10^{17}$ cm^{-3}) $Al_xGa_{1-x}InP$ ($x = 0.7$) spacing layer. A schematic cross section of the laser diode, along with a band diagram is shown in Fig. 5.1. The threshold current at 20 ^{0}C was 65 mA and the operating current at an output power of 5 mA was 83 mA. The lasing wavelength, λ, was 656 nm. The laser exhibited self-pulsation up to an output power of 10 mW and the RIN was measured to be below -138 dB/Hz in the temperature range 20-50 ^{0}C. A few months later, the same group reported an improved structure which exhibited self-pulsation and the associated low RIN up to 60 ^{0}C, but at the expense of a slightly higher threshold current (75 mA at 20 ^{0}C), [56, 57]. In January of 1996 TOSHIBA published a

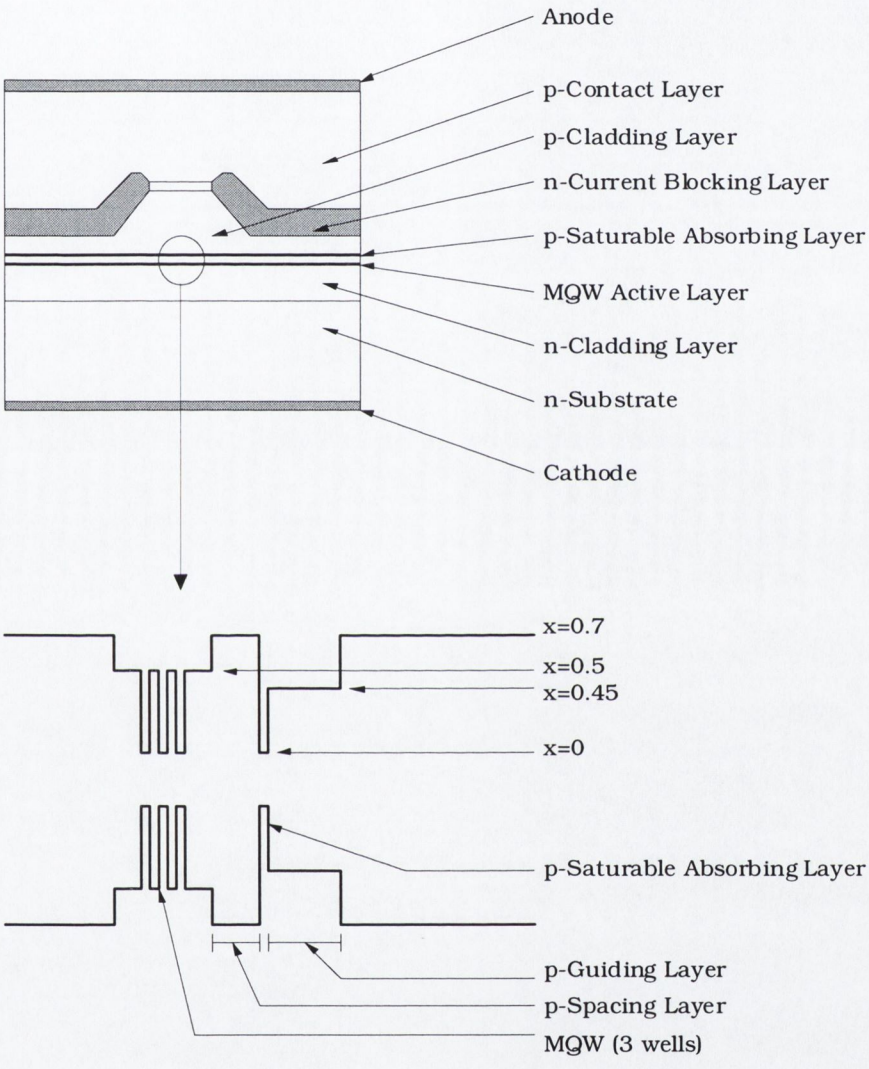

Figure 5.1: Schematic cross section and band diagram of the visible self-pulsating laser diode in [54]. The active layer consists of three quantum wells. The saturable absorbing layer consists of a single quantum well.

press release which announced that they had developed the first self-pulsating Laser diode, the TOLD9450MC, for DVD applications. However, once again the device suffered from a high threshold current ($I_{th} \sim 80$ mA at 20 ^{0}C) and only exhibited self-pulsation up to a maximum temperature of 60 ^{0}C. Soon after SHARP followed suit with the their LT055PS. It suffered from similar problems. Subsequently, Summers and Rees [58] published a numerical study of the thermal limitations of self-pulsation in the type of laser fabricated by Adachi. They concluded that the self-pulsation would be limited to a maximum temperature of 60 ^{0}C. Their reasoning was that the epitaxial integration of the saturable absorber provides a charge transfer route in the growth direction. This process limits the high temperature operation of self-pulsating AlGaInP lasers, because the absorber is saturated by the thermally induced transfer of charge carriers from the MQW gain region. In 1998 Summers and Rees managed to raise the upper limit of self-pulsation to 100 ^{0}C, [59]. In order to minimise the charge leakage effect they included three quantum wells in the cladding layer to reduce the transferred carrier density per well by a factor of three compared to a single absorber. However, they a reported threshold current density of 3.1 kA/cm^2 at 20 ^{0}C which is very high (compare with a $J_{th} \sim 300$ A/cm^2 for the SSQW CW lasers in [49]). The 100 ^{0}C self-pulsating laser of Summers and Rees appears to be the current state of the art.

5.3 Experimental Characterisation

Through the very kind the help of Mr. David Martin of OPTRONICS IRELAND and formerly of TOSHIBA, we were able to obtain a small number of samples of the TOSHIBA TOLD9450MC lasers which were mentioned earlier. The following sections contain experimental data pertaining to these devices. The experimental setup used was very similar to the one already described in Fig. 3.1 on page 44. The only major differences were that mir-

rors used were metallic rather than dielectric, and the microscope objective used to collimate the emitted light from the laser diode had a slightly longer working distance, and consequently a smaller NA.

5.3.1 Light-Current Characteristics

Light Current (LI) curves were recorded at 20 K intervals over the temperature range 77 K $\leq T \leq$ 290 K. Fig. 5.2 is typical of the behaviour observed for the three laser diodes which were studied. The wavelength shift over the 210 K temperature range was around 30 nm and was accounted for in the photodiode responsivity. The most striking feature with respect to this

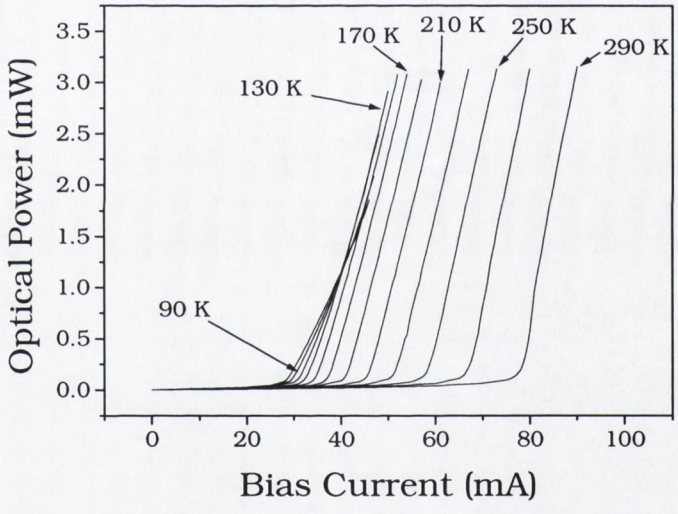

Figure 5.2: Typical Light-Current curves for a TOSHIBA TOLD9450MC red self-pulsating laser diode in the temperature range, T, 77 K $\leq T \leq$ 290 K. Note: Only every second curve is labelled on the graph.

series of curves is the behaviour the of slope efficiency, particularly at low temperature. Usually there is a steady increase in the slope efficiency at lower temperatures as the various temperature dependent nonradiative recombination processes play smaller roles. However, in this case, the slope

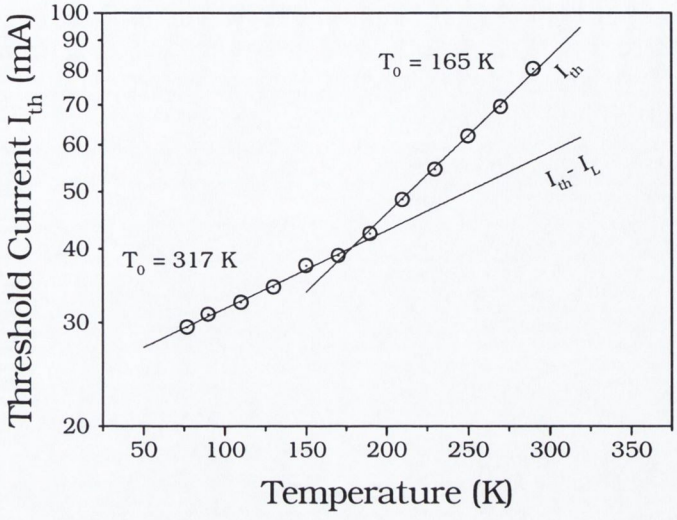

Figure 5.3: Semi-logarithmic plot of I_{th} versus temperature

efficiency appears to be fairly constant from 290 K down to around 130 K. Below this temperature it appears to decrease with further decreasing temperature. The reason for this behaviour is unclear, but it may be related to the behaviour of the near field pattern in section 5.3.3.

Fig. 5.3 shows a semi-log plot (as is conventional) of the threshold current, I_{th}, as a function of temperature. It is clear from this graph that there are two well defined values for the characteristic temperature, T_0. At lower temperatures (in the range 77 K $\leq T \leq$ 180 K) the threshold current in the device is only weakly dependent on temperature, with typical values of T_0 being around 300 K. At 180 K there is a cross-over point (often called the break-point temperature, [8]) and the value of T_0 drops dramatically to around 165 K, the lower value indicating a much more sensitive dependence of threshold current on temperature. Leakage currents begin to play a role in determining the threshold current of the laser above this break-point temperature, as carriers gain enough thermal energy to flow over the heterobarrier without recombining. This type of behaviour is well known for quantum well

lasers and the values of T_0 observed agree well with those in the literature, [60]. By extrapolating the line defining the lower temperature T_0 up to room temperature it is then possible to estimate the leakage current contribution to threshold current, [61]. For example at 210 K the leakage current only contributes 4.2 mA to the 48.5 mA threshold (just under 9%). By the time room temperature is reached (290 K) the leakage current contributes 24 mA to the 80.5 mA threshold (30%). This goes a long way towards explaining the temperature sensitivity of visible self-pulsating lasers, as demonstrated by Summers in [58].

It is also interesting to look at the behaviour of the polarisation resolved LI curves with temperature, Fig. 5.4 and 5.5. There are signs of carrier pinning down to around 170 K. Below this temperature, there appears a small component of lasing light begins to appear in the polarisation resolved TE polarisation. This is not perhaps surprising, since we are dealing with a strained MQW active region. Normally, in a QW laser with no strain the light and heavy hole valance bands are degenerate at $k = 0$. The transition strength from the conduction to the lowest energy heavy hole valance band is considerably stronger for the TE polarisation, pg. 81 of [62]. In contrast the transition from the conduction band to the light hole valance band is favoured by the TM polarisation. However, since the TE mode has a slightly larger reflectivity coefficient at the facet as well as a larger overlap (Γ) with the gain region, it is usually the predominant lasing mode. Introducing strain in a quantum well breaks the degeneracy of the light and heavy hole valance bands, pg. 442 of [7]. Compressive strain broadens the band gap and raises the heavy hole band above the light hole band, while tensile strain shrinks the bandgap and brings the light hole band above the the heavy hole band. In this case the laser diode has a compressively strained MQW active region, and thus the emission is almost exclusively in the TE polarisation at room temperature for the reasons outlined above. However, moving to lower temperatures can result in movement of the bands thus increasing the

probability of lasing in the TM polarisation.

5.3.2 Self-Pulsating Frequency Characteristics

The parameter space over which self-pulsation was sustained by the red lasers was also investigated over a wide temperature range. It was found that the lasers only exhibited self-pulsation approximately in the range 230 K $\leq T \leq$ 330 K. This is a considerably smaller self-pulsating temperature range when compared to the CD laser which exhibited self-pulsation down to around 110 K. Fig. 5.6 shows a typical plot of the variation of self-pulsation frequency with bias current over the temperature range 230 K $\leq T \leq$ 290 K. The relationship between self-pulsating frequency and bias current appears to be quite linear and the slope of these curves seems to be independent of temperature. Fig. 5.7 shows the same data re-plotted as a function of normalised bias current. Two things immediately stand out. Like the infrared CD lasers, the curves clearly do not follow the standard square root rule commonly observed for relaxation oscillations, Eq. (3.8), on page 51 of chapter 3. However, unlike their infrared counterparts, temperature appears to have some impact on the frequency (y-axes) intercept of the curves (in the case of the CD laser the curves were laid nearly on top of each other, in Fig. 3.5). The impact of the temperature on the slope is small. The difference in the trends observed for the infrared CD laser and the red self-pulsating laser may be due to the extra saturable absorbing layer. It was noted that on occasion, under large bias currents, double pulsing was observed. This raised the question, whether under certain conditions, there were two competing processes endeavouring to produce pulsed emission. For example, perhaps the self-focusing effect identified in CD type lasers might be competing with the type of saturable absorption process which produces pulse emission in the simple two-section self-pulsating laser at the relaxation oscillation frequency. Alternatively, double pulsing can sometimes be observed in gain switched lasers when the laser

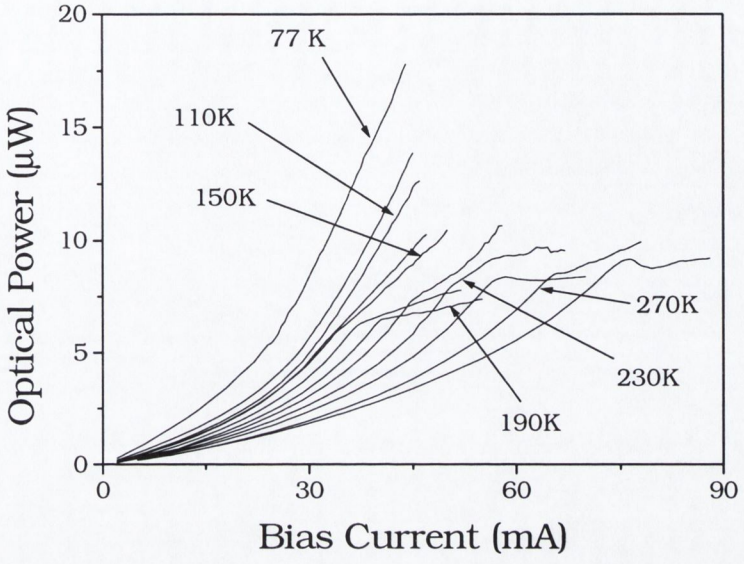

Figure 5.4: Typical polarisation resolved, LI curves for a TOSHIBA TOLD9450MC DVD laser in the temperature range 77 K $\leq T \leq$ 310 K.

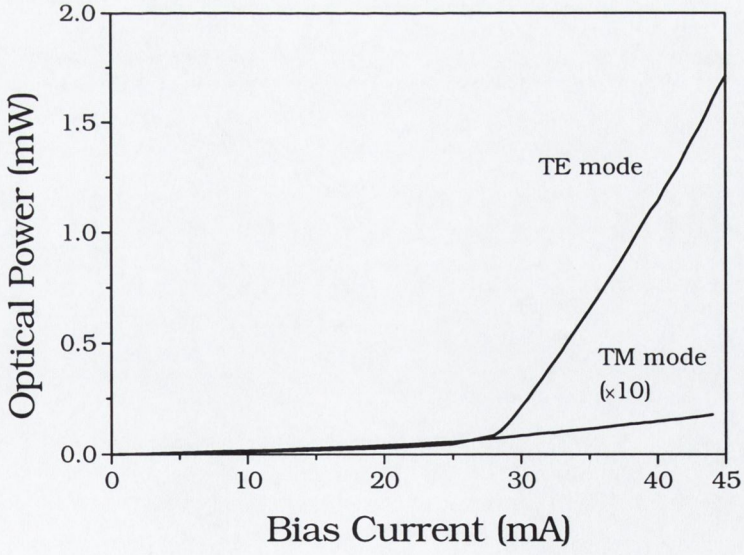

Figure 5.5: Normal, and polarisation resolved LI curves recorded at a heatsink temperature of 77 K.

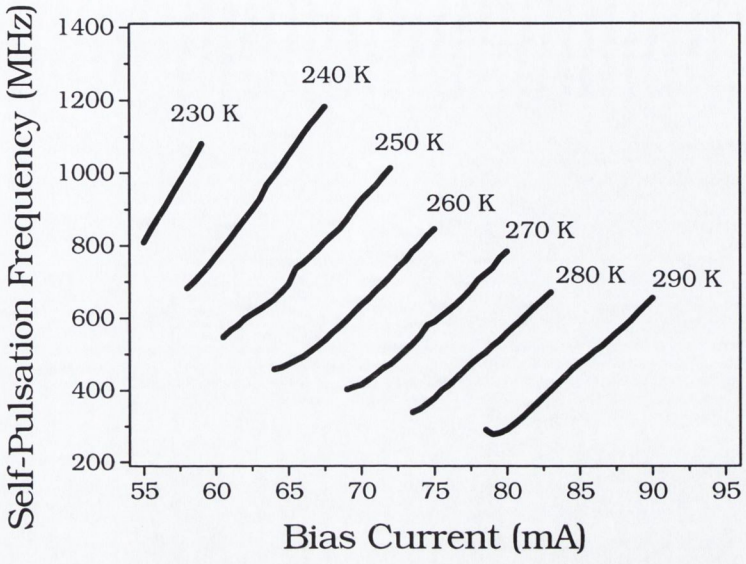

Figure 5.6: Self-Pulsation frequency versus bias current measured at 10 K intervals, in the temperature range 230 K $\leq T \leq$ 290 K.

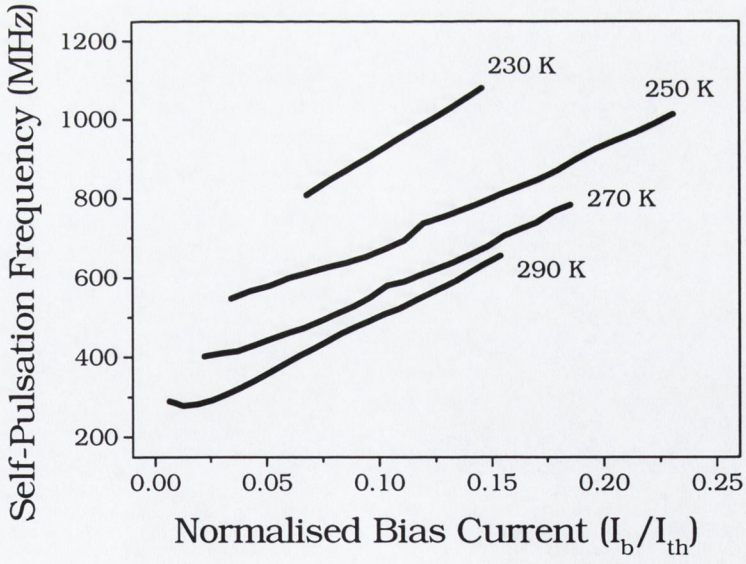

Figure 5.7: Self-Pulsation frequency versus normalised bias current in the temperature range 230 K $\leq T \leq$ 290 K. Note: For clarity only every second curve is shown.

is over-pumped, which might explain why this phenomenon was only observed under large bias currents. However, it should be noted that there was no tangible experimental evidence to substantiate either of these hypotheses.

5.3.3 Near Field Characteristics

The behaviour of the near-field was investigated using an experimental set-up similar to that described on page 66 of section 4.4. Again the only major difference was the use of metallic mirrors and the NA of the collimating lens, both of which were previously mentioned at the start of section 5.3. The near-fields were analysed using the techniques outlined on page 68 of section 4.2.2. The peak displacement, $(\bar{x} - x_0)$ and the standard deviation of the intensity distribution around $\bar{x}$ were calculated using Eq. 4.1 and 4.2 and are presented in Fig. 5.8 for a number of representative heatsink temperatures. Fig. 5.8 (a) and (b) show the behaviour of $(\bar{x} - x_0)$ and σ with bias current at 140 K. At this heatsink temperature the laser is operating in CW emission and the behaviour of the peak displacement is not very well defined. There are some indications of spatial hole burning. Below threshold the asymmetry of the lasing emission appears greater than that of the polarisation resolved spontaneous emission. Once above threshold this position is reversed and the $(\bar{x} - x_0)$ even changes sign for the lasing emission. (This type of behaviour was also seen CD lasers when not self-pulsating at low temperatures.) σ follows the same trend for all temperatures. Its value decreases until around threshold and then settles to around 2.0μm. At 230 K the onset of self-pulsation has just been reached and the spread in the values of $(\bar{x} - x_0)$ has settled somewhat. However, $(\bar{x} - x_0)$ for both the stimulated emission and the polarisation resolved spontaneous emission is predominantly positive indicating that the mode is being predominantly guided off-centre. At 290 K the device is now exhibiting robust self-pulsation. The peak displacement is now spread around the centre of the active region. It should be noted that

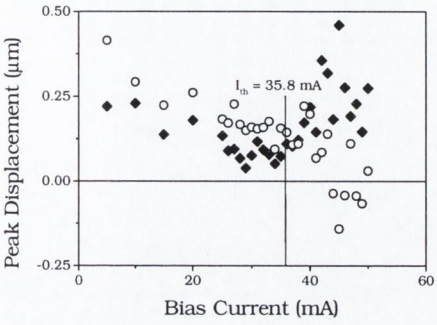

(a) $(\bar{x} - x_0)$ vs I, 140 K

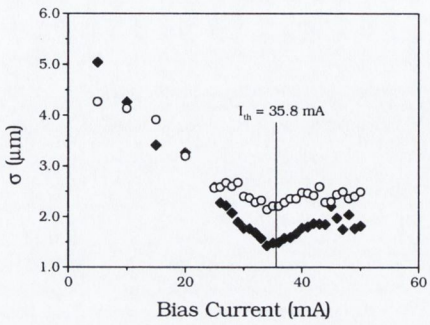

(b) σ vs I, 140 K

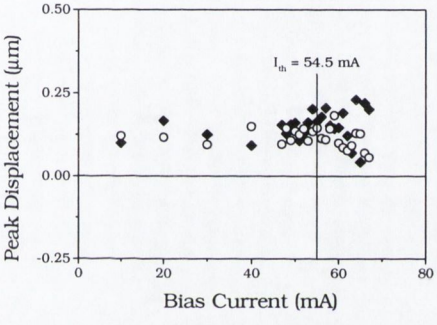

(c) $(\bar{x} - x_0)$ vs I, 230 K

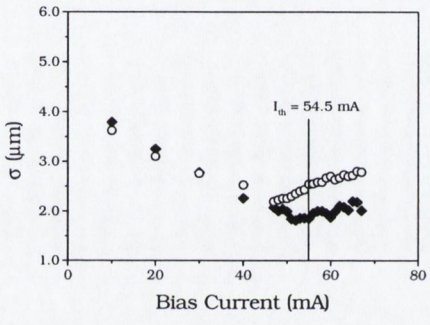

(d) σ vs I, 230 K

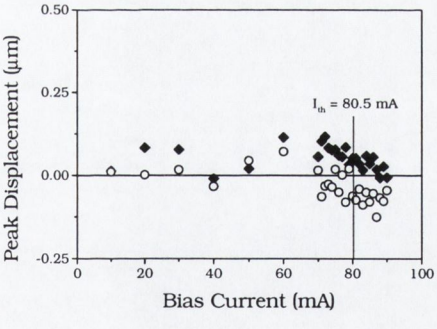

(e) $(\bar{x} - x_0)$ vs I, 290 K

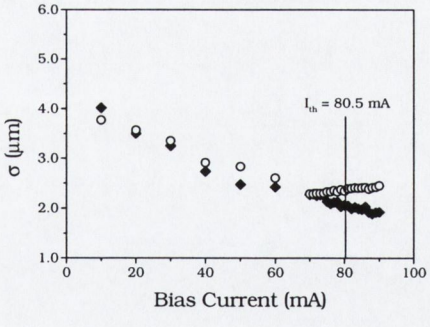

(f) σ vs I, 290 K

Figure 5.8: Six representative graphs which show the variation of both $(\bar{x} - x_0)$ and σ with bias current for heatsink temperatures of 140 K, 230 K and 290 K. The black diamonds represent the spontaneous emission, while the white circles represent the stimulated emission.

the behaviour of the $(\bar{x} - x_0)$ for the spontaneous emission is very different from that observed in the CD lasers in Fig. 4.9. This suggests that these particular red self-pulsating lasers are not using any waveguide modification effects in order to enhance self-pulsation.

In section 5.3.1 mention was made of the anomalous behaviour of the external quantum efficiency in Fig. 5.2. It may be possible to explain this behaviour by reference to Fig. 5.8. At heat sink temperatures below 140 K σ decreases until threshold and then begins to increase again. As the temperature is increased this trend changes. At 230 K σ plateaus at threshold while at 290 K it continues to decrease with increasing bias current. This indicates that below 140 K guiding reaches its optimum at threshold and then worsens as the bias current is increased. This would have a corresponding detrimental effect on the external quantum efficiency of the laser. At room temperature the guiding improves with increasing temperature which would have a positive effect on the external quantum efficiency.

5.4 The Future of Self-Pulsation in Red Laser Diodes

Experimental characterisation of packaged red AlGaInP self-pulsating D-VD lasers has highlighted the problems of obtaining robust self-pulsation over a wide temperature range with acceptable bias currents. It has been shown that leakage current accounts for over 30% of the total bias current at threshold for room temperature operation, and that these devices only exhibit self-pulsation over a very narrow range of operating conditions. Like their infrared counterparts the self-pulsating frequency does not obey the square root relaxation oscillation law. However, it can be seen that the self-pulsation frequency is considerably more sensitive to temperature changes. It is also clear from the near-field studies that these devices do not make use of any waveguide modifications during pulse formation in order to enhance

self-pulsation by carrier induced self-focusing effects.

Given these results, and what has been learned from studies of self-pulsation in infrared laser diodes, the natural question to ask is how to go forward from here? Two problems must be solved if red self-pulsating lasers are to be realised. The first hurdle which must be overcome, is to bring the threshold current down to an acceptable value by reducing the amount of carrier leakage across the heterobarrier. The structure proposed by Chang [53], shows considerable potential. They inserted a tensile strain barrier cladding layer (TSBC) in order to increase the potential barrier, thus reducing the leakage current. This group had previously employed the same strategy to increase the electroluminescence intensity of an AlGaInP yellow-green LED, [63]. The second problem is the temperature range over which the laser diode exhibits self-pulsation, and the associated low RIN. All current thinking on this problem has revolved around introducing extra saturable absorbing layers. In terms of acceptable self-pulsation temperature range, the structure of Summers and Rees [59] is still the best, with self-pulsating operation up to 100 ^{0}C. However, the extra losses introduced by including extra saturable absorbing layers has caused the threshold current densities to be driven up to 3.1 kA/cm^2 which is unacceptable for a practical laser diode. A solution, other than introducing extra losses is required. The structure of Chang [53] is very interesting because they have shown that it is still possible to make a red laser diode with an acceptable threshold current which is gain guided. This result shows indirectly, that it should be possible to exploit the kind of guiding/guiding effect identified in infrared CD laser diodes, and still retain an acceptable threshold current. In order to achieve self-pulsation in this device, it will be necessary to modify the effective refractive index seen by the gain region appropriately, to obtain the same type of instability which leads to self-pulsation in CD lasers. This might be achieved by varying for example, the thickness and composition of the current blocking layers in order to optimise their influence on the effective refractive index profile seen

by the mode propagating along the laser diode. It might be necessary to grow additional guiding layers below the active region, or alter the geometry of the laser diode in some novel way in order to achieve the optimum result. This proposed solution may prove a viable method for achieving robust self-pulsation over a wide temperature range in red laser diodes, as well as in future shorter wavelength laser diodes.

Chapter 6

Applications of CD Self-Pulsating Lasers

6.1 Introduction

With the development of fibre-optic transmission systems in the 1970s and in particular the introduction of single mode fibres for high-speed and large-capacity data transmission there has been a revolution in information transport. New communications services such video conferencing and the recent internet explosion are continuously pushing the bandwidth limit. The continual transformation between the electrical an optical domains at switching stations is proving to be one of the major bottlenecks. As a result there is an increasing drive towards optical transparency in communications networks. This necessitates the development of new electro-optic components to perform tasks which were previously executed only in the electrical domain. Self-pulsating lasers have many potential applications in all-optical networks, for example, clock distribution, clock extraction, and optical multiplexing and demultiplexing. The chapter begins with a discussion of electro-optic synchronisation of self-pulsating lasers. A description of how the simple rate equation model introduced in chapter 2, and validated in chapter 3, can be modified to describe electrical/optical synchronisation of self-pulsating CD lasers is then presented, along with corroborating experimental data.

6.2 Electrical/Optical Synchronisation of Self-Pulsating Lasers

When a self-pulsating laser diode is subjected to a periodic electrical or optical signal, and if the frequency of the applied signal is not too different from the free-running self-pulsation frequency, then providing certain other conditions are met, the frequency of the self-pulsating laser will change and become *synchronised* to the frequency of the applied signal. Fig. 6.1 illustrates this phenomenon. The top diagram shows a self-pulsating CD

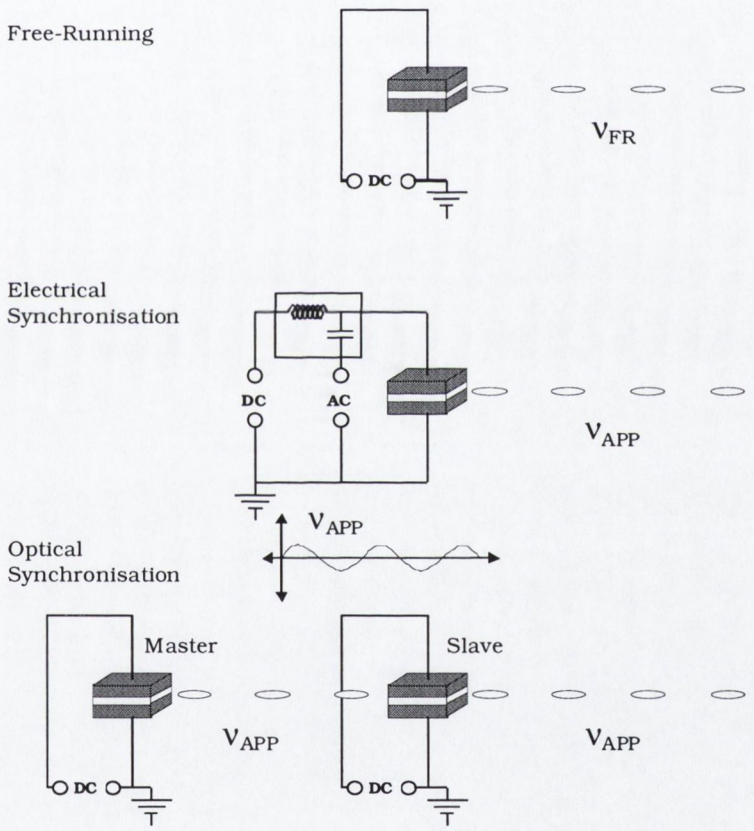

Figure 6.1: Illustration showing both electrical and optical synchronisation of a self-pulsating laser.

laser which has been DC biased and is emitting a train of pulses at the free-running self-pulsation frequency, ν_{FR}. Directly below this is a diagram of a

similar laser diode which has been synchronised to an electrical modulation. The frequency of the emitted pulse train is the same as the frequency of the applied electrical signal, ν_{APP}. At the bottom is a diagram of a laser which has been synchronised to an optical signal from a frequency stabilised master laser. Again, the frequency of the emitted pulse train from the slave laser becomes synchronised to the frequency of the optical signal, ν_{APP}.

Both electro-optical synchronisation and all-optical synchronisation have been reported in many different types of self-pulsating lasers. The earliest reported use of a self-pulsating laser diode for clock extraction was in 1988 by Jinno *et al*, [64]. The device used was a three section DFB laser with one section biased below transparency. Subsequently the same group reported optical re-timing regeneration (clock extraction) in a similar laser at a bit rate of 200 Mbit/s, [65]. In 1993 Farrell *et al* reported all-optical clock extraction in a twin section laser diode, at a bit rate of 678 Mbit/s using a non return to zero (NRZ) data stream, [66]. In the same year 2.5 Gbit/s return to zero (RZ) and 5 Gbit/s NRZ clock extraction was demonstrated with another twin section laser, [17]. In 1994 Feiste *et al* demonstrated 18 Gbit/s clock extraction with a two section DFB laser [67].

One thing which all these reports have in common is that the laser diode in question was multi-sectioned. In order to achieve low cost clock extraction it would be much more desirable to use a single contact device. One possible candidate device which could fulfil this role is the self-pulsating CD laser which can be easily synchronised to an external modulation.

One of the easiest ways to determine whether synchronisation has occurred is to examine the RF spectrum. Fig 6.2 (a) shows an RF spectrum for a free-running self-pulsating CD laser. The dominant feature in this spectrum is a broad peak at $\nu_{FR} = 1.034$ GHz, which is due to the self-pulsation. Fig 6.2 (b) shows the RF spectrum for the same laser, under similar bias conditions, when a 1 GHz sinusoidal electrical modulation, ν_{APP}, of amplitude -10 dBm was applied. Two changes in the RF spectrum are clearly apparent.

The peak is pulled from the free-running frequency, ν_{FR}, to ν_{APP} and the width of the peak decreases dramatically. Fig 6.3 (a) shows RF spectrum for both the free-running laser and the synchronised laser under the same bias conditions. The width of the self-pulsation peak is approximately 10 kHz. Fig 6.3 (b) shows the RF spectrum of the synchronised laser at the resolution bandwidth limit of the RF spectrum analyser. At this resolution the width of this peak was measured to be approximately 10 Hz. In general this width is usually limited by the frequency stability and phase noise of the signal generator. This behaviour is indicative of synchronisation.

6.2.1 Modelling Synchronisation in CD Lasers

The rate equation model which was used to simulate synchronisation is self-pulsating CD lasers is very similar to the models described in chapters 2 and 3, [68, 69, 70, 71].

$$\frac{dN_1}{dt} = \frac{I_b}{eV} + \frac{I_{APP}(t)}{eV} - \gamma_{e1}(N_1)N_1 - \Gamma_1 G(N_1)P - \frac{N_1 - N_2}{\tau_{12}} \tag{6.1}$$

$$\frac{dN_2}{dt} = -\gamma_{e2}(N_2)N_2 - \Gamma_2 G(N_2)P - \frac{N_2 - N_1}{\tau_{21}} \tag{6.2}$$

$$\frac{dP}{dt} = \left[\Gamma_1(N_1)G(N_1) + \Gamma_2(N_2)G(N_2) - \frac{1}{\tau_P}\right]P + kP_{APP} + \beta B N_1^2 + F_P(t) \tag{6.3}$$

Eq. 6.1 deals with the changing carrier density in the central region which is in gain, (section 1). The first term describes the DC current injected into the active region while the second term covers the case of electro-optic synchronisation by the inclusion of an electrical modulation. I_b is the bias current, $I_{APP}(t)$ is the applied modulation to the bias current, e is the electronic charge, and V is the active region volume. The third and fourth terms describe the carrier density lost through non-radiative recombination and carrier diffusion. $\tau_1(N_1)$ is the density dependent carrier lifetime in this region. τ_{12} is the diffusion time from the central gain region (section 1), to

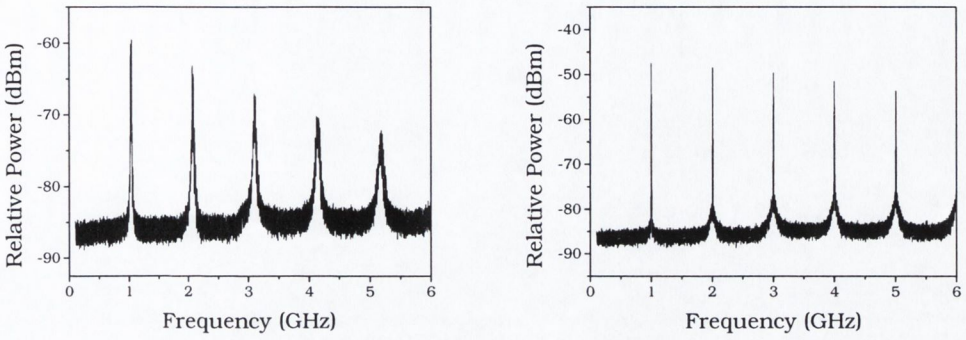

(a) (b)

Figure 6.2: (a) Typical RF spectrum for a SHARP LT022MD CD laser. The free-running self-pulsation frequency for this bias condition, ν_{FR} is 1.034 GHz. (b) RF spectrum for the same laser under identical bias conditions when synchronised to a 1 GHz sinusoidal electrical modulation at -10 dBm, ν_{APP}. (For both (a) and (b) RBW = 1 MHz and VBW = 10 KHz)

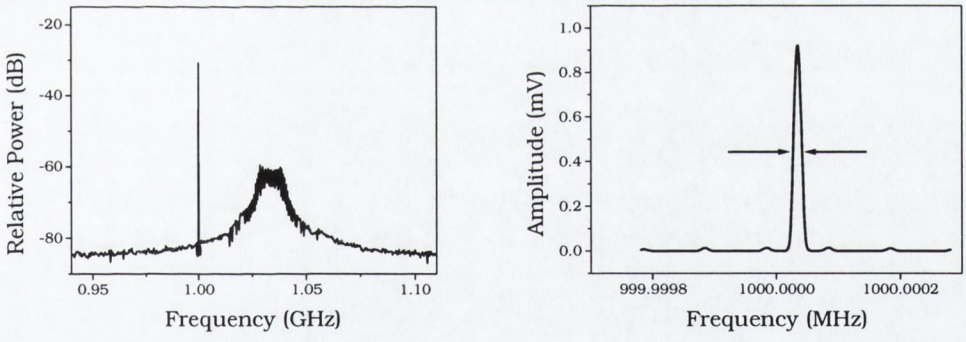

(a) (b)

Figure 6.3: (a) Comparison between the RF spectra for free-running laser and the synchronised laser under the same conditions, but on a much smaller span. (Free running RBW = 30 kHz and VBW = 300 Hz, Synchronised RBW = 30 Hz and VBW= 30 Hz) (b) Resolution bandwidth resolved RF spectrum for the synchronised laser under the same conditions. (RBW = 10 Hz, and VBW = 10 Hz)

the saturable absorber regions either side (lumped section 2). The last term describes the carrier density which has been transformed into photon density through stimulated emission. Eq. 6.2 describes the changing carrier density in the saturable absorber regions. Terms one and two play similar roles as terms three and four in Eq. 6.1. Term three describes the carrier diffusion from section 2 to section 1. Finally, Eq 6.3 describes the changing photon density. The first two terms describe the photon density generated in both sections while the third term, $1/\tau_P$ describes the losses. The fourth term take into account the possibility of an externally injected optical modulation, in the case of all-optical synchronisation. The fifth term describes the contribution to the photon density by spontaneous emission in section 1. The contribution to the photon density by spontaneous emission from section 2 was ignored because it was considered negligible with respect to the other terms in this equation. β is the fraction of the spontaneous emission coupled to the lasing mode and B is the bimolecular recombination coefficient. The last term, $F_P(t)$ is a Langevin noise source that represents spontaneous emission noise.

6.2.2 Jitter in Self-Pulsating CD Lasers Synchronised to Periodic Electrical Signals

Clock extraction and the potential for optical clock distribution by synchronisation of laser diode self-pulsation to applied electrical and optical signals was introduced in section 6.1. To date, the major thrust of research has been in the development of self-pulsating lasers which pulsate stably at frequencies in excess of 40 GHz, for very high speed long haul datacoms applications [19, 20, 21, 72, 73, 74]. However, for low cost short haul systems such as local area networks (LANs) there may be a role for cheap self-pulsating lasers in clocking subsystems which operate at data rates around 1-2 Gbit/s. For such a clocking subsystem an important consideration in determining the fidelity

of the clock extracted from the data stream is some knowledge of the contribution to timing jitter in the derived clock by the self-pulsation dynamics. Fig. 6.4 illustrates the detrimental effect timing jitter can have on a clock pulse train. The top idealised clock pulse train has no timing jitter, while the

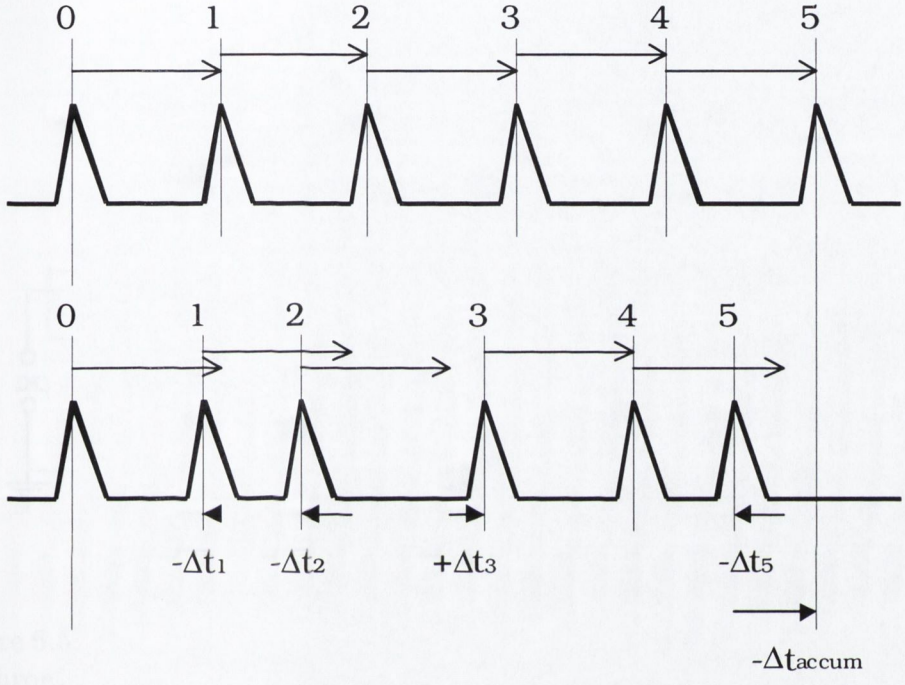

Figure 6.4: Illustration showing the effect of timing jitter on an idealised clock pulse train.

bottom clock pulse train has. Δt_i is the pulse to pulse jitter between pulse $i-1$ and pulse i. After five pulses the accumulated timing jitter, Δt_{accum}, is now so great that the clock pulse train would be nearly 90^0 out of phase with the data stream. If this clock was used to decide when to read a 1 or 0 in a data stream, the measurement would take place half way between two bits, and would probably produce an error.

In this section, both experimental and simulated results are presented which aim to quantify the effect of synchronisation on both the pulse to pulse timing jitter and the accumulated timing jitter in CD lasers which

have been synchronised to an electrical modulation.

The experimental setup used to study the jitter of an electro-optically synchronised self-pulsating CD laser is illustrated in Fig. 6.5. The CD laser

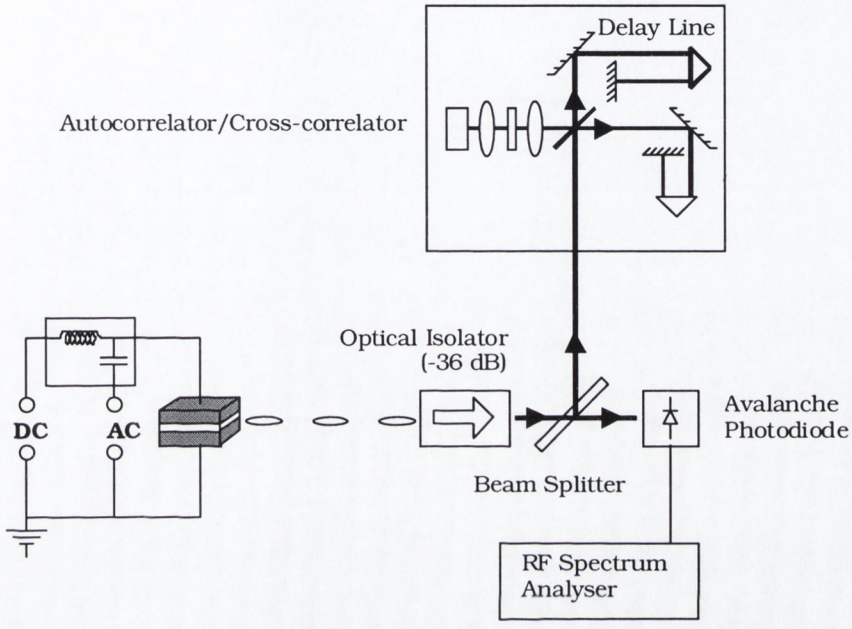

Figure 6.5: Experimental Setup used to study the jitter of an electro-optically synchronised self-pulsating CD laser. The Avalanche photodiode was used to monitor the frequency and had a bandwidth of 2.2 GHz.

was a SHARP LT022MD. A small amplitude sinusoidal electrical modulation was applied across the capacitor on one arm of a bias tee, along with the normal DC bias through the inductor of the other arm. The frequency synthesizer used to generate the electrical modulation was a HP 8657B. The collimated output of the laser diode passed through a Faraday optical isolator (with isolation -36 dB), and was incident on a beam splitter. One portion of the beam was directed onto an Avalanche photodiode (bandwidth 2.2 GHz), which was connected to a RF spectrum analyser. This made it possible to monitor the synchronisation of the laser to the applied electrical modulation. The other portion of the beam was directed into an autocorrelator (see

section 2.6.2 for a full description). In autocorrelation the time-averaged signal from a second harmonic crystal will depend on the time delay, Δt, between the two arms. When Δt is varied about zero, an autocorrelation trace is obtained with a FWHM proportional to the average pulse width, [24]. However, by increasing the length of the fixed arm, it is possible to vary Δt about nt_p, and cross-correlation traces are obtained (n is an integer and t_p is the average pulse period). The cross-correlation FWHM at a given order, n, is determined by the the average pulse width (as measured at $n = 0$) and the average timing jitter accumulated over n pulses.

Fig. 6.6 shows a plot of the cross-correlation FWHM versus n, obtained with a CD laser diode with a free-running self-pulsation frequency of 2 GHz and for the same CD laser when synchronised to a small amplitude applied sinusoidal electrical signal of frequency 2 GHz. For the free-running laser, the cross-correlated FWHM increases monotonically with increasing n. Since the average pulse width is measured when $n = 0$, this increase in FWHM can be attributed to the increasing jitter over n periods. The FWHM increase for the synchronised laser, at low values of n, is very similar to that of the free-running laser. An interesting point to note here, is that at $n = 0$ the FWHM of the synchronised laser is about 3 ps less than the FWHM of the free-running laser. The applied electrical modulation slightly increases the carrier density prior to pulse emission which results in a shorter optical pulse. This phenomenon was predicted in [68]. Above $n = 7$ the two curves begin to diverge markedly. In contrast to the behaviour of the free-running laser, the curve for the synchronised laser is flatter and the FWHM approaches a value of about 100 ps at $n = 25$.

Fig. 6.7 shows the calculated variance of σ_{JDC} with n when a CD laser is synchronized to an applied sinusoidal electrical signal and for a free-running CD laser. A train of 10200 pulses was simulated, the first 200 of which were discarded in order to discriminate against turn-on transients. The time between pulses separated by nt_p is determined and binned to produce jitter

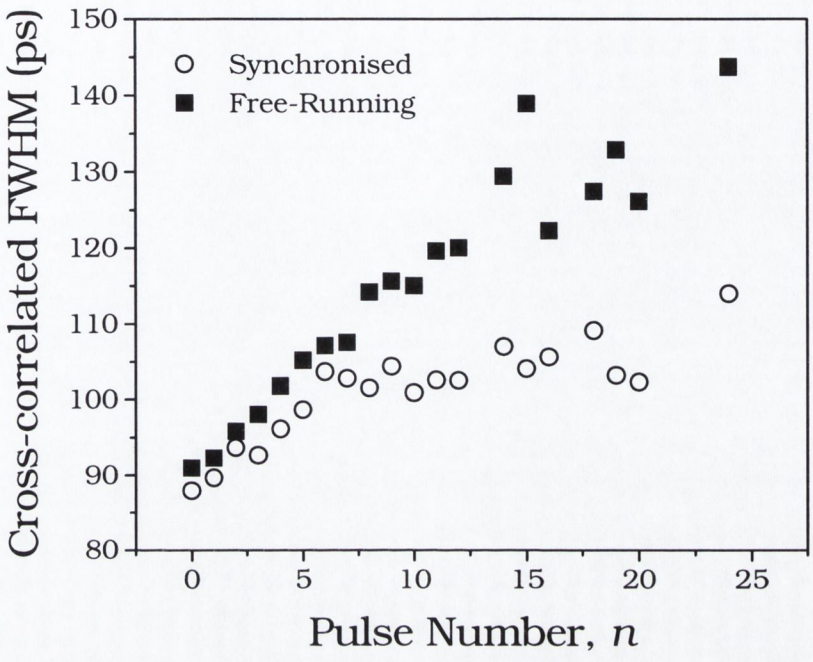

Figure 6.6: Plot of experimentally measured 2 GHz CD laser cross-correlation FWHM versus pulse number n. The free-running self-pulsation frequency in each case is approximately 2 GHz and the laser is synchronised to an applied electrical sinusoidal frequency of 2 GHz. The solid squares were measured for the free-running laser. The hollow circles were measured for the electro-optically synchronised laser.

distribution curves whose FWHM, σ_{JDC}, measures the timing jitter between pulses separated by nt_p [70, 75]. In this plot σ_{JDC} measures the calculated timing jitter between pulses separated by nt_p. The behaviour of σ_{JDC} with increasing n shows the same trend as is observed for the cross-correlation dependence on n, (Fig. 6.6). For $n = 1$ the pulse jitter for the synchronised laser and the free-running laser are similar. σ_{JDC} increases quickly and monotonically for the free-running laser. The value of σ_{JDC} for the the synchronised laser appears to saturate after about $n = 6$, and settles down to a value of about 40 ps.

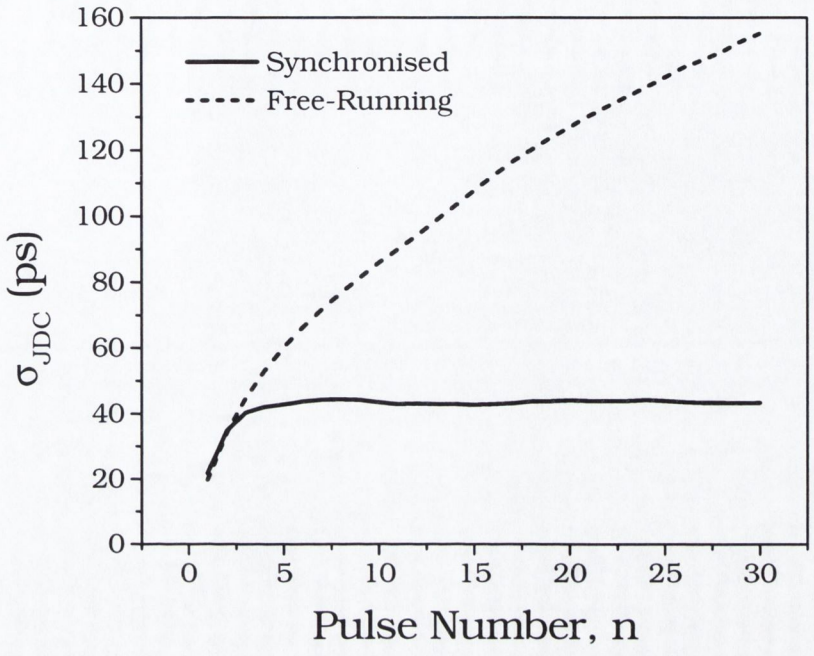

Figure 6.7: σ_{JDC} versus n. The dashed line represents σ_{JDC} calculated for a free-running CD self-pulsating laser. The solid line represents the same quantity calculated for the CD laser synchronised to a sinusoidal electrical modulation.

A number of important inferences can be drawn from these results. The time domain results (both experimental and calculated) confirm what is observed in the RF spectrum. Synchronisation is characterised by a very narrow fundamental peak in the RF power spectrum. It can be seen that this decrease results from the saturation of the accumulated jitter in the synchronised laser after 6 or 7 pulses. This saturation of the accumulated timing jitter is due to the much diminished frequency drift when the periodic signal interacts with the laser pulse separating process. Synchronisation does not appear to substantially change the pulse to pulse jitter from the free-running laser. This result has very important implications for the use of self-pulsating CD lasers in clock extraction subsystems. Very long strings of zeros in a da-

ta stream could result in a timing error since the slave clock would not be synchronised. Since the slave laser would now be essentially free-running the timing jitter would rapidly accumulate and lead to an error. In a practical system the data would therefore have to be encoded, to ensure that too may zeros did not arrive sequentially.

6.2.3 All-Optical Synchronisation of CD Self-Pulsating Laser Diodes

Following on from the discussions in section 6.2 the work presented in this section deals some of the aspects of all-optical synchronisation in CD lasers, with ultimate aim of demonstrating a viable all-optical clock extraction subsystem. In particular, experimental and theoretical results are presented regarding the phase difference between the injected optical signal and the synchronised self-pulsating laser diode emission. The phase difference dependence on detuning between the laser free-running self-pulsation frequency and the applied signal frequency, and on the injected signal power are investigated and the implications for a real clock extraction subsystem are explored.

To begin with, the experimental setup in Fig. 6.8 is discussed. The CD laser to be synchronised (the slave) and the laser (the master) that provides the optical input to the slave were both SHARP laser diodes, model LT022MD. The master laser was electro-optically synchronised by the application of a sinusoidal electrical modulation with frequency, $\nu_{APP} = 2$ GHz. The optical emission was collimated by a $\times 20$ microscope objective and was incident on a beam splitter. Synchronisation was verified by monitoring the portion of emission which passed through a beam splitter on an avalanche photodiode connected to an RF spectrum analyser. The remaining portion of the beam passed through a variable attenuator and a -36 dB faraday optical isolator. The isolator prevented light from the slave laser perturbing the emission from the master laser. The optical emission from the master

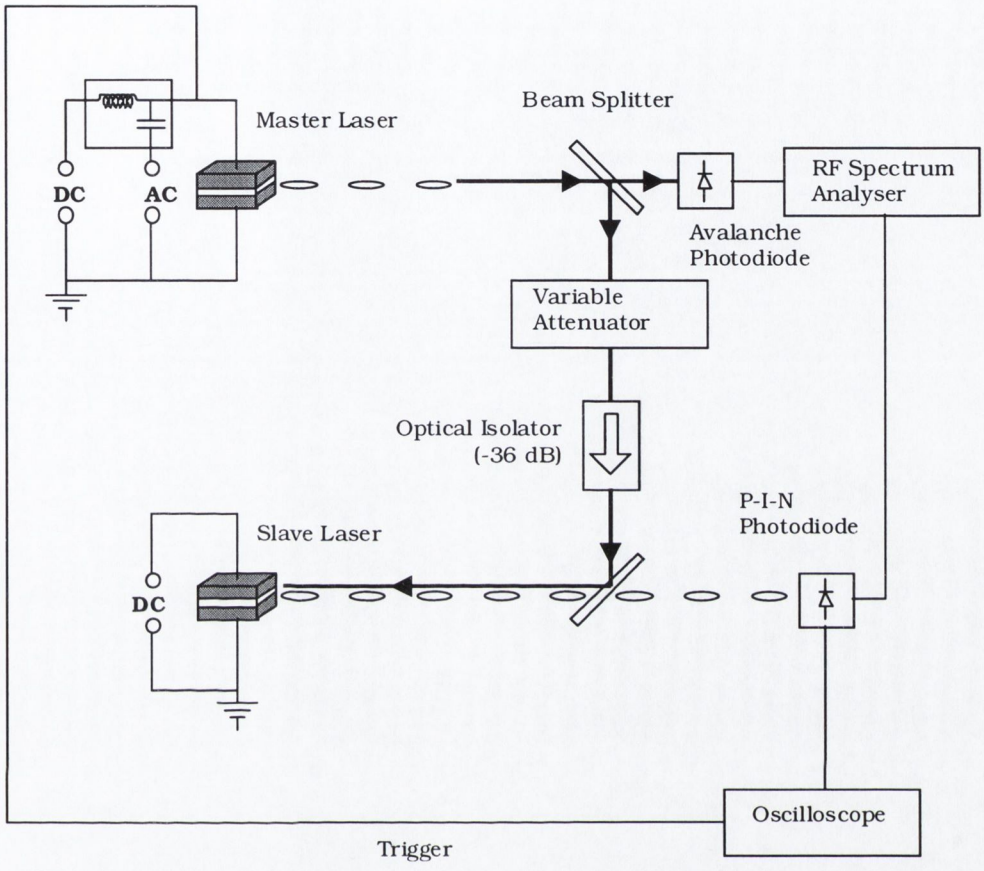

Figure 6.8: Experimental setup used to investigate the dependence of phase difference between the optical input and the output for a synchronised self-pulsating CD laser on the free-running self-pulsation frequency and input signal power.

laser was then coupled to the slave laser through another $\times 20$ microscope objective which also had the dual purpose of collimating the optical emission from the slave laser. The slave laser emission was monitored by a fast *p-i-n* photodiode. The electrical signal from this photodiode was split. One portion was taken to the RF spectrum analyser and the other portion was taken to a digital sampling oscilloscope which was triggered by the RF signal generator providing the electrical modulation applied to the master. If either the free-running self-pulsation frequency of the slave, ν_{FR}, was changed (by

varying the bias current) or the intensity of the optical emission originating from the master is varied (by changing the attenuation along the path of the beam) then the trace displayed on the oscilloscope shifts in time. This relative phase difference between the optical emission of the slave laser and the master laser, which is a function of the phase difference between the optical emission from the slave laser and the trigger, $\Delta\phi_D$, can thus be measured.

$\Delta\phi_D$ was measured as a function of ν_{FR} for a number of different injected power levels. For each data set $\Delta\phi_D$ was expressed relative to the frequency $\nu_{FR} = \nu_{APP} = 2$ GHz. The data is plotted in Fig. 6.9. The frequency

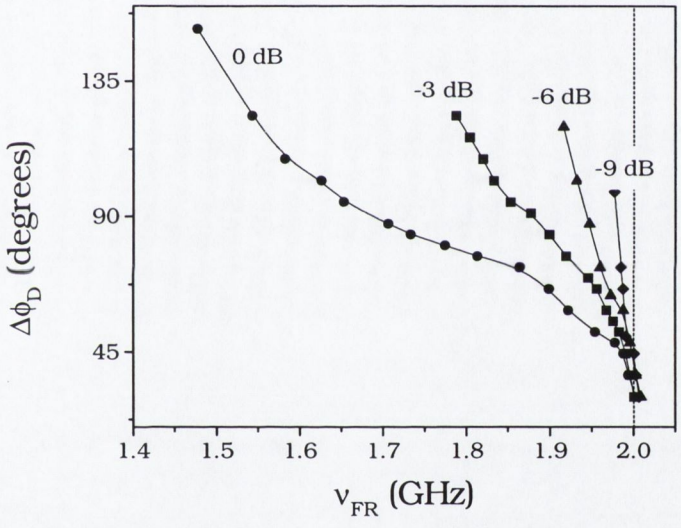

Figure 6.9: Experimentally determined dependence of the phase difference, $\Delta\phi_D$, between the optical emission of the the master and the free-running self-pulsation frequency of the slave, ν_{FR}, parameterised in terms of relative injected optical power. $\Delta\phi_D$ is expressed relative to $\nu_{FR} = \nu_{APP} = 2$ GHz.

range over which synchronisation occurs varies with injected signal power and shows a sharp cut-off at $\nu_{FR} = \nu_{APP}$. The total phase range over which synchronisation can be achieved is about 100^0, which is similar to the range reported for electro-optical synchronisation of a two section self-pulsating laser diode, [76].

In an effort to better understand these experimental results, this behaviour was modelled using equations 6.1 - 6.3. The term S_{APP} describes the simulated injected optical signal which for simplicity is treated as a train of rectangular pulses with a duty cycle of 10% and a frequency, $\nu_{APP} = 2$ GHz. Spectral detuning effects were neglected in the model. While spectral detuning would obviously affect the coupling between the master and the slave lasers, it has been shown that injection locking is not required for all-optical synchronisation and that these systems can still be used for synchronisation/clock extraction with wavelength changing, [21]. The free running self-pulsation frequency, ν_{FR}, in the slave laser was controlled by changing the bias conditions. $\Delta\phi_D$ was defined as the phase difference between the rising edge of the applied optical pulse and peak of the next output optical pulse. Fig. 6.10 shows the calculated dependence of the phase difference on ν_{RF} and on injected power. The power levels are expressed relative to the laser

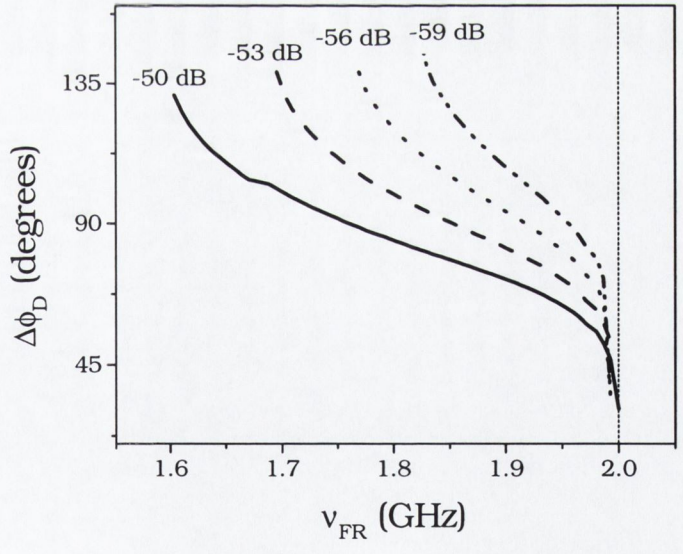

Figure 6.10: Calculated dependence of the relative phase difference, $\Delta\phi_D$, between the injected optical signal and the slave laser emission, ν_{FR}, parameterised in terms of relative injected optical power. $\Delta\phi_D$ is expressed relative to $\nu_{FR} = \nu_{APP} = 2$ GHz.

output power when $\nu_{FR} = 2$ GHz and 100% coupling of the injected signal to the lasing mode is assumed. The total phase range was about 90^0 which compares well to the experimentally determined value. The agreement between the trend of phase shift with detuning and incident power shown in Fig. 6.9 and Fig. 6.10 is also excellent.

Two points require further discussion. Firstly, both experiment and calculation show that optical synchronisation is only possible at these power levels for positive detuning of ν_{APP}. That is, ν_{APP} most be greater than ν_{FR}. This is certainly not the case for electro-optic synchronisation. Here synchronisation is possible for both positive and negative detuning of ν_{APP}. This is because a sinusoidal electrical modulation periodically injects and removes carriers from the active region. In this way extra carriers can hasten the onset of the next pulse, while the removal of carriers can delay it. In the case of optical synchronisation, the injected signal creates extra carriers, which for positive detuning of ν_{APP}, will hasten the next pulse. However there is no analogous way to remove carriers from the active region, and delay the onset the next pulse. Thus optical synchronisation is not possible for negative detuning of ν_{APP}, [68]. Secondly, it can be seen from both Fig. 6.9 and Fig. 6.10 that the variation of $\Delta\phi_D$ is greatest for low powers. This point is made clearer by Fig. 6.11. Here ν_{FR} was held fixed at 1.8 GHz and the relative injected power was varied over the range -58 dB to -48 dB. This dependence of phase on power has important consequences for potential all-optical clock extraction and distribution subsystems, since data or clock signals may travel from one element in a telecommunications system to another along different routes and thereby suffer different levels of attenuation along these routes.

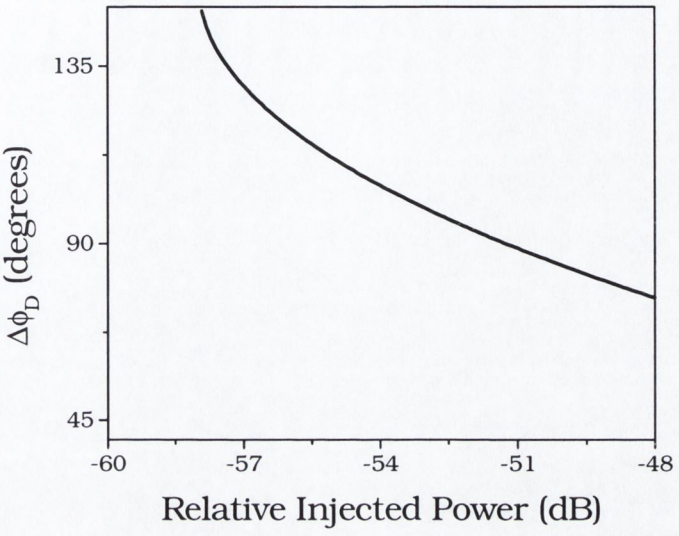

Figure 6.11: Calculated dependence of relative phase on injected signal power. $\nu_{APP} = 2$ GHz and $\nu_{FR} = 1.8$ GHz.

6.2.4 All-Optical Synchronisation with Frequency Division

Although methods of electronic clock recovery at gigabit per second rates have been demonstrated for optical time division multiplexing systems and networks, such techniques require subsequent optoelectronic conversion to generate an optical clock signal and ultimately meet the same bandwidth constraints as other electronic signal processing, [17]. Alternatively all-optical synchronisation with frequency division and multiplication using self-pulsating laser diodes has been demonstrated [64, 65, 77, 78], as has all-optical timing extraction with frequency division [66]. Clearly, inexpensive CD self-pulsating laser diodes have the potential to play an important role in large fan-out functions such as clock distribution with frequency multiplication or division from a single master clock and multiplexing or demultiplexing.

In general it should be possible to achieve synchronisation according to

Eq. 6.4, where n and m are integers greater than zero.

$$n\nu_{FR} \approx m\nu_{APP} \tag{6.4}$$

In the case where $n < m$, this is termed frequency multiplication while, if $n > m$ this is termed frequency division. This section contains both experimental and calculated results pertaining to case of the application of a periodic optical signal giving synchronisation with frequency division.

Synchronisation of two CD self-pulsating lasers with frequency division was successfully verified with the same experimental set-up illustrated in Fig. 6.8 and described in section 6.2.3. The bias conditions of both the master and slave lasers were adjusted so that ν_{FR} was approximately 4 GHz for the master and ν_{FR} approximately 2 GHz for the slave. The master laser was then electro-optically synchronised to exactly 4 GHz and ν_{FR} of the slave laser was varied around 2 GHz in order to achieve 2:1 frequency division. Fig. 6.12 shows plots of the upper limit, ν_{upper}, and the lower limit, ν_{lower}, of the free-running self-pulsation frequency of the slave laser where synchronisation can be achieved at a particular relative injected power. As the relative injected power is increased it can be seen from the graph that both ν_{upper} and ν_{lower} move to lower values of ν_{FR}, while the total synchronisation range increases.

The behaviour of self-pulsating CD lasers under all-optical synchronisation with frequency multiplication and division was extensively studied using the rate equation model described in section 6.2.2 by Egan, [71, 79]. The relevant results pertaining to all-optical synchronisation with frequency division are presented in Fig. 6.13. Fig. 6.13 shows the calculated phase difference, $\Delta\phi_D$, between injected optical signal and laser output as a function of ν_{FR} for three relative injected optical powers. The three individual plots correspond to the case of 1:1 synchronisation, $\nu_{APP} = 2.5$ GHz (top), 2:1 frequency division, $\nu_{APP} = 5$ GHz i.e. $\nu_{APP} \approx 2\nu_{FR}$ (middle), and 3:1 frequency division $\nu_{APP} = 7.5$ GHz i.e. $\nu_{APP} \approx 3\nu_{FR}$ (bottom). A number of significant differ-

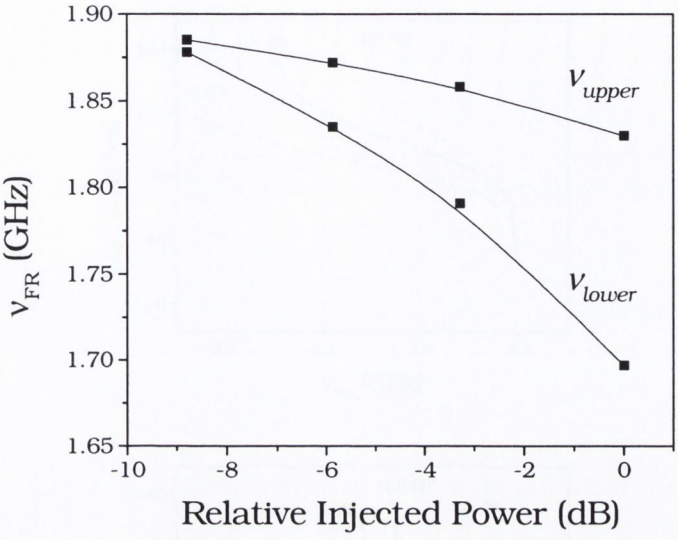

Figure 6.12: Experimentally determined synchronisation range with 2:1 frequency division. The labels ν_{upper} and ν_{lower} refer to the upper and lower frequency limits respectively, where synchronisation can be achieved at that relative injected power.

ences exist between these three plots. Firstly, the total range of free-running self-pulsation frequencies (ν_{upper} to ν_{lower}), over which synchronisation can be achieved decreases from the 1:1 synchronisation case, through the 2:1 frequency division case, down to the 3:1 frequency division case. Secondly, ν_{upper} is now somewhat smaller than 2.5 GHz (ν_{APP}) for the case of 2:1 frequency division, and ν_{upper} is considerably smaller than 2.5 GHz for the case of 3:1 frequency division. These trends are in excellent qualitative agreement with the experimental results in Fig. 6.12.

This leads to an interesting and important result. In Fig. 6.13, for a particular power level, the synchronisation range has an upper and lower frequency bound. For example, in the 1:1 case it is clear that for $\nu_{FR} = 2.3$ GHz (dotted line), synchronisation does not occur for an injected power of -4.8 dB. However, synchronisation does occur for -1.8 dB and 0 dB. For all high-

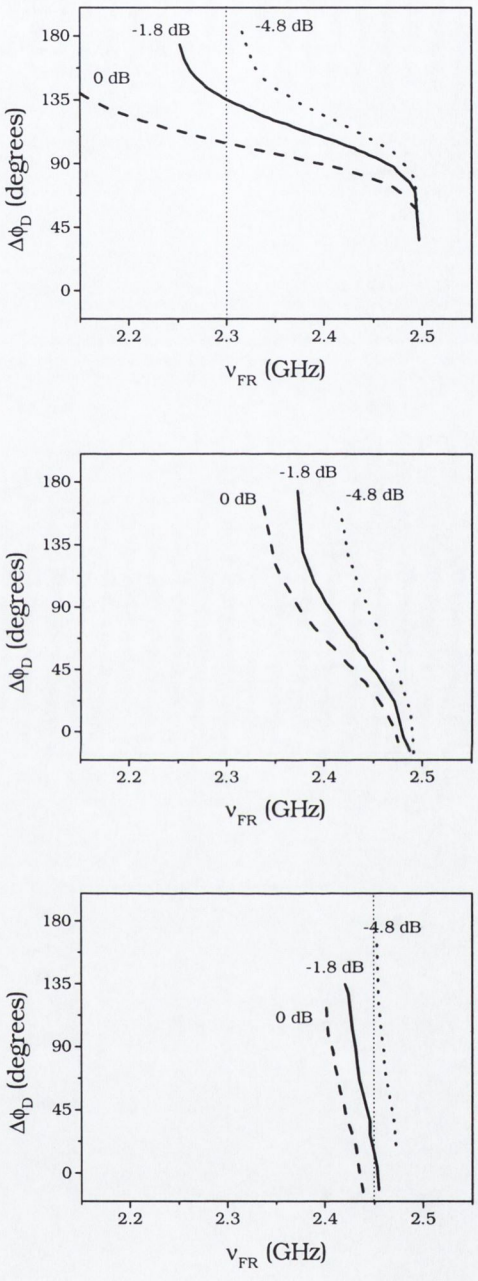

Figure 6.13: Calculated phase difference, $\Delta\phi_D$, between injected optical signal and laser output as a function of ν_{FR} for three relative injected optical powers. (top) 1:1 synchronisation, (middle) 2:1 frequency division, and (bottom) 3:1 frequency division.

er powers synchronisation always occurs at $\nu_{FR} = 2.3$ GHz, since ν_{lower} will move to lower frequencies while ν_{upper} remains fixed. In the 3:1 case, the situation is quite different. For example, when $\nu_{FR} = 2.45$ GHz (dotted line) synchronisation does not occur for a power level of -4.8 dB. As the power is increased to -1.8 dB synchronisation becomes possible, but if increased to 0 dB synchronisation is lost. For all higher powers synchronisation is not possible since ν_{upper} has moved below 2.45 GHz.

It has previously been shown in section 6.2.3 that there exists a power dependence of the phase difference between the injected optical signal and the laser output in a synchronised CD laser in the case of 1:1 synchronisation. For frequency division, it is found that the sensitivity to the input power is even greater. Not only does the phase difference between the signals change with power but there exists a power synchronisation window, which narrows as the frequency division ratio increases. This is very important in the context of the use of CD lasers for optical multi/demultiplexing and for the distribution of clock signals with frequency division. It needs to be taken into account in the design of optical signal processing elements that exploit frequency division, since it places severe constraints on the injected power level and the allowable variation in power, if synchronisation is to be achieved and maintained.

6.3 Summary

The predominant driving force behind the research presented in this chapter was the exploration of potential applications of the self-pulsating CD laser other than the data storage application they were originally designed for. Specifically, the main thrust was to understand the fundamental limitations of using a self-pulsating CD laser as a viable component of an optically transparent telecommunications system. By studying the effect of timing jitter on an electro-optically synchronised self-pulsating CD laser the inherent lim-

itations of using a CD laser as part of a clock extraction subsystem were assessed. Consequently, constraints on the type of encoding used could be inferred, if a self-pulsating CD laser were to be used in such a fashion. In addition to these findings, the work was later extended in [80] to include fundamental bandwidth limitations and bit error rates. The dependence of phase between the incoming data stream and the synchronised self-pulsating CD laser emission was then investigated in terms of injected power and detuning from the free-running self-pulsation frequency. The resultant consequences of this phase dependence was then explored in terms of a viable clock extraction subsystem. Finally, the potential for extending such a clock extraction subsystem for time division multiplexing/demultiplexing was considered and it's feasibility assessed.

Chapter 7

Conclusions

7.1 General Overview

This thesis has been primarily concerned with the formation and dynamics of optical pulses in semiconductor lasers. The possibility of exploiting semiconductor lasers as a source of short optical pulses has generated considerable interest, since their small size and ease of operation open up a wide range of applications which were previously infeasible or uneconomical. For example, optical pulses are used in high speed optical fibre communications systems for time division multiplexing and demultiplexing. Short optical pulses are also used for optoelectronic measurement applications such as electro-optic sampling, analog to digital conversion and impulse response testing of optical components. Short optical pulses are also of interest as a research tool in applications such as electroluminescence lifetime measurements.

There are a considerable range of techniques used to generate short optical pulses in semiconductor lasers. Gain switching is one of these techniques and involves turning on the the laser gain very rapidly using a fast pulse of pumping current. This fast pumping causes the population inversion, and the gain, to go considerably above threshold before laser oscillation has time to build up from the initial noise level in the cavity. Q-switching is another technique, where the cavity losses are set at some artificially high value,

allowing the population inversion and hence the gain to be pumped up to a value much larger than normally present in the laser. The cavity loss is then suddenly lowered and the spontaneous emission builds up at an unusually rapid rate, soon developing into an intense burst of laser oscillation. Q-switching of the laser cavity is often achieved in semiconductor lasers by using multi-section devices, where one section is biased very much in gain while another section is modulated around the transparency level. A third technique for producing optical pulses is mode-locking, and typically it produces the shortest pulses. Providing the bandwidth of the gain is sufficient to include a number of longitudinal modes, and if a constant phase relationship can be maintained between them, the fourier components will add to form a pulse. The larger the bandwidth of the gain spectrum, and the larger the number of phase-locked modes, the shorter the optical pulse. Amplification takes place after each cavity round trip, and under ideal conditions will result in a fourier transform limited pulse.

Selfpulsating lasers require neither extra modulation circuitry, nor extra optical components, to achieve pulsed emission. Instead, the origin of the self-pulsation lies in the interaction between the optical mode and the non-uniformly pumped gain material. It is the formation and evolution of these optical pulses in the semiconductor material that has been of primary concern in this thesis.

Until quite recently it was thought that the origin of self-pulsation in CD type structures was relatively well understood. However, the considerable problems which surfaced when attempting to design self-pulsating lasers in new material systems has necessitated a rethink. To date, most groups have sought to get around these problems by introducing extra saturable absorbing material, but this has had limited success over the operational range of temperature demanded by many of the applications. Introducing extra saturable absorbing material has also the unwanted side effect of driving the threshold currents higher, which further aggravates the temperature sensitivity of the

self-pulsation.

Traditionally it was thought that the highly temperature dependent carrier diffusion played a key role in controlling the self-pulsation behaviour in CD lasers. The temperature dependence of self-pulsation in infrared CD lasers is explored in chapter 3. Experimental characterisation over a wide temperature range revealed that CD lasers exhibit self-pulsation from approximately 100 K to above 400 K. The self-pulsation frequency was found to vary linearly with normalised bias current with a slope which was highly insensitive to temperature changes. This furnishes direct evidence that carrier diffusion does not play a first order role in controlling the self-pulsation. Based on the experimental characterisation, a phenomenological rate equation model including temperature was developed. Only standard parameters from the literature were used, and no attempt was made to fit the experimental data. However, very good agreement between simulation and experiment was still achieved. The model was able to correctly predict the temperature range over which this type of laser exhibits self-pulsation. It also provides corroborating evidence that carrier diffusion does not play a first order role in controlling the self-pulsation.

Although the temperature dependent rate equation was able to correctly predict the macroscopic details of the self-pulsating behaviour it had severe limitations in terms of understanding the underlying physics which causes the phenomenon. To this end, a more in depth investigation was performed on the spatial evolution of pulses in CD lasers. This study forms the bulk of chapter 4. Considerable attention was paid to transition between CW emission at very low temperatures to self-pulsation. Below 100 K in the CW regime, peculiar non-linearities in the light-current characteristics appeared. Near field measurements revealed that these were due to instabilities in the waveguide as a result of spatial hole burning of the carrier density. Polarisation resolved near field measurements above 100 K, when the device was in the self-pulsating regime, revealed that there was considerable modification

of the waveguide between pulses. Time resolved near field measurements performed on a streak camera showed that there was indeed considerable modification of the spatial distribution of the optical emission during the evolution of a pulse. By extending the model to include spatial variations, it was possible to show that the origin of the self-pulsation is due to a self focusing effect. The sum total of the lateral refractive index step due to the blocking layers, and the carrier induced modification of the refractive index, leads to a repetitive antiguiding/guiding effect and results in self-sustained pulsation. This has important consequences for the design of self-pulsating lasers in new material systems since the refractive index of the semiconductor varies with the bandgap.

Initial attempts at achieving reliable self-pulsation in wider bandgap materials such as AlGaInP have not been very successful. In particular, it has proved very difficult to manufacture lasers which self-pulsate at elevated temperatures. Most researchers have adopted the approach of adding extra saturable absorbing material near the active region in order to enhance the self-pulsation. Unfortunately, the addition of extra saturable absorbing material has the added disadvantage of driving up the threshold current. A thorough investigation of commercial red self-pulsating lasers is presented in chapter 5. Analysis of the temperature dependence of threshold current reveals that carrier leakage contributes at least 30% of the current at room temperature. Also, the lasers only exhibit self-pulsation in the temperature range 230 K $\leq T \leq$ 330 K. Polarisation resolved near field investigations reveals that these lasers do not exploit self-focusing effects identified in infrared CD lasers. Since low threshold gain guided AlGaInP lasers have been demonstrated in the literature, this suggests that it should be possible to design a red self-pulsating laser which exploits self-focusing and which has a low threshold.

In recent years additional uses other than optical storage have emerged for self-pulsating lasers. One property of self-pulsating lasers which is very

interesting is their ability to synchronise to an external modulation (either electrical or optical). This means that they have potential application in all-optical telecommunications networks, where they could be used in clock extraction and distribution subsystems. In chapter 6 the possibility of using a self-pulsating CD laser in such a clock extraction subsystem was explored. By studying the effect of timing jitter on an electro-optically synchronised self-pulsating CD laser the inherent limitations of using a CD laser in this fashion were assessed. Consequently, constraints on the type of encoding were inferred. The dependence of phase, between an incoming data stream and the synchronised self-pulsating lasers was also explored. It transpires that this phase has a dependence on injected power and detuning from the free-running self-pulsation frequency. This is unfortunate, since optical signals may suffer different levels of attenuation along different paths. However, simulation showed that this effect could be minimised by maximising the power incident on the self-pulsating laser at switching nodes.

7.2 The Future

It is clear from the preceding discussion, that much work in this area remains to be done. Self-focusing has been identified as the cause of self-pulsation in CD lasers. The next step is to design a red self-pulsating laser which exploits this effect. Since the refractive index of the semiconductor material is different, considerable modelling will have to be done to optimise the lateral index profile in the new material. These new structures will then have to be manufactured and tested. Eventually it will become necessary to migrate this technology to even wider bandgap materials such as GaN, and the structures will have to be optimised again.

The instability/nonlinearity which causes self-pulsation in infrared CD lasers bears a striking resemblance to the optical Kerr nonlinearity which is exploited in some solid-state modelocked lasers. It may also be possible to

exploit this nonlinearity in CD type structures to produce very short modelocked pulses. Initial investigations using AR coated CD lasers in external cavities have been promising and some pulse shortening has been observed.

It is uncertain what role the length of the laser chip plays in the self-pulsation. It would be very interesting to investigate how an optical pulse propagates in a long laser chip with similar transverse cross-section. If the device self-pulsated, and the frequency could be controlled, it might even be possible to realise some type of 'self-modelocked' laser diode, where the self-pulsation frequency matched the roundtrip time of the laser cavity. If this were possible, the device would have enormous advantages over conventional modelocked semiconductor lasers, since it would not require an external cavity.

Considerable research has yet be done on optical synchronisation of self-pulsating lasers. The investigations in this thesis have been primarily concerned with synchronised lasers of very similar wavelengths. To the best of my knowledge, no comprehensive study has been done on the inherent limitations of synchronising lasers with substantially different wavelengths. A system using lasers with a large wavelength difference might be advantageous since it is inherently one way (the wider bandgap semiconductor laser would be transparent to light from the narrow bandgap semiconductor laser, but not vice versa). This would remove the requirement for separate optical isolation of the master laser.

Bibliography

[1] Albert Einstein. Zur quantentheorie der strahlung. *Zeitschrift für Physik*, 18:121–128, March 1917.

[2] A. L. Schawlow and C. H. Townes. Infrared and optical masers. *Phys. Rev.*, 112(6):1940–1949, Dec 1958.

[3] T. H. Maiman. Stimulated optical radiation in ruby lasers. *Nature*, 187:493, 1960.

[4] L. A. Coldren and S. W. Corzine. *Diode lasers and photonic integrated circuits.* Microwave and optical engineering. Wiley, 1995.

[5] L. Coldren and T. Koch. Analysis and design of coupled-cavity lasers-part ii: Transient analysis. *IEEE J. Quantum Electron.*, 20:671–682, 1984.

[6] B. Corbett and D. McDonald. Ridge waveguide single longitudinal mode 1.3 μm fabry-perot laser by modal perturbation. *IEEE J. Quantum Electron.*, 31:2181–2182, 1995.

[7] Shun Lein Chuang. *Physics of Optoelectronic Devices.* Wiley Series in Pure and Applied Optics. Wiley, 1995.

[8] G. P. Agrawal and N. K. Dutta. *Long-Wavelength Semiconductor Lasers.* Electrical/Computer Science and Engineering Series. Van Nostrand Reinhold, New York, 1986.

[9] E. S. Yang, P. G. McMullin, A. W. Smith, J. Blum, and Shih. Degradation induced microwave oscillations in double-heterostructure lasers. *Appl. Phys. Lett.*, 2:324–326, 1974.

[10] N. G. Basov. Dynamics of injection lasers. *IEEE J. Quantum Electron.*, QE-4:855–867, 1968.

[11] J. P. van der Zeil, J. L. Merz, and T. L. Paoli. Study of intensity pulsations in proton-bombarded stripe-geometry double-heterostructure AlGaAs lasers. *J. Appl. Phys.*, 50(7):4620–4637, July 1979.

[12] R. W. Dixon and W. B. Joyce. A possible model for sustained pulsation osciallation (pulsations) in AlGaAs double-heterostructure lasers. *IEEE J. Quantum Electron.*, 15:470–474, 1979.

[13] C. Harder, K. Lau, and A. Yariv. Bistability and pulsations in semiconductor lasers with inhomogeous current injection. *IEEE J. Quantum Electron.*, QE-18(9):1351–1360, Sept. 1982.

[14] J. P. van dr Ziel. Self-focusing effects in pulsating AlGaAs double-heterostructure lasers. *IEEE J. Quantum Electron*, QE-17(1):60–68, January 1981.

[15] J. Buus. Models of the static and dynamic behaviour of stripe geometry lasers. *IEEE J. Quantum Electron.*, QE-19:953–960, 1983.

[16] M. Yamada. A theoretical analysis of self-sustained pulsation phenomena in narrow stripe semiconductor lasers. *IEEE J. Quantum. Electron.*, 29:1330–1336, 1993.

[17] P. Barnsley. All-optical clock extraction using two contact devices. *IEE Proc. J*, 140(5):325–336, 1993.

[18] B. Sartorius, M. Mörhle, and U. Feiste. 12-64 GHz continuous frequency tuning in self-pulsating 1.55 μm multiquantum-well dfb lasers. *IEEE Journal of Selected Topics in Quantum Electronics*, 1(2):535–538, 1995.

[19] H. Wenzel, U. Bandelow, H. J. Wunsche, and J. Rehberg. Mechanisms of fast self-pulsations in two-section DFB lasers. *IEEE J. Quantum Electron.*, 32:69–78, 1996.

[20] R. Schatz. Longitudinal spatial instability in symmetric semiconductor lasers due to spatial hole burning. *IEEE J. Quantum Electron.*, 30:1443–1449, 1992.

[21] G. H. Duan and P. Landais. Self-pulsation in multielectrode distributed feedback lasers. *IEEE Photon. Technol. Lett.*, 7:278–280, 1995.

[22] X. Tang, J. P. van der Ziel, B. Chang, R. Johnson, and J. A. Tatum. Observation of bistability in GaAs quantum-well vertical-cavity surface-emitting lasers. *IEEE J. Quantum Electron.*, 33(6):927–932, June 1997.

[23] C. R. Mirasso, G. H. M. van Tartwijk, E. Hernádez-García, D. Lenstra, S. Lynch, P. Landais, P. Phelan, J. O'Gorman, M. San Miguel, and W. Elsäßer. Self-pulsating semiconductor lasers: Theory and experiment. *IEEE J. Quantum Electron.*, 35(5):764–770, May 1999.

[24] J. C. M. Diels, I. C. McMichael J. J. Fontaine, and F. Simoni. Control and measurement of ultrashort pulse shapes (in amplitude and phase) with femtosecond accuracy. *Appl. Opt.*, 24(9):1270–1282, 1985.

[25] M. Osinski and M. J. Adams. Intrinsic manifestation of regular pulsations in time-averaged spectra of semiconductor lasers. *Electronics Letters*, 20(13):525–526, June 1984.

[26] K. Vahala, L. C. Chiu, S. Margalit, and A. Yariv. On the linewidth enhancement factor α in semiconductor injection lasers. *Appl. Phys. Lett.*, 42(8):631–633, April 1983.

[27] M. Osinski and J. Buus. Linewidth broadening factor in semiconductor lasers - an overview. *IEEE J. Quantum Electron.*, QE-23(1):9–29, Jan 1987. (Invited Paper).

[28] P. Lazaridis, G. Debarge, and P. Gallion. Time-bandwidth product of chirped $sech^2$ pulses: Application to phase-amplitude-coupling factor measurement. *Optics Letters*, 20(10):1160–1162, May 1995.

[29] Peter T. Landsberg. *Recombination in Semiconductors.* Cambridge University Press, 1991.

[30] Y Arakawa and H. Sakaki. Multidimensional quantum well laser and temperature dependence of its threshold current. *Appl. Phys. Lett.*, 40(11):939–941, June 1982.

[31] P. Blood, E. D. Fletcher, K Woodbridge, K. Heasman, and A. Adams. Influence of the barriers on the temperature dependence of threshold current in GaAs/AlGaAs quantum well lasers. *IEEE J. Quantum Electron.*, 25(6):1459–1468, June 1989.

[32] P. McEvoy, P. Landais, S. A. Lynch, J. O'Gorman, and J. Hegarty. Relaxation oscillations and self-pulsations in compact disc laser diodes. Submitted for publication.

[33] E. A. Avrutin. Analysis of spontaneous emmision and noise in self-pulsing laser diodes. *IEE Proc. J. Optoelectron.*, 140:16–20, 1993.

[34] P. Blood, S. Colak, and A. I. Kucharska. Influence of broadening and high injection effects on GaAs-AlGaAs quantum well lasers. *IEEE J. Quantum Electron.*, 24:1593, 1988.

[35] H. Hirakawa and H. Sakaki. Mobility of the two-dimensional electron gas at selectively doped n-type AlGaAs/GaAs heterojunctions with controlled electron concentrations. *Phys. Rev. B.*, 33(12):8291–8303, June 1986.

[36] T. L. Paoli. Nonlinearities in the emission characteristics of stripe geometry (AlGa)As double-heterostructure junction lasers. *IEEE J. Quantum Electron.*, QE-12:770–776, 1976.

[37] J. L. Synge and B. A. Griffith. *Principles of Mechanics.* Physics Series. McGraw-Hill, 3rd edition, 1987.

[38] Paul McEvoy. *Numerical Invesitgations of Waveguiding Properties in Semiconductor Lasers.* PhD thesis, University of Dublin, October 1998.

[39] T. Takayama, O. Imafuji, H. Suguira, M. Yuri, H. Naito, M. Kume, and K. Itoh. Low noise and high power GaAlAs lasers diodes with a new real refractive index guided structure. *Jpn. J. Appl. Phys.*, 34:3533–3542, 1995.

[40] T. Takayama, O. Imafuji, M. Yuri, H. Naito, M. Kume, A Yoshikawa, and K. Itoh. 800 mW peak-power self-sustained pulsation GaAlAs laser diodes. *IEEE Jounal of Selected Topics in Quantum Electron.*, 1(2):562–568, June 1995.

[41] H. van Houten and J. Schleipen. Optical data storage. *Physics World, IOP publishing*, 11(10), October 1998.

[42] Eugene Hecht. *Optics.* Addison Wesley, 2 edition, 1987.

[43] M. Ikeda, Y. Mori, H. Sato, K. Kaneko, and N. Watanabe. Room tepmerature continous wave operation of an AlGaInP double heterostructure laser grown by athmospheric pressure metalorganic chemical vapor deposition. *Appl. Phys. Lett.*, 47(10):1027–1028, 1985.

[44] K. Kobayashi, S. Kawata, A. Gomyo, I. Hino, and T. Suzuki. Room temperature CW operation of AlGaInP double heterostructure visible lasers. *Electron. Lett.*, 21(20):931–932, 1985.

[45] M. Ishikawa, Y. Ohba, H. Sugawara, M. Yamamoto, and T. Nakanishi. Room temperature CW operation of InGAP/InGaAlP visible light laser diodes on GaAs substrates grown by metalorganic chemical vapor deposition. *Appl. Phys. Lett.*, 48(3):207–208, 1986.

[46] T. Tanaka, T. Kawano, and T. Kajimura. InGaP/InGaAIP double-heterostructure and multiquantum-well laser diodes grown by molecular-beam epitaxy. *J. Appl. Phys.*, 61(5):1713–1719, 1987.

[47] M Ikeda, A. Toda, K. Nakano, Y. Mori, and N. Watanabe. Room-temperature continous-wave opeation of GaInP/AlGaInP multiquantum well laser grown by metalorganic chemical vapor deposition. *Appl. Phys. Lett.*, 50(16):1033–1034, April 1987.

[48] D. P. Bour and J. R. Shealy. High power (1.4 W) AlGaInP graded-index seperate confinement heterostructure visible ($\lambda \sim 658nm$) laser. *Appl. Phys. Lett.*, 51(21):1658–1660, November 1987.

[49] J. Hashimoto, T. Katsuyama J. Shinkai, I. Yoshida, and H. Hayashi. Effects of strined structure on the threshold current density of AlGaInP/GaInP lasers. *Appl. Phys. Lett.*, 58(9):879–880, March 1991.

[50] C. P. Kuo, S. K. Vong, R. M. Cohen, and G. B. Stringfellow. Effect of mismatch strain on band gap in III-V semiconductors. *J. Appl. Phys.*, 57(12):5428–5432, June 1985.

[51] H. B. Serreze, Y. C. Chen, and R. G. Waters. High-power, very low threshold, GaInP/AlGaInP visible diode lasers. *Appl. Phys. Lett.*, 58(22):2464–2466, June 1991.

[52] T. Katsyama, I. Yoshida, J. Shinkai, and J. Hasimoto. High temperature ($> 150^0$C) and low threshold current operation of AlGaInP/GaInP strained multiple quantum well visible laser diodes. *Appl. Phys. Lett.*, 59(26):December, 1991.

[53] S. J. Chang and C. S. Chang. 642-nm AlGaInP laser diodes with triple tensile strain barrier cladding layer. *IEEE Photon. Technol. Lett.*, 10(5):651–653, May 1998.

[54] H. Adachi, S. Kamiyama, I. Kidoguchi, and T. Uenoyama. Self-sustained pulsation in 650-nm-band AlGaInP visible-laser diodes with highly doped saturable absorbing layer. *IEEE Photon. Technol. Lett.*, 7(12):1406–1408, December 1995.

[55] R. C. P. Hoskens and T. G. van de Roer. Self-pulsating laser with quantum well saturable absorber. *Appl. Phys. Lett.*, 65(10):1343–1345, September 1995.

[56] I. Kidoguchi, H. Adachi, T. Fukuhisa, and M. Mannoh. Stable operation of self-sustained pulsation in 650-nm-band AlGaInP visible lasers with highly doped saturable absorbing layer. *Appl. Phys. Lett.*, 68(25):3543–3545, June 1996.

[57] I. Kidoguchi, H. Adachi, S. Kamiyama, T Fukuhisa, M. Mannoh, and Akira Takamori. Low-noise 650-nm-band AlGaInP visible laser diodes with a highly doped saturable absorbing layer. *IEEE J. Quantum Electron.*, 33(5):831–837, May 1997.

[58] H. Summers and P. Rees. Thermal limitation of self-pulsation in 650 nm AlGaInP laser diodes with an epitaxially integrated absorber. *Appl. Phys. Lett.*, 71(18):2665–2667, November 1997.

[59] H. D. Summers and P. Rees. High-temperature opeation of 650-nm wavelength AlGaInP self-pulsating laser diodes. *IEEE Photon. Technol. Lett.*, 10(9):1217–1219, September 1998.

[60] P. Blood, S. Colak, and A. I. Kucharska. Temperature dependednce of threshold current in GaAs/AlGaAs quantum well lasers. *Appl. Phys. Lett.*, 52(8):599–601, February 1988.

[61] M. Ishikawa, H. Shiozawa, K. Itaya, G. Hatakoshi, and Y Uematsu. Temperature dependednce of the threshold current for InGaAlP visible laser diodes. *IEEE J. Quantum Electron.*, 27(1):23–29, January 1991.

[62] Peter S. Zory, editor. *Quantum Well Lasers.* Quantum Electronics - Principles and Applications. Academic Press, 1993.

[63] S. J. Chang, C. S. Chang, Y. K. Su, P. T. Chang, Y. R. Wu, K. H. Huang, and T. P. Chen. AlGaInP yellow-green light-emitting diodes with a tensile strain barrier cladding layer. *IEEE Photon. Technol. Lett.*, 9(9):1199–1201, September 1997.

[64] M. Jinno and T. Matsumoto. All-optical timing extraction using a 1.5 μm self-pulsating multielectrode DFB LD. *Electron. Lett.*, 24(23):1426, 1427 1988.

[65] M. Jinno and T. Matsumoto. Optical retiming regenerator using 1.5 μm multi-electrode DFB LDs. *Electron. Lett.*, 25(20):1332–1333, 1989.

[66] G. Farrell, P. Phelan, J. Hegarty, and J. Shields. All-optical timing extraction with frequency division using a twin section laser diode. *IEEE Photon. Tech. Lett.*, 5(6):718–721, 1993.

[67] U. Feiste, D. J. As, and A. Ehrhardt. 18 GHz all-optical frequency locking and clock recovery using a self-pulsating two-section DFB laser. *IEEE Photon. Tech. Lett.*, 6(8):930–932, 1994.

[68] A. Egan, P. Rees, J. O'Gorman, M. Harley-Stead, G. Farrell, J. Hegarty, and P. Phelan. Theoretical investigations of electro-optical synchronisation of self-pulsating laser diodes. *IEE Proc. Optoelectron.*, 143(1):31–36, February 1996.

[69] A. Egan, M. Harley-Stead, P. Rees, S. Lynch, P. McEvoy, J. O'Gorman, and J. Hegarty. All-optical synchronisation od self-pulsating laser diodes. *Appl. Phys. Lett.*, 68(25):3534–3536, June 1996.

[70] A. Egan, M. Harley-Stead, P. Rees, S. Lynch, J. O'Gorman, and J. Hegarty. An experimental and theoretical analysis of jitter in self-pulsating lasers synchronised to periodic electrical signals. *IEEE Photon. Technol. Lett.*, 8(6):758–760, June 1996.

[71] A. Egan, M. Harley-Stead, P. Rees, S. Lynch, P. McEvoy, J. O'Gorman, and J. Hegarty. All-optical synchronisation of self-pulsating laser diodes with frequency multiplication and division. *Journal of Modern Optics*, 45(6):1239–1248, 1998.

[72] U. Bandelow, H. J. Wunsche, and H. Wenzel. Theory of self-pulsations in two-section DFB lasers. *IEEE Photon. Technol. Lett*, 5:1176–1179, 1993.

[73] A. J. Lowery. Dynamics of SHB-induced mode instabilities in uniform DFB semi-conductor lasers. *Electron. Lett.*, 29:1852–1854, 1993.

[74] D. D. Marcenac and J. E. Carroll. Distinction between multimoded and single-moded self-pulsations in DFB lasers. *Electron. Lett.*, 30:1137–1138, 1994.

[75] J. B. Georges and K. Y. Lau. Broadband microwave fiber-optic links with rf phased-array antennas. *IEEE Photon. Technol. Lett.*, 5(11):1344–1346, 1993.

[76] A. Egan, J. O'Gorman ann P. Rees, G. Farrell, J. Hegarty, and P. Phelan. Frequency dependence of phase between synchronised self-pulsating laser emission and injected periodic electrical signals. *Electron. Lett.*, 31(10):802–803, 1995.

[77] P. Phelan, G. Farrell, and J. Hegarty. All-optical clock synchronisation with frequency division of mode-locked pulses. *IEEE Photon. Technol. Lett.*, 4(8):930–932, 1992.

[78] P. Phelan, G. Farrell, and J. Hegarty. All-optical synchronisation and multiplication of the frequency of mode-locked pulses. *IEEE Photon. Technol. Lett.*, 4(12):1332–1335, 1992.

[79] Aidan Egan. *Synchronised Self-Pulsating Laser Diode Dynamics.* PhD thesis, University of Dublin, October 1995.

[80] P. Rees, P. McEvoy, A. Valle, J. O'Gorman, S. Lynch, P. Landais, L. Pesquera, and J. Hegarty. A theoretical analysis of optical clock extraction using a self-pulsating laser diode. *IEEE J. Quantum Electron.*, 35(2):221–227, February 1999.